NASA Contractor Report 3973

Helicopter Rotor Noise Due to Ingestion of Atmospheric Turbulence

John C. Simonich, Roy K. Amiet,
Robert H. Schlinker, and Edward M. Greitzer

CONTRACT NAS1-17096
MAY 1986

NASA

NASA Contractor Report 3973

Helicopter Rotor Noise Due to Ingestion of Atmospheric Turbulence

John C. Simonich, Roy K. Amiet,
and Robert H. Schlinker
United Technologies Research Center
East Hartford, Connecticut

Edward M. Greitzer
Massachusetts Institute of Technology
Cambridge, Massachusetts

Prepared for
Langley Research Center
under Contract NAS1-17096

NASA
National Aeronautics
and Space Administration

**Scientific and Technical
Information Branch**

1986

TABLE OF CONTENTS

TABLE OF CONTENTS (Cont'd)

SUMMARY

A theoretical study was conducted to develop an analytical prediction method for helicopter main rotor noise due to the ingestion of atmospheric turbulence. The study extends an existing UTRC model based on an isotropic turbulence assumption at the rotor plane by incorporating an atmospheric turbulence model and a rapid distortion turbulence contraction model which together determine the statistics of the anisotropic turbulence at the rotor plane. Critical to turbulence contraction model is the inclusion of a rotor mean flow model which predicts the turbulence vorticity distortion during the rotor in-flow process.

Inputs to the combined mean inflow and turbulence models are controlled by atmospheric wind characteristics and helicopter operating conditions. The generalized acoustic source model was employed to calculate absolute noise levels for full scale helicopters without the use of empirical or adjustable constants. Calculated turbulence ingestion noise levels were compared with existing trailing edge noise predictions for full scale aircraft to assess the relative importance of the two mechanisms.

Conclusions from the study can be grouped into two categories. In the case of fluid dynamic results, obtained from the various turbulence and rotor mean inflow calculations, the following observations are available. For the atmospheric conditions encountered by a rotor, statistical properties of the upstream turbulence can be modeled as locally stationary and homogeneous. In addition, for wavenumbers controlling the generation of atmospheric turbulence ingestion noise, the turbulence field is locally isotropic upstream of the rotor. Contraction and turning of this isotropic turbulence field by the rotor mean-inflow distorts the turbulence vorticity field creating a nonisotropic turbulence field at the rotor disk. Deformation of the vorticity filaments can be computed using an existing rapid distortion theory. For large mean flow contraction ratios accurate prediction of vorticity components at the rotor face requires incorporating the differential drift of fluid particles on adjacent streamlines. Significant contraction ratios and turning of vortex filaments occur for hover, low speed vertical ascent and low speed forward flight. The strength of the resulting nonisotropic and nonhomogeneous vorticity field at the rotor differs from the upstream isotropic turbulence conditions by factors of 0.5 to 20 over the rotor disk. In contrast, for high speed vertical ascent and high speed forward flight, turbulence distortion is non-existent and turbulence spectra at the rotor face are isotropic.

Relative to the aeroacoustic conclusions, the present first principles theory for rotor turbulence ingestion noise predicts large differences between quasi-tonal peak amplitudes for isotropic atmospheric turbulence and nonisotropic turbulence incident on the rotor disk but less significant differences for the acoustic energy produced. The largest difference occurs for hover and low speed vertical ascent with approximately a 10 dB difference in quasi-tonal peak amplitudes, a 5 dB difference in high frequency broadband noise, and a 3 dB difference in acoustic spectrum energy. Predicted acoustic spectra are sensitive to the non-homogeneous turbulence vorticity distributions at the rotor. Accurate prediction of these features requires modeling the differential drift of fluid particles on adjacent streamlines. Failure to account for this effect results in significant differences in the quasi-tonal peak amplitudes.

The most intense turbulence ingestion noise corresponds to the low speed vertical ascent case and the quietest is the forward flight case. Increasing forward flight speed minimizes the turbulent eddy distortion which decreases quasi-tonal peak amplitudes and broadens the peaks. Polar directivity patterns associated with these operating conditions exhibit a dipole character for hover and vertical ascent irrespective of the incident turbulence features. Azimuthal directivity patterns are uniform for hover and vertical ascent but vary strongly with forward flight. Accurate predictions of these trends requires detailed statistics of the atmospheric turbulence. Stability length is the most sensitive parameter as indicated by a 20 dB increase in acoustic energy between stable and unstable atmospheric conditions. Decreases in altitude and increases in wind speed enhance turbulence ingestion noise. When compared to trailing edge noise, turbulence ingestion noise is the dominant acoustic source mechanism below 30 rotor harmonics while trailing edge noise dominates above 100 harmonics.

INTRODUCTION

The noise level at a given angle relative to a helicopter and within a specified frequency band represents the sum of contributions of a number of separate noise sources. Some mechanisms apply primarily to the main rotor, some apply to both rotors, and in more complex situations, interactions occur between rotors. The list of possible rotor noise mechanisms is lengthy and is often debated among specialists in helicopter noise research. It is generally agreed that, in the absence of impulsive noise, random or broadband noise can be a strong source.

Design of helicopters with reduced broadband noise level requires the ability to predict the contribution from each source mechanism. Due to the limitations of empirically based helicopter noise prediction methods an increasingly important objective of helicopter noise research has been the development of procedures based on first principle approaches. One specific broadband noise source for which such analytical prediction methods have been developed is the ingestion of atmospheric turbulence by the main rotor blades. This sound generation mechanism involves the interaction of the rotating blades and the unsteady upwash velocity vectors associated with the atmospheric turbulent eddies ingested by the rotor. The resulting noise exists in the presence of loading noise and thickness noise mechanisms. It is also additive to the rotor trailing edge noise and vortex interactions noise generation mechanisms which represent additional broadband acoustic sources.

Previous analytical methods treating this noise mechanism were developed to predict far field noise for isotropic turbulence rotor inflows. However, the analytical methods were limited in their ability to predict absolute sound pressure levels and acoustic spectra for a rotor operating in a realistic atmospheric turbulence field with a non-isotropic spectrum. Although a generalized acoustic analysis existed, realistic turbulence conditions, needed as inputs to the analysis at the rotor face, were unknown. The primary limitation was the lack of a rigorous turbulence contraction model to account for the distortion of the upstream atmospheric turbulence as it is entrained by the rotor mean inflow. This distortion process can be regarded as due to the deformation of the vortex filaments that represent the turbulence. Both contraction and turning of the vortex filaments by the rotor mean inflow serves to alter the initial atmospheric turbulence spectrum as it convects into the rotor.

In the absence of a realistic atmospheric turbulence model and a turbulence contraction model, it is difficult to rank turbulence ingestion noise relative to other noise mechanisms. Furthermore, since full scale outdoor rotor tests contain other operative noise mechanisms, direct experimental assessment of this noise source is not possible. The lack of a firm understanding of this noise mechanism for realistic rotor operating

conditions created a clear need for a fundamental study to advance the existing analytical methods. The objective of the present study was to define the atmospheric turbulence field and the effect of streamline contraction and turning on the turbulence characteristics incident on the rotor disk. Application of the turbulence contraction model provided a realistic input to a previously developed first principles turbulence ingestion noise theory. The combined turbulence and acoustic source models were then employed to predict full scale helicopter rotor noise without the use of empirical constants. Calculated sound pressure levels were then compared with other noise mechanisms to assess the relative importance of rotor turbulence ingestion noise.

LIST OF SYMBOLS AND NOMENCLATURE

A	Constant in geostrophic drag law
B	Constant in geostrophic drag law
C_o	speed of sound
C_T	Rotor Thrust Coefficient = $T / \rho\pi R^2 (\Omega R)^2$
d	Zero plane displacement height
$\underline{e}$	Unit vector along one of the three upstream or downstream axes
E(k)	Wavenumber energy spectrum
$\underline{f}^D$	vector defined by Equation A.17 or A.18
f_c	Coriolis parameter, $2\omega \sin \theta$
$\underline{F}$	force vector
g	Gravitational acceleration
G	Geostrophic wind speed
H	Average rooftop height
k	Wave number
$\underline{k}$	Wavevector of turbulence
k_E	wave number defined by Equation 27
ℓ	spatial integral scale of the streamwise component of turbulence
l	Length scale used in Reference 1
L	Monin - Obukhov length
L_c	characteristic length scale for Rapid Distortion Theory
L_∞	Spatial integral scale
L_w^*	Integral length scale
M_n	Mach number in direction of observer

n	Direction of the principle normal to the streamline
$\underline{n}$	Unit vector normal to airfoil
p	exponent in mean velocity power law
P_s	sound pressure
$\underline{q}$, $\underline{Q}$	Velocity field and magnitude of a Fourier component of turbulence. See Equation 51
r_x	Displacement in x direction
r	Local radius of curvature
r_s	source to observer distance
R	Rotor radius
R_i	Richardson number
$\tilde{R}_{ww}$	Cross correlation coefficient
T	Thrust
u	Turbulence fluctuation
U	Local time mean velocity
U_∞	Mean horizontal freestream velocity
U_*	Friction velocity = $\sqrt{\tau_w/\rho}$
V_∞	Mean vertical freestream velocity
V_o	Rotor induced velocity = $\frac{C_T \Omega R}{2\sqrt{\lambda^2 + \mu^2}}$
w	Vertical turbulence fluctuations
$\sqrt{w^2}/U_\infty$	rms turbulence intensity
x_i	Upstream Cartesian coordinate system, i = 1, 2, 3

$\underline{X}$	vector location
Z	Height above ground
Z_o	Roughness length
Z_T	Tropopause height
α	Rotor tip path plane angle of attack
$\Gamma(\ )$	Gamma function
δ	Boundary layer thickness
ϵ_{ijk}	Alternating tensor
θ	Polar angle
θ	Geographic latitude
κ	von Karman constant
λ	Wavelength of Fourier component of turbulence, or rotor inflow ratio = $(U_\infty \sin \alpha - V_o)/\Omega R$
μ	Rotor advance ratio = $U_\infty \cos \alpha/(\Omega R)$
ζ_i	Downstream Cartesian coordinate system
T	Temperature
τ	Temperature fluctuations
τ_w	Wall shear stress
ϕ	Azimuthal angle
Φ_m	Nondimensional wind speed gradient
χ	Wake skew angle = $\tan^{-1}\left[-U_\infty \cos \alpha/(U_\infty \sin \alpha - V_o)\right]$
ω, Ω	Rotation rate
$\underline{\omega}$, $\underline{\Omega}$	Vorticity field and magnitude of a Fourier component of turbulence. See Equation 52.

Superscripts

U and D Specify the upstream or downstream location

Subscripts

i,j,k
1,2,3 Specify either a vector (such as one of the vectors $\underline{e}_1$, $\underline{e}_2$, $\underline{e}_3$) or a component of a vector (such as the first Cartesian component of the vector $\underline{e}_2$)

PREVIOUS INVESTIGATIONS

Relevant Analytical and Experimental Studies

The study of the noise produced by interaction of turbulence with an airfoil has been an ongoing research area for many years. The following summary is not intended to be a comprehensive review, but only to touch on the primary developments as they relate to the objectives of the present program. For an extensive historical development in this topic area the reader is referred to the review papers by George (ref. 1) or Brooks and Schlinker (ref. 2). In addition, there have been numerous studies of the unsteady loading on an airfoil in a turbulent flow, but the following discussion concentrates on studies pertaining to noise prediction.

Sharland (ref. 3) was one of the first to demonstrate the noise generated by the interaction of an airfoil with a turbulent flow. He placed a small isolated flat plate in a nozzle exhaust and obtained good agreement between the experimental results and a simple theory based on the concept of unsteady surface pressure correlation area. Dean (ref. 4) improved on these experiments by measuring the airfoil surface pressure at a point and the spectrum of the vertical component of the incident turbulence, in addition to the far-field noise. Approximate calculations were made of the airfoil surface pressure correlation lengths.

Approaches such as these, based on a surface pressure correlation area, present the difficult task of determining the correlation as a prerequisite to the noise prediction. An alternative approach is to formulate the prediction method in terms of the inflow turbulence spectrum together with a general solution for the airfoil response functions for skewed gusts and nonzero Mach number. To be complete, such a prediction must include noncompactness effects of the airfoil surface pressure.

Obtaining a prediction method through the use of airfoil response functions has been accomplished by several authors (refs. 5 through 7). However, many of these are limited in some respect. For example, references 5 and 6 use low frequency airfoil response functions, appropriate to incompressible flow. This leads to incorrect high frequency behavior since the Sears function (incompressible flow) decays as $k^{-1/2}$ (k = reduced frequency) whereas the correct behavior for compressible flow is k^{-1}. Thus, these prediction methods significantly overpredict the high frequency spectrum where the acoustic wavelength is comparable to or smaller than the chord. Also, both predictions in references 5 and 6 assume chordwise compactness of the surface pressure which is significantly in error at the higher frequencies.

The prediction method of Amiet (ref. 7) was one of the first analyses to incorporate all the above factors into a consistent acoustic model. The procedure was based on accurate flat plate airfoil response functions for nonzero Mach number. Noncompactness effects of the airfoil surface pressure source term in both the chordwise and spanwise directions were included. Comparison with the experiment by Paterson and Amiet (ref. 8) showed good agreement.

The above described noise prediction methods are limited to the case of rectilinear airfoil motion through turbulence. The case of a rotating airfoil interacting with turbulence, such as a propeller or helicopter rotor in hover, was first treated rigorously by Homicz and George (ref. 9). This analysis made use of the exact expression for the pressure field of a rotating dipole. However, approximations were needed to include the effects of the spanwise turbulence correlation length and the assumption of chordwise compactness of the surface pressure was used. Also, the airfoil response function was a low frequency approximation which has inaccuracies at high frequency.

Amiet (ref. 10) formulated a different approach to modeling the rotating blade case. Rather than use the expression for a rotating dipole, the rectilinear motion analysis (ref. 7) was used to calculate the instantaneous spectrum of the rotor as a function of azimuthal position. Whereas this appears to be an approximation, it becomes an exact analysis for high frequency and gives good results for frequencies approaching the rotor frequency. The flat plate airfoil response functions used are accurate over the entire frequency range and the effects of both chordwise and spanwise noncompactness are included. A major advantage of this approach is that it can be readily generalized to the case of helicopter forward flight.

The report of George and Chow (ref. 11) compared the method of Amiet with that of George and Kim (ref. 12). The method of George and Kim was indicated to be similar to that of Homicz and George although it requires a high frequency assumption to obtain a simplified result. The authors compared the methods of Amiet and George and Kim with available data and found comparable results for the two methods.

Comparisons between theory and experiment were also made by Paterson and Amiet (ref. 13). One extension made to the theory for these comparisons was to simulate the effect of eddy elongation by varying the drift velocity of the eddy through the rotor disk during forward flight. For low drift velocities (low forward flight speed) a given eddy would be cut by the rotor more often than for high drift velocities. Assuming the rotor tip velocity is significantly greater than the drift velocity, lowering the drift velocity will not change the overall acoustic energy but it does concentrate more acoustic energy around the harmonics of blade passage frequency.

The present study extends this analysis by performing a more rigorous calculation of the sound produced by a stretched eddy, as well as modeling the details of the stretching process. By combining a mean flow contraction calculation with a rapid distortion calculation for the turbulence, the spectrum of the contracted turbulence is determined. In addition, because the present treatment allows for distortion of the turbulence spectrum, it predicts different acoustic energy level when compared to the non-distorted turbulence inflow condition.

Constraints of Previous Analytical Formulations

The previous subsection outlined the general features of the various analytical approaches. From a noise prediction standpoint the theory of Amiet (ref. 13) represents the most rigorous treatment of rotor turbulence ingestion noise since it models the eddy drift velocity through the rotor under forward flight conditions. Since the present study represents an extension of the previous turbulence ingestion noise analyses of Amiet, it is necessary to review the capabilities of this method.

The rotating blade analysis of Amiet modeled blade-to-blade correlations and, hence, was capable of predicting narrowband random tones at harmonics of blade passage frequency. Input parameters to the generalized theory required only turbulence intensity, length scale, and rotor operating conditions such as tip speed and orientation of the rotor with respect to the flow.

The experimental assessment of the analysis employed isotropic turbulence flows in open jet acoustic wind tunnel tests using a model rotor in vertical ascent and forward flight operating conditions. It was recognized that the use of isotropic turbulence did not simulate realistic applications. However, from a theoretical standpoint, analytical expressions for the turbulence characteristics needed as an input to the theory were documented. Fundamental shortcomings of the acoustic source model could, therefore, be assessed without questions arising about the turbulence field. In particular, for the forward flight case, the theoretical model describing the variation of the radial and azimuthal position of successive blade/eddy intersections could be tested.

The experimental assessment of the analysis for non-isotropic in-flows was, conducted in outdoor hover tests using a model rotor (ref. 13). Similar to the controlled turbulent inflow tests carried out in the open jet acoustic wind tunnel, the outdoor tests confirmed that atmospheric turbulence is a source of broadband and quasi-tonal noise. Except for the first few harmonics of blade passage frequency, the turbulence ingestion noise mechanism dominated, causing narrowband random noise extending to approximately 25 harmonics of BPF. This was due to the interaction of axially elongated eddies with the rotor.

An anisotropic flow model was found to be necessary to predict the measured noise levels for the outdoor hover test. Otherwise, errors of as much as 25 dB occurred. At the time of the study, only a semi-empirical flow model was available to describe the complicated anisotropic turbulent inflow. This was achieved by decreasing the convection speed through the rotor in the isotropic analysis to give an axially elongated length scale corresponding to the value determined from hot-wire measurements during the experiment. The isotropic turbulence spectrum definition was, however, retained since transverse and axial turbulence intensity measurements indicated that the inflow velocity field was relatively isotropic. The resulting noise prediction showed favorable agreement with the measured values.

The major constraint of this previous study was the lack of a rigorous inflow turbulence model. This observation represents one of the primary motivations of the present investigation. For high speed vertical ascent or forward flight rotor tests conducted in an acoustic wind tunnel with an upstream turbulence generating grid, an isotropic turbulence model is satisfactory since there is little contraction of the flow as it passes through the rotor. However for outdoor hover or slow vertical ascent operating conditions, only a small freestream flow is imposed so that significant contraction of the inflow streamlines occurs. Even an initially isotropic ambient atmospheric turbulence field would be significantly distorted and stretched in the axial direction in the process of convecting through the rotor.

While the above described distortion was recognized in the studies of Paterson and Amiet (ref. 13), an analytical representation of the non-isotropic turbulence spectrum at the rotor face was not available. Consequently there existed a need to develop the atmospheric turbulence model and turbulence contraction model reported in the present study. Conceptually, this effort would provide the turbulence energy spectrum tensor at a station immediately upstream of the rotor disk. Turbulent inflow characteristics could then be defined as a function of the rotor altitude and the statistical details of the ambient atmospheric turbulence field. In essence, the turbulence field at the rotor plane would be linked with the atmospheric turbulence field existing at "infinity" prior to contraction.

PRESENT INVESTIGATION

Objectives

The primary objective of the present study was to develop a generalized atmospheric turbulence ingestion noise prediction theory for helicopter rotors. Although previous investigations treated this noise mechanism the present effort advances existing prediction methods by incorporating a realistic atmospheric turbulence model and modeling the effect of streamline contraction and turning on the turbulence characteristics incident at the rotor disk. Critical to calculating the effects of streamline changes is the development of a rotor mean inflow model for the hover, vertical ascent, and forward flight operating conditions addressed by the prediction method. The resulting turbulence contraction model provides a realistic anisotropic input to the existing turbulence ingestion noise theory of Amiet. The combined turbulence and acoustic source models provide absolute level, full scale helicopter rotor noise predictions without the use of adjustable constants.

A secondary objective was to document the turbulence ingestion noise sensitivity to atmospheric conditions, rotor operating conditions, and observer location. As part of the sensitivity evaluation, the prediction method was used to compare broadband noise due to rotor turbulence ingestion and blade trailing edge noise. The objective of this effort was to determine the relative importance of these mechanisms for the same rotor operating conditions. This provides a capability not available experimentally since the coexistence of multiple sources in rotor noise test data precludes ranking the separate noise mechanisms.

Problem Formulation and Approach

Development of a calculation procedure for rotor noise due to atmospheric turbulence ingestion requires modeling several different phenomena. Specifically, all of the following processes were modeled:

1) Atmospheric turbulence, i.e., the spectral distribution (length scale, amplitude and frequency) of the "ambient" turbulence.

2) The background (or mean) flow into the rotor, i.e., the flow into the rotor not considering the turbulence.

3) The change, or distortion, of the turbulence as it is ingested into the rotor. This distortion is due to the influence of the rotor on the vortex filaments that comprise the turbulence.

4) The unsteady surface pressures generated on the rotor blades when interacting with the spatially nonuniform and unsteady flow that exists at the rotor disk.

5) The acoustic radiation resulting from the fluctuating surface pressures.

The overall calculation process is diagrammed in the "flow chart" shown in figure 1. Here, the ambient turbulence is the input to a dynamic system calculation. As shown, the calculations of parts 2) and 3) can be regarded as a "transfer matrix" which converts the ambient turbulence field into a modified turbulence field at the rotor inlet. The calculations in 4) and 5) then represent operations performed on this input quantity that result in the predicted system noise output.

The report is organized as follows. First, the fluid dynamic and acoustic models associated with the different physical processes will be described. Computational results will then be presented for several cases of practical interest, first for the fluid dynamic parts of the calculation and then for the acoustic part.

ATMOSPHERIC TURBULENCE MODEL

Review of Past Work

Several review articles on the structure of the atmospheric boundary layer have been written in recent years. There appears to be a large range of differences in the data reported and in proposed prediction methods between authors. Teunissen (ref. 14) presented a review of the planetary boundary layer in 1970. Snyder (ref. 15) reviews the state of the art of atmospheric boundary layer modeling in a paper describing procedures for establishing modeling similarity for wind tunnel experiments. A review and evaluation of atmospheric boundary layer models applicable for maritime applications was presented by Fairall et al. (ref. 16) in 1981. More recently, researchers have applied computational fluid dynamics to the atmospheric boundary layer (for example, Campbell (ref. 17)). Treatments of this type, however, are still in the research phase and are not really applicable to engineering calculations.

The model presented below was chosen after a review of the current literature on the topic and is considered to be representative of the present state of the art in atmospheric turbulence prediction. Most of the correlations are from Snyder (ref. 15). These were chosen since they were the only ones found which included non-adiabatic effects (i.e., a non-neutral atmosphere where heat transfer is important).

Model Assumptions and Limitations

To render the problem tractable, a number of simplifying assumptions are employed in the predictions method selected here:

1) The flow is stationary.

This condition assumes that the statistical properties of the flow field do not vary with time. In particular, the mean flow as well as turbulence properties such as the integral length scale, the velocity correlations, etc. are time invariant. This assumption has been shown to be valid (from aircraft measurements (ref. 14)) for periods on the order of 10 to 20 minutes. The fluid particle transit time from a "far upstream station" (ten rotor radii, say) through the rotor is on the order of tens of seconds, i.e., considerably smaller. Hence for the present problem, which deals with events that occur over the time of a particle passage, the approximation that the ambient flow conditions are stationary should be quite a good one.

2) The flow is homogeneous in any horizontal plane.

This implies that the ambient flow is two dimensional. This is strictly valid only for a homogeneous terrain, i.e. one in which the surface does not vary in height or roughness length as a function of horizontal distance. However, for terrain in which the horizontal length scale of the variation in height or roughness length is large compared to the boundary layer thickness, this is not likely to be a serious drawback.

3) The flow is isotropic.

While the real atmospheric boundary layer is a shear flow and not truly isotropic, available data on nonisotropy in the atmosphere is very limited. In general, this assumption is valid for large wavenumbers, i.e. those in the inertial subrange and above. In this "local" region of the energy spectrum, there is little production of turbulence and energy is passed from larger, anisotropic, energy containing eddies to smaller, more nearly isotropic eddies. As the eddies become smaller, they approach the isotropic condition. The real question therefore is what the pertinent wavenumbers for the phenomena of interest are.

The wavenumbers of interest in the current study are limited by the rotor diameter and thickness. Eddies larger than the rotor diameter will affect the rotor only as a slowly varying mean velocity while eddies smaller than the airfoil thickness are not addressed by the thin airfoil theory used in the acoustic source model.

The wavenumber range corresponding to these limits for a typical helicopter under neutrally stable atmospheric conditions is shown in Figure 2. For this case, the wavenumbers of interest are close to the inertial subrange. For atmospheric turbulence, a commonly accepted upper wavelength for isotropy is one third the boundary layer height (although buoyancy effects can decrease this upper limit). The concept of a region of "local" isotropy in the atmosphere is supported by measurements in the atmosphere obtained from hundreds of hours of aircraft data (ref. 18).

For the wavenumbers of concern for noise generation by the ingestion of atmospheric turbulence therefore, the flow will be largely isotropic, and the assumption of local isotropy is valid.

Analytical Expressions

A model is presented below to describe the structure of the atmospheric boundary layer.

The following parameters are predicted:

δ Boundary layer thickness

U_* Friction velocity, $\sqrt{\tau_w/\rho}$

U(z) Mean velocity profiles as a function of height, z, in both the surface layer and the overall boundary layer

L_w* Integral length scale

$\sqrt{w^2}/U_\infty$ rms turbulence intensity

E(k) Wavenumber energy spectrum

The following parameters must be input for neutral conditions (without heat transfer):

G Geostrophic wind speed

Z_o Roughness length

θ Geographic latitude

H General rooftop level

For non-neutral conditions, additional input parameters are:

L Monin-Obukhov length

Z_T Tropopause height

The following section will describe the different parts of the atmospheric model. The procedure used to calculate the various parameters is also given. Some of the predicted boundary layer parameters are not directly applicable to acoustics but are required inputs for calculation of other parameters. The most important parameters for the calculation of turbulence ingestion noise are the spectra and the integral length scale of the turbulence field.

Boundary Layer Thickness. Counihan (ref. 19) made an extensive survey of the literature on adiabatic boundary layers in 1975. He concluded that for neutral conditions, the depth of the boundary layer is independent of wind speed or surface roughness, and is approximately 600 m. Therefore for neutral conditions, the boundary layer thickness is assumed to be constant at 600 m. For unstable conditions the boundary layer varies from 1 to 2 km during the course of a day. Since no model exists to predict this diurnal variation, following reference 15 it is assumed here to be constant at 1500 m. For stable conditions, the boundary layer thickness is given by the following equations from Deardorff (ref. 20):

$$\delta = \left[\frac{1}{30L} + \frac{f_c}{.25\ U_*} + \frac{1}{Z_T}\right]^{-1} \qquad (1)$$

where $L = \dfrac{-T\ U_*^3}{g\kappa\ \overline{w\tau}}$ = Monin-Obukhov Length

Equation 1 must be solved iteratively in conjunction with Eq. (2) below to determine δ.

Friction Velocity. The friction velocity, U_*, is defined as $\sqrt{\tau_w/\rho}$. The friction velocity is described by the "geostrophic drag law":

$$\ln \frac{G}{f_c Z_o} = A + \ln \frac{G}{U_*} + \left[\frac{\kappa^2 G^2}{U_*^2} - B^2\right]^{1/2} \qquad (2)$$

where

G = Geostrophic wind speed

Z_o = Roughness length

κ = von Karman constant

Here, A and B are "constants" which are a function of the stability condition of the atmosphere:

1) Neutral Conditions $A = 1.7,\ B = 4.7$ (3)

2) Stable Conditions

$$A = \ln(\delta/L) - .96\ (\delta/L) + 2.5$$

$$B = 1.15\ (\delta/L) + 1.1 \qquad (4)$$

3) Unstable Conditions

$$A = \ln(-\delta/L) + (f_c\delta/U_*) + 1.5$$

$$B = \kappa/(f_c\delta/U_*) + 1.8\ (f_c\delta/U_*)\ \exp(.2\delta/L) \qquad (5)$$

Equation 3 is from Blackadar and Tennekes (ref. 21). Equations 4 and 5 are from Arya (ref. 22).

Mean Velocity Profile. As stated, the atmospheric boundary layer is typically 500 to 2000 m in thickness. Meteorologists have found that the best fit to the time mean velocity profile over the entire boundary layer is given by a power law of the form:

$$U/U_\infty = (Z/\delta)^p \tag{6}$$

The exponent, p, is described as a function of roughness height alone for neutral conditions by:

$$p = .24 + .096 \log_{10} Z_o + .016 (\log_{10} Z_o)^2 \tag{7}$$

For non-neutral conditions, the power law exponent is a function of both roughness height, Z_o, and stability length, L. Results of an analysis by Irwin (ref. 15) are shown in Figure 3. The Pasquill-Gifford stability classes shown in the figure are a broad classification scheme frequently used by meteorologists to categorize atmospheric diffusion.

Within the atmospheric boundary layer, there exists a sublayer, called the surface layer, where stresses and fluxes are nearly constant. This layer can be as thick as 150 m in neutral and unstable conditions, but can be as thin as 10 to 20 m under stable conditions.

In the surface layer, the logarithmic law is valid and a more accurate description of the mean velocity profile is given by the following equations for neutral, stable, and unstable conditions respectively:

Neutral Conditions

$$\frac{U}{U_*} = \frac{1}{\kappa} \ln \frac{(Z-d)}{Z_o} \tag{8}$$

where $d = 0$ for $Z_o < .2$ m

$d = H - Z_o/\kappa$ for $Z_o > .2$ m

H = Average rooftop height

Stable Conditions

$$U/U_* = 1/\kappa \left[\ln (Z/Z_o) + 5\ Z/L\right] \tag{9}$$

Unstable Conditions

$$U/U_* = 1/\kappa \left\{\ln(Z/Z_o) - 2 \ln\left[1/2 \left(1 + 1/\Phi_M\right)\right] - \ln\left[1/2 \left(1 + 1/\Phi_M^2\right)\right] + 2 \text{ TAN}^{-1} \left(1/\Phi_M\right) - \pi/2\right\} \quad (10)$$

where $\Phi_M = \kappa Z/U_* \, dU/dZ = (1 - 15 \, Z/L)^{-1/4}$

Integral Length Scales. The integral length scale is defined as

$$L_w^x = \int_o^\infty \tilde{R}_{ww}(r_x) dr_x \quad (11)$$

where $\tilde{R}_{ww} = \dfrac{\overline{w(x)w(x+r_x)}}{w^2}$

For neutral conditions, the integral length scale is a function of height only and is given by:

$$L_w^x = .4 \, Z \quad (12)$$

For stable atmospheric conditions, the following equation from Kaimal (ref. 23) is suggested:

$$L_w^x = .015 \, Z/R_i \quad \text{for } .05 < R_i < .2 \quad (13)$$

where R_i = Richardson number

$$= \frac{Z/L}{1 + 5 \, Z/L} \quad \text{for } Z/L > 0 \quad (14)$$

$$= Z/L \quad \text{for } Z/L < 0 \quad (15)$$

For unstable conditions, no correlation is available which takes into account stability parameters. Therefore, Equation 12 for neutral conditions is used. Strictly, the models for the integral length scale are valid only for the surface layer, typically the lower 10 to 20 percent of the boundary layer.

Under the assumption of isotropic turbulence, all longitudinal integral scales are equal to each other, as are the lateral integral scales, i.e.

$$L_u{}^x = L_v{}^y = L_w{}^z = L_u \tag{16}$$

and

$$L_u{}^y = L_u{}^z = L_v{}^x = L_v{}^z = L_w{}^x = L_w{}^y = L_v \tag{17}$$

Teunissen (ref. 14) has shown since all longitudinal correlations are equal and all lateral correlations are equal, and (from the continuity equation):

$$L_u = 2\ L_v \tag{18}$$

so that

$$L_u{}^x = 2\ L_v{}^x = 2\ L_w{}^x \tag{19}$$

Turbulence Intensity. The vertical component of the rms turbulence intensity $\sqrt{w^2}$ is given for neutral, stable and unstable conditions respectively by the following equations:

Neutral Conditions

$$\sqrt{w^2}/U_\infty = .5\ p\ \ln\ (30/Z_o)\ /\ \ln\ (Z/Z_o) \tag{20}$$

Stable Conditions (and Neutral)

$$\sqrt{w^2} = 1.25\ U_* \quad \text{for} \quad Z/L > -.3 \tag{21}$$

Unstable Conditions

$$\sqrt{w^2} = 1.9\ (-Z/L) \quad U_* \quad \text{for} \quad Z/L < -1 \tag{22}$$

Since these correlations are strictly valid only for the surface layer, following Counihan's (ref. 19) suggestion a linear interpolation is used between the value at the top of the surface layer (assumed to be 15% of the boundary layer thickness) to a value of .01 at the top of the boundary layer.

For neutral conditions, the longitudinal and lateral turbulence intensities are approximately:

$$\sqrt{u^2} = 2\ \sqrt{w^2} \tag{23}$$

and

$$\sqrt{v^2} = 1.5\ \sqrt{w^2} \tag{24}$$

For nonadiabatic atmospheric boundary layers, the horizontal velocity components do not obey Monin-Obukhov similarity (as the vertical velocity fluctuations do) and no simple formula to describe them exists at present.

Spectrum. The von Karman model was chosen to describe the turbulence spectrum. This model was chosen for several reasons. First, an isotropic model was selected since isotropy has been shown in an earlier subsection to adequately represent the atmospheric turbulence. Second, Teunissen (ref. 14) indicates that the von Karman model best "captures the features of scale length, total variance and the -5/3 slope". Teunissen also sites the work of Gunter et al. (ref. 18) to conclude that the von Karman model spectrum best fits the experimental data, at least for heights above the surface layer.

The von Karman model for the energy spectrum in isotropic turbulence is:

$$E(k) = \frac{Ik^4}{\left[1 + (k/k_E)^2\right]^{17/6}} \tag{25}$$

where

$$I = \frac{55}{9\sqrt{\pi}} \frac{\Gamma(5/6)}{\Gamma(1/3)} \frac{u^2}{k_E^5} = 6.25278\ u^2 L^5 \tag{26}$$

$$k_E = \frac{\sqrt{\pi}}{L} \frac{\Gamma(5/6)}{\Gamma(1/3)} = \frac{.746834}{L} \tag{27}$$

Atmospheric Turbulence Characteristics for Selected Acoustic Test Conditions

The model outlined above is very general, in that it can accommodate a wide range of inputs. In order to explore the effects of various atmospheric conditions on noise generated by a helicopter main rotor, some representative cases were selected. The following three parameters were chosen and held fixed:

1) latitude, $\theta = 45°$

This latitude is representative of the northern portion of the United States and also southern Europe.

2) roughness height, $Z_o = 0.02$ m

This is a typical runway condition (see for example ref. 15).

3) tropopause height, $Z_T = 11{,}000$ m

This is the tropopause height for the U.S. Standard Atmosphere, 1962.

The following three parameters were systematically varied in order to study their effect on rotor acoustics:

4) stability length, L = -10 m, ∞, and 20 m

Three values were chosen, -10, ∞, 20 m, representing unstable, neutral, and stable atmospheres. These particular values were chosen since they represent Pasquill - Gifford categories B, D, and F respectively. (Pasquill - Gifford stability classes are a broad classification scheme frequently used by meteorologists to categorize atmospheric diffusion and are described in reference 15.)

5) geostrophic wind speed, G = 2.6, 5.1, and 10.3 m/s (5, 10, and 20 knots)

The 5.1 m/s condition was chosen as a "baseline" since it represents a maximum, practical, acceptable limit for noise certification testing. The two other values were chosen to examine the effect of wind speed.

6) altitude, Z = 50, 122, and 152 m (164, 400, and 500 ft)

The 122 and 152 m heights were chosen, since they represent the approach and cruise height, respectively for the proposed noise certification test for helicopters. The 50 m height was chosen to see the effect of very low altitude flight.

Calculated Atmospheric Turbulence Characteristics

The effect of varying the stability length, wind speed, and altitude on the structure of the atmospheric boundary layer is shown in Figures 4 through 9.

The effect of stability length and wind speed on the boundary layer thickness is shown in Figure 4. For an unstable atmosphere, the boundary layer height is fixed at 1500 m while for neutral conditions, it is 600 m. The effect of stable stratification is to decrease the boundary layer height, while increasing wind speed thickens it. The deficiencies in the model are apparent since the sudden increase in boundary layer thickness from 600 to 1500 m as the atmosphere changes from neutral stability to slightly unstable is not physically justified.

The effect of stability length and wind speed on the friction velocity is shown in Figure 5. Friction velocity increases as stability length decreases. A rapid change is seen as neutral stability is approached. Increasing wind speed also increases the friction velocity.

Figure 6 shows how the vertical component of turbulence intensity varies with stability length and height. The largest values of intensity occur for the unstable atmosphere. In the neutral atmosphere, the turbulence is shear produced. Stable stratification acts to suppress this "mechanical" turbulence. On the other hand, unstable stratification produces "convective" as well as "mechanical" turbulence. In this case the flow is influenced by heat transfer and is in a state of free convection. For locations above the surface layer, an interpolation between the value at the top of the surface layer and a value of 0.01 at the top of the boundary layer has been assumed. The top of the surface layer has been assumed to be 15% of the boundary layer thickness. This value was chosen since it is typical for a neutrally stable atmosphere (ref. 15) and no simple formula for the surface layer thickness was found.

The effect of stability length and height in the boundary layer on the integral length scale is shown in Figure 7. For unstable conditions, the line for neutral conditions is assumed since there is no correlation presently available for unstable atmospheres. Stable atmospheric conditions are seen to suppress the integral length scale. Varying the stability length for stable atmospheres has little effect on the integral length scale.

The effect of stability length on the spectrum is seen in Figure 8. There is virtually no difference between the neutral and the stable conditions at high wavenumbers, although the peak in the spectra is shifted to the left with increasing stability length. The effect of altitude on the spectra is shown in Figure 9. A small increase in the amplitude of the spectra occurs with increasing altitude. Since the portion of the spectra relevant to rotor noise due to atmospheric turbulence ingestion errors at wavenumbers above the spectrum peak, differences at low wavenumber are of little interest here.

By using three different values for the stability length, wind speed and altitude, 27 different cases are possible. The matrix of atmospheric test conditions evaluated in the present study are shown in tabulated form in Table 1.

MEAN FLOW CONTRACTION MODEL

Introduction

To calculate the distortion of the atmospheric turbulence field as it convects toward the helicopter rotor, it is first necessary to develop an analysis which predicts the mean flow through the rotor. In developing this analysis, it is important to compare and evaluate the present approach with existing calculation procedures for helicopter flows.

In this connection, we note that much of the helicopter aerodynamic analyses are concerned with the details of the flow below (i.e., "downstream" of) the rotor, as it is this flow which interacts with the fuselage and tail rotor. For this reason, considerable work has been conducted on the structure of the vortex system that is shed from the rotor blades. Examples of these include Sadler (ref. 24), Reddy (ref. 25), Caradonna (ref. 26), Roberts and Murman (ref. 27), Thuy and Renaud (ref. 28), Landgrebe (ref. 29), and Egolf and Landgrebe (refs. 30 and 31).

In the present problem, however, the primary physical phenomenon to be addressed is the flow upstream of the rotor. A description of this flow is fundamental to calculating the distortion of the turbulence as it is ingested by the rotor. Details of the blade wake interaction or of the structure of the trailing vortex wake are less important, since these will not have a substantial effect on this upstream flow, Lighthill (ref. 32).

For this reason, a simpler approach to the computation of the mean flow can be adopted. Although this can not deal with all the complexities that exist in the real case it is useful to answer questions concerned with the deformation of the turbulence, which is the main object here.

The above considerations have been set out in some detail, since they are at the core of our approach to this problem. As was stated initially, the purpose of this effort is to provide the simplest physically relevant description of the different phenomena, and this concept is repeated throughout the description of the modeling.

The calculation procedure for the flow field induced by the rotor is described below. This flow field (referred to as the mean flow) provides a definition of the streamlines (or particle paths). These in turn are used to track the vortex filaments describing the turbulence and thus to determine the change in vorticity and wave number, between a station far upstream of the rotor disk and a station at the rotor face. In the concluding part of this section, the results of these flow computations will be presented for representative cases.

Wake Definition

The method used to calculate the mean flow into the rotor is to model the wake by a number of stationary, discrete vortices. A graphical representation of this is shown in Figure 10. Initially a two-dimensional calculation procedure was developed using line vortices. However, a more realistic three-dimensional description of the flow was subsequently implemented using discrete ring vortex elements. In all subsequent discussions, and predictions, it is this three-dimensional calculation procedure that will be referred to. It should be noted that although the individual vortex rings are axisymmetric, in all cases other than pure vertical ascent, the flow will, in fact, be three-dimensional.

Based on the above approach the total vector is determined by the superposition of the ring vortices plus the ambient flight velocity. In the calculations twenty vortex rings were used. The spacing was varied so that the vortices were placed closer together near the rotor disk (see Fig. 10), with the circulation per unit length (along the wake) constant to minimize flow leakage between vortex rings. The vortices extend to approximately five rotor diameters along the line of the wake. As will be shown in subsequent figures of the predicted streamlines, this vortex termination was sufficiently far downstream that it had only small effect on the flow upstream and in the vicinity of the disk.

All twenty ring vortices were the same diameter (equal to the rotor diameter). The wake model is therefore uncontracted and wake distortions are also neglected. As suggested by Lighthill, this will effect the flow locally but the overall character of the upstream velocity field should not be substantially affected.

The wake skew angle, χ, the angle between the normal to the rotor disk and the wake boundary, is defined by:

$$\chi = \tan^{-1} \left[-U_\infty \cos\alpha / (U_\infty \sin\alpha - V_o) \right] \tag{28}$$

where U_∞ = free stream velocity
α = rotor tip path plane angle of attack
V_o = induced velocity at the rotor from momentum theory

The strength of the vortices is found by matching the predicted induced velocity at the rotor face with experimentally measured model rotor data. These data were taken from cases reported by Landgrebe and Egolf (ref. 33). The rotor tip path plane angle of attack, α, (the angle between the rotor plane and the free stream direction) was also taken from these references. Experimental measurements were available for only a few operating points,

generally hover, and moderate speed forward flight. For other operating points, induced velocity and tip path plane angle of attack were extrapolated using analytic expressions for helicopter aerodynamics from Gessow and Myers (ref. 34).

From momentum theory for helicopter aerodynamics, the rotor induced velocity is:

$$V_o = \frac{\Omega R C_T}{2\sqrt{\mu^2 + \lambda^2}} \tag{29}$$

where μ = rotor advance ratio

$$= U_\infty \cos\alpha / \Omega R \tag{29a}$$

and λ = rotor inflow ratio

$$= (U_\infty \sin\alpha - V_o)/\Omega R \tag{29b}$$

Combining Equations 29, 29a, and 29b yields:

$$\frac{C_T^2 (\Omega R)^4}{4 V_o^2} = (U_\infty \sin\alpha - V_o)^2 + (U_\infty \cos\alpha)^2 \tag{30}$$

Given C_T, ΩR, α, and U_∞, this equation can be solved iteratively for V_o. This induced velocity from helicopter aerodynamics theory is then used to set the vortex circulation strength, Γ, for the twenty ring vortices (see subsection below). The correct value for Γ is found by iteratively varying the vortex circulation strength until the induced velocity predicted by the ring vortex solution matches the induced velocity, V_o, determined from equation 30.

Vortex Model

As stated, the rotor wake is described by a series of twenty ring vortices, along the (possibly skewed) line of the wake. The potential velocity for a ring vortex is given by Kuchemann and Weber (ref. 35) and by Castles and De Leeuw (ref. 36). The axial and radial velocities at any point are expressed by:

$$V = \frac{\Gamma}{2\pi x R}(AB + CDF) \tag{31}$$

$$V_R = \frac{-\Gamma}{2\pi x R}(AB' + CDF') \tag{32}$$

where $A = K(\tau) - E(\tau)$ (33)

$$B = \frac{x-1}{d_1} + \frac{x+1}{d_2} \tag{34}$$

$$C = d_1 + d_2 \tag{35}$$

$$D = \frac{\tau\, E(\tau)}{1-\tau^2} \tag{36}$$

$$F = 1 - \frac{(1 + x^2 + z^2) - d_1 d_2}{2x^2} - \frac{(1 + x)d_2^2 - (1 - x)d_2^2}{2x d_1 d_2} \tag{37}$$

$$B' = z(1/d_1 + 1/d_2) \tag{38}$$

$$F' = \frac{z}{x}\left[1 - \frac{1 + x^2 + z^2}{d_1 d_2}\right] \tag{39}$$

$$d_1 = \sqrt{z^2 + (x-1)^2} \tag{40}$$

$$d_2 = \sqrt{z^2 + (x+1)^2} \tag{41}$$

$$\tau = \frac{d_2 - d_1}{d_2 + d_1} \tag{42}$$

x = radial distance from the axis of the vortex ring nondimensionalized by the ring radius

z = axial distance from the plane of the vortex ring nondimensionalized by the ring radius

$K(\tau)$ = complete elliptic integral of the first kind

$$= \int_0^{\pi/2} \frac{1}{\sqrt{1 - \tau^2 \sin^2\alpha}}\, d\alpha \tag{43}$$

$E(\tau)$ = complete elliptic integral of the second kind

$$= \int_0^{\pi/2} \sqrt{1 - \tau^2 \sin^2\alpha}\, d\alpha \tag{44}$$

For any given rotor operating condition, the velocity is obtained by superposition of the induced velocity of each of the twenty vortex rings.

Computational Procedure for Streamline Tracing

Given the helicopter operating parameters, the procedure described above can be used to compute the velocity at any station in the flow field. The resulting rotor induced flow can then be used to calculate the flow streamlines which control the distortion of the upstream atmospheric turbulence as it is entrained by the rotor. The following discussion describes the streamline prediction while the next section (Turbulence Contraction Model) defines the distortion process.

A streamline can be computed by integrating the streamline equations, which are:

$$dx = u\,dt \tag{45}$$

$$dy = v\,dt \tag{46}$$

$$dz = w\,dt \tag{47}$$

Starting at a given station these expressions can be integrated forward or backward in the time domain to predict the next streamline position. Equations 45 through 47 are three coupled nonlinear ordinary differential equations. A computer subroutine, written by Shampine and Gordon (ref. 37) was used for the numerical integration. This method uses a modified divided difference form of the Adams-Pece formulas and local extrapolation. It adjusts the order and step size to control the local error per unit step in a generalized sense.

In practice, one is only interested in streamlines which pass through the rotor disk, and the upstream location of these is not known. It was thus convenient to begin the calculation at the rotor and integrate upstream (i.e., backwards). The computations were stopped when the streamlines reached a point outside of a three rotor diameter cube centered on the rotor. Beyond this station the streamlines are essentially straight and the velocity magnitude is essentially constant.

Selection of Test Cases

Calculations were performed for several test cases to show the sensitivity to rotor operating conditions. The cases examined are hover, vertical ascent, and forward flight with specific operating parameters listed in Table 2. Figure 11 shows the locations of the ring vortices in the helicopter wake for the cases examined. The physical dimensions of the rotor and the helicopter operating conditions in Table 2 were chosen to match experimental data of Miller, Tang and Perlmutter as reported by Landgrebe and Egolf in reference 33.

Before describing the specific results, some discussion of the basis for selection of these conditions is appropriate. In addition it is also necessary to define in a more precise manner what is meant by "hover". Here the term indentifies a condition where the aircraft is stationary relative to the ground. This appears to be a more readily recognizable condition than being stationary with respect to the fluid, and is the condition that is called out in noise specifications.

Having said this, the "conditions at infinity" in the hover situation are thus determined by the ambient wind velocity which was selected to be 5 knots (2.57 m/s). This also implies that the mean flow for the hover condition is not at all axisymmetric, but instead three-dimensional.

The above definition of hover, which correctly models actual test specifications, also removes a potential source of ambiguity in modeling the rotor inflow. The ambiguity has to do with the ambient level of turbulence, which is the external forcing function for the noise. The turbulence intensity is specified as a fraction of the mean velocity. However, if the aircraft moved with the mean wind velocity then the relative velocity far away from the rotor would be zero. The fundamental assumptions on which the turbulence contraction model to be described in a following section are based (the turbulent velocities being much smaller than the mean velocities) would no longer be valid, and the contraction ratio (mean velocity at the rotor face divided by the mean velocity at "infinity") would be infinite. There is no real body of methods that have been developed for dealing with such cases. Thus, on grounds of "practicality" as well as of ability to model, we have excluded this singular situation from consideration.

Although the hover condition defined above is not axisymmetric, the flight conditions of pure vertical ascent are. In practice, if the rate of ascent is substantially larger than the ambient wind speed, the flow into the rotor disk will be approximately axisymmetric. This condition permits examining the turbulence ingestion process for an axisymmetric flow into the rotor. (This is essentially the empty wind tunnel contraction geometry.)

Whereas the conditions of hover and vertical ascent generally exhibit a significant contraction of the streamlines as fluid is entrained by the rotor disk, under forward flight conditions a primary feature on the flow is turning of the streamlines, rather than streamline contraction. Therefore differences are expected between the streamline trajectories for forward flight and vertical ascent in addition to differences in the contraction ratio.

Calculated Mean Flow Velocity Field

To examine the mean flow features for the different flight conditions, streamlines and timelines (which are material lines) were plotted for a number of cases. Representative calculations are shown in Figures 12 through 20.

An evaluation of the vortex ring superposition model (Fig. 10) used to define the flow through the rotor is given in Figure 12. This shows the streamlines (solid) and timelines (dashed) in a vertical plane through the center of the rotor disk, for the slow forward flight case. The position of the rotor disk is marked by the heavy solid line.

Although the streamlines in Figure 12 are wavy near the discrete vortices in the wake, streamline trajectories at a distance of one vortex spacing from the vortex contours are smooth. In addition, the streamline pattern indicates little if any flow through the interface line formed by the vortex rings. This demonstrates that the wake skew angle has been chosen correctly. These calculated features establish the consistency of the mean flow model adopted here.

Sensitivity of the overall flow features to changes in the flight conditions can also be evaluated. Figure 13 shows the projection of the so-called capture surface on a vertical plane through the center of the rotor for the six flight conditions that are reported here. (The capture surface is the dividing stream surface between fluid that passes through the rotor disk and fluid which does not.) Note that there is a large variation in the contraction ratio, from far upstream to the rotor disk, as the rotor operation changes from hover (as defined in the present report) to vertical ascent, and finally to fast forward flight.

Figure 14 shows another view of this streamline envelope as the rotor changes operation. Here the capture area is projected onto a plane normal to the flow at "infinity", for the six flight conditions. In both Figure 13 and 14 the strong asymmetry of the forward flight cases is evident.

In Figures 15 through 20 four different views of the streamlines and timelines are given for each of the six operating conditions. Figures 15 and 16 show the fast forward and slow forward flight conditions while Figure 17 shows the pseudo-hover operation condition. Figures 18, 19 and 20 show the slow, medium, and fast vertical ascent cases.

In each of these figures four views are given: a) a view of the streamlines in a vertical plane parallel to the velocity at infinity and passing through the center of the rotor disk, b) a top view of the streamlines emanating from the perimeter of the rotor disk, c) a view perpendicular to view a, d) a three-dimensional perspective view from an observer location 20 degrees above and 70 degrees from the ambient wind velocity direction. These views show all streamlines bounded by the 95% location circumference of the rotor. Streamlines beyond this region cannot be calculated since the wake model breaks down at the tip (infinite velocities are predicted at the core of the ring vortex used to model the wake).

In Figure 15 very little turning of the streamlines occurs. In Figure 16 some turning of the streamlines is apparent. The flow which enters the forward most part of the rotor disk starts in the freestream from a location below the disk. In Figure 17, a large amount of both turning and stretching of the timelines is evident in the figures.

At the highest vertical ascent case, shown in Figure 18, with a vertical velocity of 6.1 m/s, there is virtually no contraction or turning. The flow from the freestream enters the rotor disk undistorted. In this case, we would expect that the turbulence would also be unaffected. At the lowest vertical velocity case shown in Figure 20, however, the flow has large amounts of both contraction and turning.

Aside from the large differences in streamline patterns another important feature seen in Figures 15 through 20 is the relation of the time lines to the streamlines. At far upstream locations the two are orthogonal, however, near the rotor, in the cases where there is substantial turning of the streamlines, there is a significant departure from orthogonality. In other words, the timelines can become tipped into the local streamwise direction. This point, which has important implications for the evolution of the turbulence as it is ingested, will be discussed further in the next section.

TURBULENCE CONTRACTION MODEL

Introduction

The mean flow model developed in the previous section controls the distortion of the atmospheric turbulence as it is ingested by the rotor. Modeling this turbulence distortion in a completely general manner and describing the alteration of the turbulence field as it convects into the rotor would require solving the unsteady Navier-Stokes equations for each flight condition of interest. Such a calculation is currently not feasible, but (as described previously) even if it were possible, it would be inconsistent to pursue in light of other approximations made in the calculation procedure.

Based on this conceptual observation, a basic question arises as to which analytical model provides the required accuracy for treating the turbulence distortion problem. One approach is to use "Rapid Distortion Theory" for calculating the evolution of the turbulent flow. This is an approximate analysis which has been applied to computations of turbulence in many different situations. The assumptions inherent in this approach will be spelled out in more detail below. Basically the analysis models the flow field in terms of a primary flow, induced by the rotor, which convects (and distorts) vortex filaments which are used to represent the turbulence. The rapid distortion approach thus accounts for the inherently three-dimensional processes of vortex stretching and tilting, which can change both the frequency distribution and the intensity of the turbulence. A further advantage of using Rapid Distortion Theory is that the consequences of the assumptions are known, permitting direct assessment relative to the other approximations employed in the present study.

Background

The central concepts on which Rapid Distortion Theory is based were developed by Prandtl and G. I. Taylor, and have been known in a qualitative sense for over fifty years. The first extensive quantitative applications of these ideas were by Ribner and Tucker (ref. 38), and Batchelor and Proudman (ref. 39). These studies resulted in the development of approximate procedures to calculate the changes in the Fourier coefficients of the turbulence spectrum due to passage through a contraction.

The two analyses mentioned are similar in that both made use of Cauchy form of the vorticity equations (ref. 40) (or the integral of these equations) to relate the components of the vorticity at any two points on a streamline. Both analyses are linearized, in that the flow is viewed as composed of a steady mean flow with a vorticity perturbation superimposed on it, the latter being responsible for the turbulence velocity field.

The basic concept of the Rapid Distortion Theory is to relate the components of the vorticity at given locations along a streamline. In a linearized

rapid distortion analysis, these streamlines (along which the fluid particles are converted) are streamlines associated with the mean flow. Thus, the vortex filaments are regarded as being convected by the mean flow. The velocities induced by the perturbation vorticity are neglected in considering the deformation of the vortex filaments.

The applications reported in references 38 and 39 refer to problems in which the differences in drift time of the fluid particles through the contraction could be neglected. (Drift time is defined as the length of time for a fluid particle to be convected along a streamline from an upstream to a downstream station.) In addition, as will be described below, changes in the vorticity due to viscous dissipation were not modeled. Further, the flow fields calculated did not satisfy the boundary conditions that would exist on the bounding surfaces of the wind tunnel contraction section for which the analysis was developed.

A significant extension of the capabilities of these theories was carried out by Hunt (ref. 41). His starting point was also the linearized form of the Cauchy vorticity equations. However he treated the situation in which different particles take different times to be convected (drift) past an obstacle or through the region of interest. Under this condition, the turbulence vorticity field is distorted due to turning of the streamlines even if there is no net contraction of the streamlines.

The basic mechanism associated with distortion due to turning can be illustrated in Figure 21. The figure shows a vortex filament being convected through a constant area bend. The line AA' represents the vortex filament at a location upstream of the bend, while BB' describes the filament at the downstream location.

Since the mean flow is irrotational the fluid particles on the inside of the bend travel faster than those on the outside.* Particles on the outside of the bend also have a larger distance to travel because of the larger radius. For these reasons, particles at B will lag those at B', and the vortex line (which is also a fluid or material line) will be rotated into the streamwise direction resulting in an increase of the vortex filament length.

Associated with the vortex line is a vorticity vector which represents the turbulence level. This vector remains aligned with the vortex filament as it is convected through the bend. In the upstream location the vector is transverse to the flow but downstream of the bend both transverse and axial components of vorticity exist. Similar to the increase in vortex filament length due to rotation, the transverse magnitude of the vorticity vector increases.

* The irrotationality condition can be written in terms of natural coordinates as $\delta q/\delta n = q/r$, where n denotes the direction of the principal normal to the streamline (directed towards the center of the curvature), q is the magnitude of the velocity, and r is the local radius of curvature of the streamlines. Thus as one moves radially outward in the bend, the velocity decreases.

Finally, creation of the streamwise component of vorticity brings with it a secondary circulation, which causes motion in a direction perpendicular to the primary flow.

Although the concepts of secondary flow have been described in terms of flow through a bend, the general physical principles associated with the existance of this secondary vorticity have a much wider application. As an example, models with secondary flows are needed to calculate three-dimensional flows in turbomachines (refs. 42, 43 and 44), to calculate the flow field associated with inlet vortices (ref. 45), and to predict the flow around struts and wing-body junctions (ref. 46). However, we have described it here at some length, since it may be less familiar in the present context, and since it is an important part of the present problem.

Hunt's extension of the theory was not limited to the incorporation of the effect of turning. In addition to modeling this phenomenon, he described the procedures needed to satisfy the analytical boundary conditions. These are essentially the solution of three Poisson equations for the part of the velocity field that is associated with the vorticity distribution and the solution of Laplace's equation for the additional part of the velocity field necessary to satisfy the boundary conditions.

The procedure, along with calculations for some cases having simple geometry, was described by Hunt in references 47 and 48, in addition to comparisons with experiments. A review of the basic assumptions and regimes of applicability of the theory is given in reference 48.

More recently, Goldstein (ref. 49) reformulated the problem using a generalized analysis based on an alternative velocity field decomposition which has several attractive features. The perturbation velocity field is regarded as composed of contributions from the vorticity field (which contains no pressure information) and an additional part, which is irrotational, but which satisfies a Poisson's equation and the relevant boundary conditions. The vorticity field contribution can be found from knowledge of the far upstream vorticity distribution and the mean flow, so that the procedure involves solving only a single Poisson equation rather than the three described in the previous paragraph. Goldstein has applied this procedure to several cases of practical interest (ref. 49), and Goldstein and Durbin (ref. 50) have extended the analysis to account for finite wavenumbers.

One of the most important questions addressed in Reference 50 was the effect of wavenumber (of the turbulence) on the amplification of velocity fluctuations through a contraction, a problem which is not within the scope of the "classical" treatments of rapid distortion theory. It was demonstrated that there are significant effects when the turbulence length scales are of the same order as the mean flow length scales .

Another recent approach to this problem is by Tsuge (ref. 51), who examined the influence of wavenumbers on the properties of a turbulent velocity field after a contraction. An analysis was developed for a simple mean flow field, such as would occur near the axis of a straight section wind tunnel. Under these conditions a simplified calculation procedure was developed, which provided insight into the manner in which the turbulent velocity field is altered by the contraction.

It is worthwhile to comment briefly on the different phenomena which are described by these recent theories (and by the present analysis) and compare the treatment to those that are inherent in the original treatments of Ribner and Tucker (ref. 38) and Batchelor and Proudman (ref. 39). One of these is connected with the stretching and tipping of vortex filaments due to the differential "drift" (Lighthill, ref. 52) of fluid particles on different streamlines. This is associated with the time history of the fluid particles, and (locally) is independent of the velocity perturbation-boundary turbulence scale.

There are other effects, however, which do depend on the scale of the turbulence (Goldstein and Durbin (ref. 50), Hunt (ref. 48), Hunt (ref. 41), Tsuge (ref. 51).) These arise because of: 1) the fact that the downstream vorticity field (as well as the vorticity field in the contraction) is spatially non-uniform, and 2) the velocity perturbation-boundary interaction between the vorticity induced flow field and the boundaries.

The first of these effects implies that there is no simple vorticity/-velocity relation, as there would be if the vorticity distribution were homogeneous. Rather to find the velocity, one must sum the perturbation velocity vectors from vortex elements over all space. In practice, this implies that the integration must be taken over a scale larger than the scale of the turbulence. It also means that only for small turbulence scales (compared to the scale of the contraction) can the velocity/vorticity relation at any point be regarded as the same as that which would exist in a homogeneous flow having that distribution of vorticity. The second of these conditions implies that there will be velocity perturbations due to the presence of the boundary and that, (very crudely) at distances from the boundary of less than the scale of the turbulence, this interaction should be taken into account.

It is important to point out that in this study turbulence scales (the integral length scale) are considered to be substantially less than the scale of the contraction. This will in fact be the case for the wavenumber components of the turbulent field which are of most interest. Thus, features of the turbulence ingestion process which are dependent on scale are not treated. Instead the study concentrates on the part of the phenomenon that is associated with the kinematics of the vorticity field. As will be seen below, this permits a simplified description of the velocity field. It should be emphasized, however, that the main justification for treating only small turbulence scales is not the analytical simplification but rather the relation between the length scales of the contraction and of the turbulence.

Another aspect that the basic ("classical") rapid distortion approach does not account for is the effects of viscosity. An approximate correction for this is to assume that turbulence decays without distortion of the flow. According to Hunt (ref. 48), this tends to underestimate the decay. It should be noted however that, depending on the Reynolds number regime, the effects of viscosity can often be quite small for the turbulence wavelengths of interest.

In the present treatment, no attempt is made to apply a viscous correction. This is done for several reasons. First, a primary point of the present investigation is to examine the importance of effects on the turbulence that are inherently three-dimensional in nature. The resulting conclusions should not depend strongly on whether or not viscous effects are included, especially if they are only included in an approximate fashion. Second, the shortest wavelength, (or the smallest eddies that are of interest in the present investigation) still have reasonably high Reynolds numbers (greater than 100) so that viscous effects can be expected to be small. Third, it is not at all apparent in the present situation that the approximations used for wind tunnels are appropriate.

In a wind tunnel the turbulence is created by a screen or upstream obstacle, and decays as it is convected downstream. Thus the turbulence level of a given fluid element should decrease with time. In the present situation there is a production of turbulence in the ground boundary layer, and hence an equilibrium between the production and decay of turbulence. It is really the difference between this equilibrium state and the instantaneous state of the turbulence undergoing the distortion that is indicative of the importance of viscous effects. If this difference is "small" then the influence of viscous effects are also small. If this difference is "large", then the state of the turbulence is far from the equilibrium, and the process of viscous decay towards the equilibrium may be of significance.

Although these concepts are qualitative, one point that can be made is that the equilibrium state in the present situation is not one of zero turbulence. Presumably, therefore, the influence of viscosity will (for a given distortion geometry) be less important than in the wind tunnel situation. However, the magnitude of the differences is a subject for future investigation.

We have described the theoretical concepts associated with rapid distortion theory. Experiments have been carried out to assess the range of applicability of this type of analysis. Two recent studies are those of Tan-Atichat and Nagib (ref. 53), and of Britter, Hunt, and Mumford (ref. 47).

The general conclusions derived from these investigations are that if the theoretical conditions are satisfied, then Rapid Distortion Theory is a useful method for predicting the evolution of a turbulent flow. Two possible sources of the descrepancies that do exist between theory and experiment are nonlinear effects, and effects of viscous dissipation. We will discuss the importance of these relative to the present study in the next section.

Criteria for Application of Rapid Distortion Theory

As reviewed in some detail by Hunt (ref. 48), the basic conditions that must be met for Rapid Distortion Theory to apply are:

1) the turbulence intensity is small, i.e.

$$\frac{u_o'}{U_o} \ll 1$$

where u_o' is some measure of the turbulence velocity amplitude and U_o is a velocity that characterized the mean flow field.

2) the "overturning time" for a turbulent eddy is much larger than the time for the distortion (contraction in our case) of the mean flow. Explicity this can be written as,

$$\frac{\text{distortion time}}{\text{overturning time}} = \frac{L_c}{\ell\ \Delta U_o} \ll 1$$

where ℓ is the spatial integral scale of the streamwise component of turbulence, L_c is a characteristic length over which the mean flow changes, and ΔU_o is a representative mean flow velocity change.

Selecting the appropriate length scale requires careful consideration. If the mean flow is irrotational, as it is in many practical cases, there is no natural length scale in the governing equation (Laplace's equation). The appropriate length to characterize the flow non-uniformity will thus be of the same order as the geometric length scale of the problem. For our problem the geometric scale is represented by the region where there is significant streamline curvature, and hence distortion of vortex filaments. The size of this region is of the order of the capture streamtube dimension, which is denoted by H. (In the present problem H is also of the same order as the rotor diameter, D.) The condition for the applicability of Rapid Distortion Theory is thus that the quantity

$$\frac{Hu'_o}{\ell \Delta U_o} \quad \left(\text{or} \quad \frac{Du'_o}{\ell \Delta U_o} \right)$$

should be small.

3) The Reynolds' number associated with the turbulence is large, i.e.

$$\frac{u'_o \ell}{\nu} >> 1$$

Now that we have described the conditions that must be met, we can examine the extent to which they are obeyed in the present problem.

1) The condition $u'_o / U << 1$

At the proposed noise certification height for helicopters (152 m) for typical runway conditions (Z_o = 0.02 m) and a neutral atmosphere, Equation (16) predicts (see Table 1) an rms turbulence intensity of 5% of the mean wind. Hence if we consider a helicopter with zero velocity relative to the ground the condition is well fulfilled. At cruise, helicopters typically travel an order of magnitude faster than wind speeds. Even allowing for the change in mean velocity from far upstream to the rotor face this implies that for typical forward flight cases the ratio of u'_o/U will be less than for zero velocity. Hence we can regard this condition as being obeyed in essentially all cases of practical interest.

2) The condition $Du'_o / \ell \Delta U_o << 1$

From Equation (11) the integral length scale is approximately 60 m and the time scale is approximately 35 s. Using the rotor diameter as the length scale for the contraction this ratio becomes 0.12 for a Sikorsky S76 helicopter at cruise. At the condition of zero velocity relative to the ground, the ratio is 0.013 which is slightly larger, but still much less than unity.

Although the above criteria can be satisfied, it is useful to examine this condition in more detail. The wavelengths of interest include wave numbers considerably higher than the wave numbers which characterize the integral length scale. Therefore, it is necessary to look at the equations of motion to see what the accuracy of the Rapid Distortion Theory approximation is.

The inviscid vorticity transport equation can be written as:

$$\boxed{\frac{D\vec{\omega}}{Dt} = (\vec{\omega}*\nabla)\vec{U}} + (\omega*\nabla)\vec{u}' \qquad (48)$$

where the bars denote mean flow quantities and the primed variables denote the turbulence. The terms within the dashed lines are those that are considered in Rapid Distortion Theory, and the other terms account for nonlinear effects, i.e., the convection of perturbation vorticity by perturbation velocity.

For turbulence of a given wavenumber, k, the ratio of the nonlinear term to the terms within the dashed lines is roughly

$$kD \frac{u_o'}{\Delta U_o}$$

Hence, in order to have these effects small, the parameter $kDu_o'/\Delta U$ should also be small.

Consider the shortest wavelength of interest in the present problem (wavelength equal to the rotor blade thickness), and let us estimate the parameter. The characteristic velocity of the turbulence is now less than u' and, assuming that the spectrum has (locally) a $k^{-5/3}$ behavior, can be estimated to scale (see ref. 54) as:

$$U_k \propto k^{-1/3}$$

The quantity $kD/\Delta U_o$ would thus scale as $k^{2/3}$, so that at the above condition, we should, in fact expect that the nonlinear effects might start to be important. However, it is to be emphasized that this is only at the upper end of the wave numbers that are considered where the amplitude is smallest, and that over most of the range of interest, the basic assumptions may be quite valid. It seems, however, that an important point for future research is to resolve how critical this condition for nonlinearity to be absent is, especially in the case where the wavelengths of interest are less than an integral length scale.

3) The condition $u_o' \ell / \nu \gg 1$

For a 3 m/s wind, u_o' is 0.15 m/s. Hence the turbulence Reynolds number is 10^4 per meter. If the relevant length used is the integral length, this value is 6×10^5. Even for the shortest wavelengths that are of interest, this number is greater than 100 so the viscous effects would be expected to be small.

VORTICITY FIELD AND SPECTRUM OF TURBULENCE UNDERGOING A RAPID DISTORTION

Previous sections have described the general approach to be used for assessing the effect of the contraction of the turbulence and the mean flow model. The present section presents the details of the procedure for calculating the evolution of the turbulence as it is convected towards the rotor. Changes occurring in the vorticity of a fluid particle as it is convected as well as the alterations that occur in the wavevectors that characterize the local spectrum of the turbulence are described. The analysis presented is shown to reduce to that of Ribner and Tucker if certain restrictive assumptions are made about the class of contractions considered. Finally numerical results are shown for the vorticity distribution at the rotor face, both for the present calculation procedure and for the classical (Ribner-Tucker) type of analysis.

General Background

A general turbulent velocity field for incompressible flow can be expressed as a distribution of vorticity superimposed on a potential flow field. For an inviscid constant density flow, vortex lines move with the fluid in which they are embedded. Thus any deformation of the fluid will distort the vortex lines of vorticity, and in a contracting stream the vortex filaments will be stretched and tilted, affecting the velocities induced by the vorticity.

One of the simplest types of deformations of such a turbulent field to consider is one in which a fluid element undergoes pure contraction or extension along the three coordinate axes, with the x axis being the streamline direction. A one-dimensional duct flow would give this type of deformation. (If there were unequal deformations in the two transverse dimensions, the y and z axis would need to be oriented along the principal directions in this plane if the strain is to be characterized as pure contraction or extension.) The axes of this coordinate system will remain orthogonal after the deformation. Denoting the upstream coordinates by x_i and the downstream coordinates by ξ_j (see Fig. 22), the deformation tensor denoted by $\partial x_i/\partial \xi_j$ will be diagonal for this case. This is the type of deformation to which the analysis of Ribner and Tucker (ref. 38) is directly applicable. Although this model is the simplest to visualize, it is generally the exception rather than the rule for real flows. A duct flow which undergoes a rapid contraction will not be one dimensional; it will have significant streamline curvature for off-axis locations. This will lead to non-zero velocity gradients in the direction normal to the streamlines which will give skewing and shear to a cube of fluid initially oriented parallel to the streamlines.

Ribner and Tucker determined the effect of contraction on an individual spectral component (a sinusoidal gust) of the turbulence. As discussed above assuming the contraction to be rapid, the interaction effects between the various turbulence spectral components can be ignored, as can the viscous effects. The vorticity then moves with the mean flow; once the flow is specified, the downstream vorticity, and thus the turbulence, is determined.

Ribner and Tucker considered only the case of a diagonal deformation tensor. The present analysis, taken from reference 55, is for the case of a general deformation tensor; the only restriction is that the determinant of the deformation matrix be unity, i.e., that the flow is incompressible. The details of the analysis are given in the Appendix.

It can be noted that the results of Ribner and Tucker are still applicable to the present geometry if a transformation to principal axes is first performed. A general matrix can be expressed as a sum of an antisymmetric and symmetric matrix, with the antisymmetric matrix representing pure rotation. If this were the only part of the deformation tensor, by suitable rotation of the downstream coordinate system a small fluid volume would appear to be unaffected by the deformation; the shape of the volume would be the same, and the fluid particles lying on the three axes upstream would lie on the corresponding three axes downstream. If now a symmetric matrix is added to the antisymmetric matrix (giving a general matrix), the coordinate rotation required by the antisymmetric matrix must be followed by a further coordinate transformation to the principal strain directions before the analysis of Ribner and Tucker can be used. In this final coordinate system the fluid particles lying on the three upstream axes will not lie on the corresponding downstream axes.

Application of the Ribner and Tucker analysis to calculate the effect of a general deformation on a Fourier component of the turbulence velocity field would thus require the deformation to be decomposed into a fluid rotation (3 quantities), the directions of the principal axes (3 quantities), and the amount of contraction or extension along each axis (3 quantities). (These quantities are just another representation of the nine derivatives in the deformation tensor.)

A different approach was used here for the analysis. Starting with the general expression due to Cauchy (ref. 56, p. 205) for the transport of vorticity in Lagrangian form the analysis is formulated in the same manner as the Ribner and Tucker approach, but without the restrictive assumption of a diagonal deformation tensor.

The basic equation for the vorticity at any location in terms of the initial vorticity contained by a given fluid particle is (ref. 56, p. 205)

$$\Omega_i^U = \Omega_j^D \frac{\partial x_i}{\partial \xi_j} \tag{49}$$

or

$$\Omega_i^D = \Omega_j^D \frac{\partial \xi_i}{\partial x_j} \tag{50}$$

where x_i represents the upstream coordinate system and ξ_i, represents the downstream coordinate system at the rotor face. The derivative $\partial x_i/\partial \xi_j$, is called the deformation tensor since it is related to the deformation of a volume of fluid as it moves from upstream to downstream. For example, if one starts with an infinitesimal cubical volume of fluid upstream, this will distort to a parallelepiped downstream. Denoting the three upstream length scales of the upstream volume by Δx_j, the vertices of the downstream volume will determine $\Delta \xi_i$, and thus, the tensor $\partial \xi_i/\partial x_j$; that is the inverse of the matrix used in Equation (49). The superscripts U and D in Equation (49) denote upstream or downstream conditions respectively.

The analysis below will show the specific details of the relation between upstream and downstream velocity that is implied by Equation (49). It suffices here to emphasize that it is the deformation tensor, $\partial x_i/\partial \xi_j$ that plays a key role, and which is necessary to evaluate for the three-dimensional flows under consideration.

In order to do this the streamline tracing procedure described in the Section "Mean Flow Contraction Model" is used. Starting at a given point on the rotor face the equations describing the streamline coordinates are numerically integrated to trace a streamline from the rotor face to a far upstream location, taken here to be three radii from the rotor hub. A second streamline starting a distance $d\xi_1$ from the first is then also traced for the same length of time as the first. At the upstream end of these streamlines a vector is drawn from the end of the first streamline to the end of the second. This vector determines three of the nine components of the deformation tensor; $\frac{\partial x_1}{\partial \xi_1}, \frac{\partial x_2}{\partial \xi_1}, \frac{\partial x_3}{\partial \xi_1}$.

The process is repeated for two other streamlines displaced a distance $d\xi_2$ and $d\xi_3$ respectively from the initial one, to yield the other six components of the distortion tensor. Thus four streamlines are calculated for evaluating the deformation tensor at each point of the rotor face.

Once this is done, the matrix $\left[\frac{\partial x_i}{\partial \xi_j}\right]$ can be inverted to obtain the nine quantities $\partial \xi_i / \partial x_j$. However, as described below, it is often more convenient to work "backwards" from the rotor face to an upstream station. The derivative evaluation used here is a simple scheme which is accurate to first order. However trial runs showed that the desired accuracy can be readily achieved by taking small enough values of the distances $d\xi_1$, $d\xi_2$, and $d\xi_3$; and these typically were 0.0001 of the radius.* While other more elegant variations of the present process are possible (such as writing the equations for the rate of change of the deformation tensor and then integrating this numerically along a streamline) the simple direct procedure seems adequate for the calculation at its present level of sophistication.

Because turbulence is expressed as a second order tensor, the transformation from the upstream to the downstream spectrum will involve transforming two rather than one vector quantities. The first of these vectors represents the fluid velocity of a Fourier component of the turbulence. The second vector quantity is the wavevector of the turbulence component. Both vectors are transformed using the principle that the vortex lines are convected by the mean flow.

The resulting analytical expressions have been coded in a computer program allowing the calculation of the downstream values of the vector velocity and wavevector given the corresponding upstream values. The only inputs necessary are the 9 quantities in the deformation matrix relating the upstream and downstream points. The program allows the user to specify the downstream values of wavevector and velocity vector and then calculate the upstream values, rather than the inverse. This approach was selected based on the final intended application of the program. The intent is to calculate the noise produced by turbulent flow into a propeller or helicopter rotor; for this purpose one must be able to specify a particular wavevector component of downstream turbulence at the rotor face and calculate its magnitude from the corresponding upstream component, rather than specifying the upstream wavevector and calculating the corresponding downstream wavevector. If a diagonal matrix is input for the deformation tensor, the results of the program agree with those of Ribner and Tucker.

---

* The accuracy of the derivatives can be assessed by examining the determinant $\left|\frac{\partial x_i}{\partial \xi_j}\right|$. This will have the form $\left|\frac{\partial x_i}{\partial \xi_j}\right| = 1 + O(d\xi)$

Analysis

The object of the following analysis is to relate the upstream and downstream spectrum functions. Because of the tensor representation of the turbulence, the relation between the two spectra is relatively complex. The following analysis is a summary of that given in reference 55. This reference also contains the computer programs described in the introduction of this section.

Relations Between Vorticity and Velocity at a Point. The spectrum of turbulence is described in terms of Fourier gust components as given in Equations 51 and 52 below. For a single Fourier component:

$$\underline{q}(\underline{k},\underline{x}) = \underline{Q}(\underline{k})e^{i\underline{k}\cdot\underline{x}} \tag{51}$$

$$\underline{\omega}(\underline{k},\underline{x}) = \underline{\Omega}(\underline{k})e^{i\underline{k}\cdot\underline{x}} \tag{52}$$

These relations are expressions for the velocity field and the vorticity field respectively. The vector $\underline{k}$ is the wavevector for the gust component, and $\underline{Q}$ and $\underline{\Omega}$ are the amplitudes of the velocity field and the vorticity field for the gust component, respectively.

These two fields are related by the definition of the vorticity vector in terms of the velocity

$$\underline{\omega} = \nabla\times\underline{q} \tag{53}$$

If this relation is used together with the relation for incompressible flow

$$\nabla\cdot\underline{q} = 0 \tag{54}$$

the following relations can readily be derived:

$$\underline{\Omega} = i\underline{k}\times\underline{Q} \tag{55}$$

$$\underline{Q} = i\underline{k}\times\underline{\Omega}/k^2 \tag{56}$$

These two expressions are equivalent as can be seen by taking the cross product of either of them with $\underline{k}$; they express the relation beteen the Fourier components of velocity and vorticity.

Relations Between Upstream and Downstream Velocities. If we combine Equations 49, 55 and 56 we obtain the following relation between upstream and downstream velocities:

$$Q_i^U(\underline{k}^U) = -(k_j^U/k^{U^2})k_\ell^U\, Q_m^D(\underline{k}^D)\epsilon_{\ell mn}\frac{\partial x_k}{\partial \xi_n}\epsilon_{ijk} \tag{57}$$

This equation relates upstream and downstream Fourier velocity components if the relation between the upstream and downstream wavevectors $\underline{k}^U$ and $\underline{k}^D$ are known. This relation will be determined shortly. It should be noted that although the spatial coordinates of the upstream and downstream positions do not appear explicitly, they do appear implicitly through the deformation tensor. Thus, the decomposition of the velocity field into spatial Fourier velocity components is assumed to be a local decomposition.

Stated another way, a basic assumption of the analysis is that fluid planes in the upstream flow remain fluid planes in the downstream flow. The assumption arises when a one-to-one correspondence is made between an upstream and a downstream Fourier component of the turbulence. Each Fourier component assumes a sinusoidal distribution over all space, whereas the tensor is a function of position, and the flow is distorted by different amounts at different points.

This assumption will be grossly incorrect on a macroscopic scale. However, it becomes more and more accurate as restriction to smaller and smaller scales is made and should be accurate if the turbulence scale is small compared to the scale of the distorted flow.

Relation Between Upstream and Downstream Wavevectors. As with $\underline{Q}^U$ and $\underline{Q}^D$, the wavevectors upstream and downstream will be related by making use of the deformation tensor. The three vectors $\underline{\Omega}$, $\underline{Q}$ and $\underline{k}$ form an orthogonal system with $\underline{k}$ in the direction of $\underline{\Omega}\times\underline{Q}$. The systems will be orthogonal both upstream and downstream. The direction of $\underline{\Omega}^U$ can be found from $\underline{\Omega}^D$ using Equation 56. The same is not true about $\underline{Q}^U$ and $\underline{k}^U$, however.

In order to determine the directions of the two quantities $\underline{Q}^U$ and $\underline{k}^U$, use will be made of the assumption that planes of constant phase of a vorticity wave transform to similar types of planes in moving from upstream to downstream. Thus, if the vector $\underline{\Omega}$ in Equation 56 is replaced by $\underline{Q}$, the resulting vector (call it $\underline{A}$) on the left hand side will not be $\underline{Q}^U$, but it will be in the same plane as $\underline{Q}^U$ and $\underline{\Omega}^U$. Thus, the direction of $\underline{k}^U$ can be found by taking the cross product of $\underline{A}$ and $\underline{\Omega}$, which will be referred to as vector $\underline{B}$. By taking the cross product $\underline{B}$ with $\underline{\Omega}^U$, the direction of $\underline{k}^U$ can be found.

The above discussion outlines the method for finding the direction of $\underline{k}^U$. The magnitude is found by noting that if $\underline{\Omega}$ in Equation 56 is replaced by $\underline{k}$, the quantity on the left side (call it $\underline{C}$) will not be $\underline{k}^U$, but the parallel planes of vorticity through the endpoints of the vector $\underline{k}^U$. (See Fig. 23) Thus, the magnitude of $\underline{k}^U$ is found by taking the product of the magnitude of $\underline{C}$ with the cosine of the angle between $\underline{C}$ and the direction of $\underline{k}^U$ determined previously. The relation between the upstream and downstream wavenumbers is found to be

$$k^D/k^U = (e_3^U)_i (e_3^D)_j \frac{\partial x_i}{\partial \xi_j} \tag{58}$$

where $\underline{e}_3$ is a unit vector in the direction of the wavevector.

Comparison with Results of Ribner and Tucker

Ribner and Tucker perform the same analysis as above, but for the case where the deformation tensor is restricted to be digaonal, with the three diagonal terms given by $1/\ell_1$, $1/\ell_2$ and $1/\ell_3$. For this case the vectors $\underline{A}$ and $\underline{B}$ as defined above are found to be orthogonal to each other and to $\underline{\Omega}^U$, and so they represent vectors parallel to $\underline{Q}^U$ and $\underline{k}^U$ respectively. For the case of a diagonal deformation tensor the magnitude of $\underline{k}^U$ can be found by transformation of the quantity $\underline{e}_3/k$ since the wavelength of the gust is $2\pi/\lambda$ (see Fig. 24). Equation 58 is seen to be consistent with this. The equation for the transformation of the wavevector can be written

$$\underline{k}^D = \frac{k_1^U}{\ell_1}, \frac{k_2^U}{\ell_2}, \frac{k_3^U}{\ell_3} \tag{59}$$

agreeing with that of Ribner and Tucker. This verifies that the transformed wavevector described here reduces to that of Ribner and Tucker when the deformation tensor is diagonal.

To compare the velocity relation given by Equation 57 with that of Ribner and Tucker, Equation 57 is first written in the inverse form with $\underline{Q}^D$ on the left hand side. The deformation tensor is then replaced by a diagonal tensor and the substitution $\ell_1\ell_2\ell_3 = 1$ is made. Invoking the tensor relation

$$\varepsilon_{ijn}\varepsilon_{\ell mn} = \delta_{i\ell}\delta_{jm} - \delta_{im}\delta_{j\ell} \tag{60}$$

allows the final form to be written

$$Q_i^D = \frac{1}{\ell_{(i)}} \left[Q_i^U - \frac{k_j^U k_i^U}{\ell_{(j)}^2 k^{D2}} Q_j^U \right] \tag{61}$$

agreeing with that of Ribner and Tucker. In the above relation the brackets on the subscripts are to indicate there is to be no summation over the index inside the brackets unless it appears twice elsewhere in the relation; i.e., in Equation 61 the j index is summed over, but not the i index.

Numerical Results for the Vorticity Distribution at the Rotor Face

Using the above analysis, calculations have been carried out of the vorticity distribution occurring at the rotor face. These results are shown in Figures 25 through 30 which cover the six cases that we have examined. The calculations are based on having isotropic turbulence far upstream. (Although a nonisotropic representation could have been specified upstream, this has not been done in the present set of calculations due to the simple isotropic atmosphere turbulence model chosen.)

The figures show contours of different components of the vorticity at the rotor face. All values are normalized by the value of the upstream vorticity component, ω_x (or ω_y or ω_z since the upstream turbulence is isotropic).

Each figure has nine parts, a) to i). Part a) shows the normalized local streamwise component of vorticity, i.e., the component of vorticity along the local streamwise direction, computed using the numerical method described above. As stated this uses an integration along the streamlines to find the differences in drift of the particles on a given vortex line, or, equivalently, the degree to which vorticity that was initially normal to the streamlines has been tipped into the streamwise direction.

Part b) shows the streamwise component of vorticity calculated using what we will refer to here as the Ribner-Tucker approximation, namely that differences in drift time between different streamlines can be neglected. Within this approximation the normalized streamwise component of vorticity is just equal to the ratio of the local streamwise velocity to the far upstream velocity.

Part c) shows directly the differences between the two, i.e., if ω_S is the streamwise component, the contours shown are contours of the quantity,

$$\frac{\omega_S - \omega_{S,\text{Ribner-Tucker}}}{\omega_{S,\text{Ribner-Tucker}}}$$

in percent.

Parts d) and e) show the magnitude of the normalized vorticity vector in the plane normal to the local streamwise direction, i.e., the magnitude of the resultant of the normal and binormal components of vorticity. Part d) shows this for the calculation including differences in drift and Figure e) gives the results from calculations using Ribner-Tucker approximation referred to previously. Part f) again illustrates the difference between the two. If we denote the value of the vorticity in the plane normal to the streamlines by ω_{np} we have, in Figure f),

$$\frac{\omega_{NP} - \omega_{NP,\text{Ribner-Tucker}}}{\omega_{NP,\text{Ribner-Tucker}}}$$

Parts g), h), and i) present another view of the vorticity distribution. These show contours of the component of the (normalized) vorticity in the plane of the rotor. They can thus be regarded as giving qualitative

information applicable to the turbulence ingestion noise mechanism since it is this vorticity component, which induce velocity fluctuations normal to the rotor blades, that are the primary cause of the noise. Examination of these quantities thus provides a qualitative picture of those regions in which noise generation will be greatest.

Having described the format for each figure, specific observations can now be described to the six cases. Figure 25 shows the high speed forward flight case. As can be seen from the mean streamlines (Fig. 15), there is little change in mean velocity and little difference in drift from streamline to streamline. Thus there is little change in any of the vorticity components. There are, however, qualitative differences in the shapes of the contours. This will be seen to be even more pronounced in the other forward flight cases.

For the low speed forward flight situation (Fig. 26) larger differences occur between the streamwise components of vorticity computed in the two different manners--up to seventy-five percent in some parts of the disk. The differences in normal components are less, but are still appreciable.

As one might expect, even larger differences occur in the pseudo-hover situation shown in Figure 27. Here the differences in drift are larger, so there is more generation of streamwise vorticity. There is also more contraction so that there is potential for the streamwise vorticity to be amplified, and the contours of streamwise vorticity show this. The differences between the streamwise vorticity calculation which the non-uniform particle drift into account and that computed using the Ribner-Tucker approximation is approximately a factor of two over much of the area of the disk. Sizeable differences also occur for the vorticity component in the plane of the disk.

A similar trend is seen in the vertical ascent cases. The first of these, Figure 28, is for low speed vertical ascent. As might have been inferred from Figure 18, which showed the streamlines and timelines, there are appreciable differences between the two calculations (a) and (b) near the edge of the disk. The vorticity in the plane normal to the streamwise direction is almost the same for both calculations, presumably because the contraction on any given streamtube is close to axisymmetric.

There are also appreciable differences in the vorticity in the plane of the rotor disk calculated in the two ways, as seen in Figures 26 g) to i).

Figures 29 and 30 are for mid-speed and high-speed vertical ascent respectively. The same trends as in Figure 28 are seen here, although since the contraction ratio and the drift differences are less the effects are smaller.

To summarize the results of these calculations of vorticity for both the forward flight and vertical ascent cases, if there is a large contraction ratio it is necessary to include the differential drift (of fluid particles on different streamlines) to accurately calculate the vorticity at the rotor face.

THEORETICAL DEVELOPMENT OF ACOUSTIC ANALYSIS

The previous discussions have involved calculating the effect of a contraction and turning on the turbulence spectrum. The interaction of this turbulence with the individual rotor blades must now be considered in order to calculate the noise. The analysis and computer programming for the acoustic calculations are based on previous work which began with the study by Amiet (ref. 7) of an airfoil moving rectilinearly through a turbulent velocity field.

The noise of an airfoil moving rectilinearly through a turbulent velocity field can be calculated rigorously within certain limiting assumptions. In reference 7 the airfoil is modeled as a zero thickness flat plate. This restricts the analysis to eddies with a length scale large compared to the leading edge radius of the airfoil since the eddies are assumed to impinge on a sharp edge. This assumption could be eliminated if more general airfoil gust response functions (which included the effects of finite airfoil thickness) were used. Response functions that include the effect of thickness do exist (e.g. ref. 57), but they are significantly more complex than the flat plate response functions, and their calculation is numerical in nature in comparison to the response functions used here. A consequence of the flat plate airfoil assumption is that an upper limit is placed on the frequency that can be predicted by the analysis. If the leading edge radius is denoted by R_0 an eddy with this length scale would produce a frequency U/R_0. The acoustic spectrum of frequencies of this magnitude or higher would likely be overpredicted by the present theory since an eddy impinging on a sharp edge should produce a greater acoustic response than an eddy impinging on a rounded edge.

Another assumption used in the rectilinear airfoil-turbulence interaction analysis is that the span of the airfoil is significantly greater than the chord. Also, since the problem has been linearized the mean lift does not couple with the unsteady lift and the calculated sound is independent of the airfoil angle of attack. This linearization implies that the turbulence does not drift with the actual perturbed flow, but rather it drifts with the mean stream. Also, the turbulence is considered frozen and does not evolve with time.

Finally, the turbulent eddies are assumed small with respect to the airfoil span, s. This gives a lower frequency limit of the order U/s for the sound prediction. For the case of rectilinear motion this assumption could be relaxed, but it becomes an integral part of the problem when rotating airfoil are considered, as will be seen.

The above assumptions were found to be satisfactory in the experimental studies reported by Paterson and Amiet in reference 58. Excellent agreement between experiment and theory was found for frequencies below the value U/R_0 which is the limit due to the finite airfoil thickness.

The prediction method for the case of rectilinear airfoil motion is the foundation for the rotating airfoil (helicopter) prediction method. The basic idea is to use the spectrum predicted for the case of rectilinear motion as an instantaneous spectrum which will be averaged over time to arrive at the spectrum for the helicopter case. This method was introduced by Amiet in references 10 and 59 for the case of axial flow into a propeller and was generalized in reference 60 to the case of nonaxial inflow.

This technique of averaging an instantaneous spectrum to obtain an average spectrum may at first appear to be somewhat arbitrary, but it can in fact be shown to be rigorous within certain limitations, as described by Bendat and Piersal in reference 61. The basic limitation is that the time scale over which the instantaneous spectrum is changing is large compared to the relevant time scale (or inverse frequency) of the instantaneous spectrum. For the rotating airfoil this is equivalent to saying that the rotational frequency is low compared to the acoustic frequency of interest. This limitation is consistent with the above limitation for the case of rectilinear motion; i.e., that the acoustic frequency ω be greater than U/s. For rotational motion the velocity U can be set equal to the tip velocity Ωs so that $U/s = \Omega$ (the rotational frequency) and $\omega > \Omega$.

This limitation on the lowest frequency that can be calculated also appears in the expression of the sound produced by a rotating dipole. (Rotating dipoles are used to model the airfoil loading). The fundamental expression for the sound pressure produced by a rotating dipole was given by Equation (27) of Lowson (ref. 62). This equation, reproduced as Equation (1) of references 10 and 60, is

$$p_s = \left[\frac{1}{4\pi C_o r_s^2 (1-M_n)^2} \underline{\chi} \cdot \left(\dot{\underline{F}} + \frac{\underline{F}}{1-M_n} \dot{M}_n \right) \right] \tag{62}$$

The equation consists of two terms, the first due to the rectilinear motion and the second due to the acceleration of the dipole moving in a circular path. The first term is proportional to the time derivative of the loading (proportional to ω) and the second is proportional to the time derivative of M_n, the rotor Mach number in the direction of the observer (proportional to Ω). It is seen that the term due to the rectilinear motion will dominate if the rotational frequency is small compared to the acoustic frequency of interest (with the restriction that M_n not be near unity). Thus, for acoustic frequencies significantly higher than the rotational frequency of the rotor the dipole can be treated as if it were moving in rectilinear motion. The calculation made using this assumption has been compared in reference 10 to a

calculation of Homicz and George (ref. 9) which does not make the assumption. For the particular case for which the comparison was made, good agreement was obtained over the entire frequency range which would indicate that the assumption does not impose a significant restriction. (This is not a completely rigorous check on the assumption since there were other differences between the two theories, but it does provide evidence that the assumption is not restrictive.)

The present analysis extends the theory to the case of nonisotropic turbulence. The theory of references 10 and 60 is not limited to isotropic turbulence in principle. However, as a practical matter the assumption of isotropic turbulence was introduced to simplify the analysis. This assumption is removed from the present analysis so that the turbulence is allowed to be completely general. This assumption is used in Equation (14) of reference 10; without this simplifying assumption the programming becomes complicated since the turbulence must be calculated in a rotating coordinate system fixed to the rotor in order to be able to apply the theory of reference 7. If the turbulence is isotropic the expression for the turbulence is unchanged by a coordicoordinate rotation, but for nonisotropic turbulence a new function for the turbulence spectrum must be calculated for each angular position of the rotor. In addition, for isotropic turbulence an asymptotic high frequency expression for the summation in Equation (14) of reference 10 can be used, whereas for a general turbulence spectrum there is no such simplifying expression. This fact makes the computer program execution slower at the higher frequencies, whereas for the case of isotropic turbulence the program execution is faster at the higher frequencies since the asymptotic expression could be used for the summation. The method for the calculation of the nonisotropic turbulence spectrum used as input is summarized in the section Vorticity Field and Spectrum of Turbulence Undergoing a Rapid Distortion and the computer program used is given in reference 55.

The length scales of the turbulence are assumed to be small compared to the scale of the mean flow (the rotor scale). A turbulent eddy with a dimension comparable to the rotor diameter would lead to an acoustic frequency comparable to the rotor rotational frequency. The frequency has already been restricted to frequencies greater than this as indicated above. In general, the frequencies generated by eddies comparable in dimension to the rotor diameter will not produce sound in a range of interest; for an airfoil moving at Mach number M, the wavelength of the sound will be greater than the eddy dimension by a factor of M^{-1} so that large eddies will lead to low frequency sound, outside the range of interest. References 50 and 51 analyze the case of eddy scale comparable to the mean flow scale, but this case is not in the range of interest here.

Forward flight of the helicopter can have some interesting effects on the spectrum and on its calculation. For the forward flight case an eddy will move in the plane of the rotor during the time for blade passage. This leads

to the result that the noise need no longer be concentrated at blade passage frequency and its harmonics. On the advancing side of the rotor disk the rotor-eddy intersection frequencies will be higher than blade passage frequency and on the retreating side the intersection frequencies will be lower than blade passage frequency. The overall frequency will be an average of these. The frequency can also be affected by the turbulence being non-isotropic. Thus, if a stretched eddy is convected through the rotor, even if the mean flow is normal to the rotor disk the eddy chopping frequency can be different from blade passage frequency if the edge is tilted with respect to the flow vector.

This leads to some additional difficulty in the prediction of the noise. An average of the spectrum over the azimuthal rotor angle must be calculated. At the lower harmonics the instantaneous spectrum is strongly peaked about the eddy chopping frequency, and as noted above, this need not be the blade passage frequency. This is sketched in Figure 31. If a particular frequency is chosen at which to calculate the noise, then it is seen that certain azimuthal angles will contribute significantly to the noise, while at other angles the contribution is weak. The angular increment size in the azimuthal integration must be small in the vicinity of this dominant angle due to the strong directivity peaking. If this dominant angle is not calculated explicitly before the average is obtained, then significant extra calculations must be performed since the angular increment size in the integral must then be small around the entire azimuth.

ASSESSMENT OF ACOUSTIC RESULTS

Characteristics of Turbulence Ingestion Noise

The analytical model used to calculate the noise generated by a non-isotropic turbulence spectrum ingested by a rotor is an extension of that used previously for the case of isotropic turbulence (Refs. 10, 60). The mean flow contraction model and the turbulence distortion model are totally new flow field analyses which are needed to calculate the specific non-isotropic turbulence spectrum inputs to the acoustic analysis. It is worthwhile to consider first the general features of the resulting acoustic prediction and then to discuss the new elements of the extended acoustic model

For all atmospheric turbulence and rotor operating conditions, the acoustic calculations predict a narrow-band random spectrum at low frequency and a broad band spectrum at high frequency. These acoustic spectrum features are controlled at low frequency by the large eddies while at high frequency the spectrum is dominated by small eddies. The large eddies encounter multiple rotor blade interactions leading to significant blade to blade correlation and the production of sound concentrated around the harmonics of blade passage frequency. The small eddies are cut by one blade, and there is no possibility of blade to blade correlation.

It should be noted that blade-to-blade correlation by itself does not lead to an increase of acoustic energy, as pointed out in Reference 59. (The increased velocities from a stretched eddy can lead to changes in acoustic energy as discussed in the following section on Nonisotropic Effects). Equation 17 in Reference 59 shows that for the case of isotropic turbulence the ratio of the tone peak amplitude to the tone energy is proportional to the turbulent length scale and inversely proportional to the axial mean flow velocity. Thus, decreasing the drift time through the rotor by decreasing the axial velocity will lead to an increase in tone amplitude with no change in energy.

Blade-to-blade correlation may at first appear to increase the acoustic energy since the tones have a significantly higher dB level than the surrounding broadband noise. However, the highest tones also tend to be the narrowest, and the acoustic energy will be significantly lower than might be inferred from the tone level. This factor becomes more important when the case of nonisotropic turbulence is considered; then the eddies can be stretched so that they are chopped by many blades leading to even narrower tones with even higher peak amplitudes.

The reason that blade-to-blade correlation does not lead to an increase of acoustic energy can be demonstrated with an example. Consider the case of a single rotor blade cutting turbulence of small length scale that is drifting through the rotor plane. This generates a broadband acoustic signal $p^2(t)$ propagating to the observer. The time integral of this signal gives the acoustic energy. Now let the rotor pass through the same turbulence field, but consider the turbulence drift velocity to be zero at the rotor plane; that is, the rotor will cut the same eddies repeatedly. This results in pure tones at the blade passage harmonics. However, the integral of $p^2(t)$ will be the same if the turbulent field is stationary in the statistical sense. (This conclusion would be modified slightly if the eddy were large (of the order of the rotor diameter) so that two blades could cut the same eddy at the same time since then the acoustic pressures would be added before calculating $\overline{p^2(t)}$ but these large eddies are inefficient in generating noise.)

Selection of Test Conditions

In order to compare acoustic results for similar test conditions, the aerodynamic results from the previous "Vorticity Field and Spectrum of Turbulence Undergoing a Rapid Distortion" chapter were used as input to the acoustic prediction procedure. In this way the various effects of helicopter operating conditions and atmospheric properties could be compared. The hover case was chosen for detailed examination since it presents some of the largest effects and is still an important, practical helicopter operating condition. Unless otherwise stated, the atmospheric conditions used were neutral stability, a geostrophic wind speed of 5.1 m/s, and an altitude of 122 m.

Figure 32 shows the coordinate system used for the acoustic procedure. The x, y, z axis is fixed to the rotor hub with z being the rotor axis. The axial component of flow into the rotor is in the negative z direction. The observer is assumed to be in the x-z plane at a distance r from the hub and at a polar angle θ with the z axis. The non-axial component of flow, M_f, is at an azimuthal angle Φ to the y axis, pointing inward toward the origin as shown. Unless otherwise noted, the observer location used for all the cases was at a polar angle of 0 degrees and an azimuthal angle of 0, i.e. directly above the rotor, at a distance of 10 radii.

Forward Flight Effects

Acoustic spectrum predictions will now be presented for the forward flight test condition. However, before preceding it is necessary to describe the general characteristics of the narrowband acoustic spectrum generated by rotor turbulence ingestion during forward flight.

For the case of hover or vertical ascent narrow band random acoustic tones occur at harmonics of blade passage frequency. With forward flight, however, there is a velocity component in the rotor plane. This changes the time interval for the cutting of an eddy since the eddy moves in the rotor plane. The time interval is decreased on the advancing side and increased on the retreating side of the rotor disk. Since the measured noise spectrum is an average around the rotor disk, the narrow-band random tones in the measured spectrum can be either higher or lower in frequency than the harmonics of blade passage frequency. Whether the peak levels of the tones of this averaged spectrum occur at frequencies that are higher or lower than blade passage frequency depends on the directivity and amplitude of the noise as the rotor moves around the rotor plane. For an observer directly below the rotor, one would expect the tones to increase in frequency with flight since the directivities of the sound produced by the rotor would be expected to be greater for the advancing side than for the retreating side of the rotor because of its greater relative Mach number.

A more noticeable effect due to forward flight is the broadening and decrease in peak level of the tones. This, again, is due to the movement of the eddies in the rotor plane between eddy intersections. Because the eddy intersection varies over the rotor disk, one would expect the resulting acoustic spectrum to be broader than if the eddy drift velocity in the rotor plane were zero. This phenomenon is evident in Figure 33. Based on the arguments presented above, the acoustic energy is essentially unchanged by forward flight until the flight Mach number becomes comparable to the rotor tip Mach number. Then, because acoustic energy generation depends on the fifth or sixth power of the relative Mach number, the additional acoustic energy generated on the advancing side of the rotor will be greater than the decrease in energy on the retreating side.

The shifting of the intersection frequency as one moves around the rotor disk for the forward flight case creates difficulties in the application of the computer program. As discussed in the theory section of the report, a much larger number of azimuthal integration points must be used for the forward flight case. This point was not addressed in Reference 60 for the forward flight cases presented there. The curves shown in Reference 60 are much more jagged at low frequency than they should be. The computer code used for those results is basically the same as that used here (without the extension to nonisotropic turbulence) but an insufficient number of azimuthal integration points was used. The present calculations use a much larger number of azimuthal integration points. This produces much smoother curves at the expense of requiring significantly greater computing time.

Effect of Helicopter Operating Condition

Figure 33 shows the spectra for both the isotropic and nonisotropic turbulence for five different flight conditions: fast speed forward flight, slow speed forward flight, pseudo hover, slow vertical ascent, and high vertical ascent. The first 1000 harmonics are presented for each condition. The integrated sound power level (SPL) or intensity for each case is also indicated on each figure. The upper set of curves are for nonisotropic turbulence and the lower curves show the isotropic inflow cases based on no contraction at the rotor face (calculated using the turbulence contraction model developed in the present study).

The highest sound power level SPL = 54.5 dB, occurs for the low speed vertical ascent case. The lowest SPL, 50.8 dB, occurs for the high speed forward flight case. The discrete tone peaks in the spectra are sharp and pointed and the amplitude of the signal is largest for the low speed vertical ascent and the pseudo hover cases. For slow speed forward flight conditions, the peaks become rounded and the amplitude differences between the peaks and the valleys becomes smaller. There is a corresponding decrease in SPL with increasing flight speed. These general observations in the predicted spectrum dependence on flight conditions hold for both isotropic and nonisotropic turbulence spectrum.

Nonisotropic Effects

For the case of nonisotropic turbulence, the eddies are stretched in the direction of the rotor axis. This increases significantly the number of rotor blade-eddy intersections as the turbulent eddy convects through the rotor. This in turn increases the acoustic amplitudes of the narrow band random tones while decreasing their width. The effects of this eddy stretching can be considered in two parts: an increase in blade-to-blade correlation and changes in the turbulent velocities.

For illustrative purposes, these two effects will first be considered separately. Assume that the eddies are stretched in the axial direction, but retain the spectral characteristics in the rotor plane. Then any single rotor pass will produce a spectrum that is the same as that for a non-stretched eddy since the transverse velocity spectrum which controls turbulence ingestion noise remains the same. Because the eddies are stretched in the axial direction, blade-to-blade correlation is increased, and the narrow-band tone will be higher and narrower. But as discussed above, there will be no increase in acoustic energy. This method of simulating a nonisotropic spectrum input was used in Reference 13 by decreasing the axial Mach number in the computer program. Because the axial Mach number is generally significantly smaller than the rotor tip Mach number, this will have little effect on the

acoustic energy produced. It serves merely as a method for simulating increased blade-to-blade correlation.

The second effect of nonisotropic turbulence can affect the acoustic energy. In addition to being stretched in physical dimensions along the axis, the turbulence spectrum is also changed in the cross directions. This is the effect produced by stretching a vortex (with vorticity distributed throughout its core) along its axis. As it is stretched the vorticity is drawn in toward the axis and the velocities induced by the vortex are increased. For eddies in the cross direction to the stretching, the stretching will have the opposite effect. Thus, the stretching of the turbulence will increase the velocities of some eddies and decrease the velocities of others.

Whereas the above method of simulating nonisotropic turbulence ingestion by decreasing the axial Mach number could not predict any increase in acoustic energy, the present calculations can account for such an energy increase. The overall effect on the noise is difficult to predict without running the computer code since it depends on the particular orientation of the rotor blades. This orientation in turn is changing as the blade moves around the azimuth and an average is calculated. For the cases shown in Figure 33 the effect is generally to increase the noise somewhat. It is difficult to determine this effect by visual inspection of the harmonic peaks since it is masked by the first effect, the increased blade-to-blade correlation. However, it is evident from the broad band portion of the curves which are generally a few dB higher than the comparable isotropic cases.

As indicated in Figure 33, the largest difference in SPL between the isotropic and nonisotropic conditions, 4.21 dB, occurs for the low speed vertical ascent condition. The spectrum changes from low amplitude, smooth peaks for the isotropic case to high amplitude, sharp peaks for the nonisotropic case. For the isotropic case, the harmonics are weak at the 25th harmonic location, whereas they continue to be strong at the 25th harmonic location for the nonisotropic case.

The difference in SPL between isotropic and nonisotropic turbulence cases decreases with increasing forward flight speed. For the high speed forward flight condition, the two spectra are nearly identical. This latter result can be explained by the aerodynamic streamline predictions presented earlier. For the fast forward flight case, very little turning or contraction of the streamlines occurs (see Figure 15) with the flow convecting through the rotor unaltered. Therefore, there is little difference between the isotropic and the nonisotropic cases.

For the hover case, however, the aerodynamic results show both large turning and contraction (see Figure 17). In this case the turbulence field is

significantly distorted by the mean flow. The need to include the contraction effects in the turbulence model is indicated by the comparison between the isotropic and non-isotropic spectra in Figures 33e and 33f.

Although the turning is not as severe for the low speed vertical ascent case (Figure 18), the contraction is still quite high. This accounts for the large difference noted in the acoustic spectra.

Turbulence - Blade Interaction Location

Since the acoustic prediction model developed in the present study assumes a homogeneous turbulence field at the rotor, only a single deformation tensor from the aerodynamic predictions is needed. In this case, the deformation tensor located at the center of the rotor was used to predict noise produced over the entire rotor. However, the turbulence predictions showed a large variation in properties over the rotor disk, indicating that the turbulence is non-homogeneous. Although the present acoustic analysis treats only the homogeneous turbulence field, an understanding of the non-homogeneous effects can be obtained by considering deformation tensors from different segments of the rotor.

To show the effect of the location of the deformation tensor on the spectra, six different tensor locations were selected on the rotor face for the pseudo hover condition. The results are shown in Figure 34. The center plot shows contours of constant vorticity in the plane of the rotor taken from Figure 27g. Three positions were chosen at 95% of the distance out to the rotor tip, at azimuthal angles of 0, 90 and 180 degrees. Two locations were chosen at the mid span of the blade at azimuthal angles of 45 and 135 degrees. The spectra produced by a deformation tensor at the center of the hub is also shown for reference.

The acoustic spectra in Figure 34 show large differences in character with location. The SPL varies from a minimum of 50.0 dB to a maximum of 53.9 dB. The spectra vary from nearly smooth curves dominated by broadband noise to curves dominated by intense discrete tones. This figure shows that in order to get a more accurate prediction of the turbulence ingestion noise it is necessary to remove the restriction of homogeneity from the acoustic prediction.

Rotor Acoustic Directivity Pattern

Polar Directivity. The effect of polar directivity of the turbulence ingestion noise for two cases is shown in Figure 35. This plot shows the PSD for the third harmonic as a function of polar angle, θ, for hover and fast forward flight. The observer azimuthal angle is held fixed at $\phi = 0°$ for these calculations. Although these figures are limited to hover and fast forward flight, polar directivity plots of other operating conditions were observed to be similar and will, therefore, not be presented.

The tone directivity pattern is seen to be flat within ±.2 dB over ±45 degrees of the rotor axis. Beyond 45 degrees from the axis, the directivity pattern decreases sharply as the plane of the rotor is approached. The minimum for the hover case is at 88.85 degrees and not at 90 degrees as one might first suspect. The reason that the minimum does not occur at 90 degrees is that the dipoles used to represent the noise are oriented normal to the flat plate airfoils, but since the rotor blades are at angle of attack, the rotor surface does not lie in the rotor plane.

The polar directivity of both isotropic and nonisotropic cases are predominantly dipole like in character. For the case of isotropic turbulence (as shown in Ref. 59), the directivity gets pushed outward from the rotor axis, changing from a cosine or spherical pattern above the plane to a more oblate shape, and a corresponding pattern below the rotor plane. This also occurs for the nonisotropic cases shown in Figure 35. The reason for the oblateness of the directivity pattern is that at high Mach number sound is beamed forward along the line of motion. This effect can result in several dB increase at a Mach number of 0.5.

Azimuthal Directivity. Figure 36 shows a plot of the azimuthal directivity patterns for the hover and the forward flight cases. The polar angle was fixed at 45 degrees for these calculations. The third harmonic was again used as a representative indicator of directivity.

The peak in the tone directivity pattern occurs at 0 degrees, i.e. for an observer in the direction of forward flight. In contrast the minimum tone amplitude occurs for an observer at approximately 200 degrees. The range of the directivity from maximum to minimum is only about 6 dB for this case, which is considerably less than the polar directivity variation.

The results were similar for the other operating conditions with the exception of the vertical ascent cases. For these cases, the flow is axisymmetric and the present analysis predicts a uniform azimuthal directivity for both isotropic and nonisotropic turbulence.

Effect of Altitude

By flying at different heights in the atmosphere, a helicopter experiences different turbulence fields. The effect of altitude on atmospheric turbulence ingestion noise is shown in Figure 37. This plot shows the acoustic spectra for the nonisotropic turbulence, pseudo hover condition for three different altitudes, 50 m, 122 m, and 152 m. The highest SPL occurs for the lowest altitude. Although the integral length scales will be smaller at lower altitudes, the turbulence intensities are higher. This increased intensity may be responsible for the increased noise observed at lower altitude.

Effect of Wind Speed

The effect of wind speed on atmospheric turbulence ingestion noise was examined by considering three different wind speeds. All other atmospheric parameters were held constant at 122 m height and neutral stability. Figure 38 shows that higher wind speeds cause larger turbulence ingestion noise, although the effect is not as pronounced as that due to altitude.

Effect of Atmospheric Stability Length

The effect of atmospheric stability length on the turbulence ingestion noise is shown in Figure 39. The atmospheric parameters for this case are a 10 knot wind speed and a height of 122 m. A stable atmosphere (i.e. one with a positive stability length) results in lower turbulence ingestion noise levels than a neutral atmosphere. The difference is approximately 5 dB in SPL between these two conditions. The unstable atmosphere (a negative stability length) produces considerably more turbulence ingestion noise than does the neutral atmosphere, 20 dB in SPL for this case. From Table 1 we can see that the integral length scales are the same for the neutral and the unstable cases (due to the atmospheric turbulence model used). The turbulence intensity, however, is much larger for the unstable case which is the reason for the significant increase in noise.

Full Scale Prediction

The preceding predictions have all been done using model scale rotor data. The operating conditions were taken from reference 33. In order to ascertain how the program would work with a full scale helicopter, two different cases were run.

To assist an ongoing NASA Langley experimental program on turbulence ingestion noise in hover, calculations were also performed for a full size, Hughes 500 E helicopter. Results shown in Figure 40 are for two different rotor thrust conditions which are exemplified by different induced rotor velocities, V_o. The rotor diameter for these calculations is 8 m. The observer location is above the rotor disk at θ = 30 degrees and an azimuthal angle of Φ = 3 degrees. Rotor height is one rotor diameter above the ground (This condition corresponds to an outdoor hover test to be conducted jointly by NASA and McDonnell Douglas Helicopters). Both cases shown in Figure 40 are for a wind speed of 2.57 m/s (5 Knots) at the height of the rotor which represents the maximum allowable speed for this test.

Figures 40a and 40c show the spectra and the streamlines for the 5 knot wind case and the maximum lift condition. Figures 40b and 40d show the spectra and streamlines for the same wind at a partial lift condition. The partial lift condition has narrower peaks and a 2.6 dB higher SPL than the maximum lift condition. The partial lift condition continues to show strong blade passage harmonics up through the 100th harmonic. This is contrasted by the maximum lift condition in which the blade passage harmonics begin to decay by the 50th harmonic.

Comparison of Present Turbulence Contraction Model to Ribner-Tucker Approach

To predict the turbulence ingestion noise from a helicopter rotor, a statistical description of the turbulence incident on the rotor is required. Different approximations of the turbulence properties can be employed. The simplest approach is to assume that the turbulence at the rotor is isotropic and is the same as the turbulence in the free atmosphere (i.e. without any influence of the rotor flow field).

A more advanced approximation is to use the Ribner-Tucker turbulence contraction model which does not require tracing streamlines. This approach calculates the nonisotropic turbulence field at the rotor by using the mean velocity field far upstream and at the rotor disk. The streamwise vorticity vector at the rotor disk is determined from the magnitude of the streamwise velocity. The magnitudes of the two normal vorticity vectors are found from the inverse square root of the magnitude of the streamwise velocity. The streamwise direction is considered known and it is assumed that one of the normal vorticity vectors is in the plane of the rotor. The other normal vorticity vector is assumed to be mutually orthogonal to the first normal vorticity vector and the streamwise vorticity vector. The nine components of the deformation tensor are determined by resolving the streamwise and normal vorticity vectors into orthogonal coordinates.

The highest level approximation for the turbulence contraction process tracks the streamlines to calculate the deformation tensor. This requires considerably more computation, but includes both the effect of vortex stretching and vortex filament turning which is not included in the Ribner-Tucker approach.

Figure 41 shows the acoustic spectrum for the model scale hover case calculated using the three above described turbulence approximations. Spectrum are shown from top to bottom with increasing levels of sophistication in the turbulence contraction model. The SPL increases from 50.23 dB for the simple isotropic assumption to 50.37 dB for the Ribner-Tucker approximation and 52.71 for the full nonisotropic turbulence prediction procedure. Spectra for the isotropic and the Ribner-Tucker approaches are broader than the nonisotropic spectrum case which is sharp and peaked. Spectral peaks for the isotropic and the Ribner-Tucker cases exhibit approximately the same amplitude, although the minima are deeper for the isotropic case. The amplitude of the first harmonic is about the same for all three plots, but the second and subsequent harmonics are approximately 7 dB higher for the nonisotropic case than the other two.

The importance of including the full theory incorporating both vortex stretching and turning to calculate the nonisotropic turbulence at the rotor disk is apparent.

Comparison to Trailing Edge Noise

Turbulence ingestion noise is only one of several noise mechanisms which are responsible for the total noise produced by a helicopter rotor system. The relative importance of turbulence ingestion noise can be accessed by comparing it to other noise mechanisms. A comparison to the trailing edge noise is shown in Figure 42. A trailing edge scaling law from Schlinker and Amiet (ref. 63) is shown plotted along with the turbulence ingestion noise for the pseudo hover case.

It is apparent that turbulence ingestion noise is the dominant mechanism for low frequencies. It is not until the 30th harmonic that trailing edge noise begins to dominate. The peak in the trailing edge spectrum occurs at approximately 100 blade harmonics for this case. Beyond 30 harmonics the turbulence ingestion noise decays at a nearly constant rate of 3.5 dB per octave. The slope of the trailing edge noise prediction is nearly the same as the turbulence ingestion noise prediction at high frequencies. The turbulence ingestion noise is more than 25 dB below the trailing edge noise for frequencies above 100 harmonics. It is therefore concluded that turbulence ingestion noise can be an important noise source for helicopters.

CONCLUSIONS

An analytical procedure has been developed to predict helicopter rotor noise generation due to the ingestion of atmospheric turbulence. The analysis combines several different models which describe the fluid mechanics of the turbulence ingestion process and the resulting noise. Specific phenomena modeled include the atmospheric turbulence, the rotor mean inflow, distortion of the atmospheric turbulence during the inflow process, the unsteady rotor blade lift response to the turbulence, and finally the noise generation. The noise generation model is based on an analysis and computer code previously developed by Amiet for the case of isotropic turbulence in the rotor plane.

A computer code was developed to implement the analytical models for cases of practical interest. Flow field and acoustic calculations were obtained for five cases: fast forward flight, slow forward flight, pseudo hover, low speed vertical ascent, and high speed vertical ascent.

A. Fluid Dynamic Conclusions

A.1) Mean flow and turbulence statistics associated with the atmospheric boundary layer can be modeled by existing analyses. The effects of atmospheric stability length, wind speed, and altitude on the turbulence intensity, length scale and spectrum can be predicted.

A.2) For the atmospheric conditions encountered by a helicopter main rotor, statistical properties of the upstream turbulence can be modeled as locally stationary and homogeneous. In addition, for the wavenumbers controlling the generation of atmospheric turbulence ingestion noise, the turbulence field is locally isotropic. The relevant wavenumber range controlling the noise generation is bounded by the rotor diameter at low wavenumbers and the blade thickness at high wavenumbers.

A.3) Contraction and turning of streamlines by the rotor mean inflow distorts the upstream atmospheric turbulence field. The initially isotropic atmospheric turbulence is distorted to a non-isotropic velocity field at the rotor disk.

A.4) The turbulence distortion process can be modeled as a deformation of vorticity filaments which represent the turbulence field. Deformation of the filaments can be computed using a rapid distortion theory. Turbulence intensity, turbulent eddy distortion time, and inviscid criteria for application of the rapid distortion theory are satisfied for helicopter main rotor inflow conditions.

A.5) For large mean flow contraction ratios, accurate predictions of turbulence vorticity components at the rotor face requires incorporating the differential drift of fluid particles on adjacent streamlines. Failure to account for this effect results in discrepancies of 200% in the streamwise component of the vorticity and pronounced differences in the predicted non-isotropic and non-homogeneous turbulence field at the rotor face.

A.6) Significant mean-flow contraction and turning of vortex filaments (or streamlines) occurs for hover, low speed vertical ascent, and low speed forward flight. The resulting distortion creates a non-homogeneous anisotropic turbulence field at the rotor disk. Turbulence vorticity strength differs from the upstream isotropic turbulence conditions by factors of 0.5 to 20 over the rotor face.

A.7) Mean flow contraction and turning are absent for high speed vertical ascent and high speed foward flight. Turbulence distortion is consequently non-existent and turbulence spectra at the rotor face are isotropic for these operating conditions.

B. Aeroacoustic Conclusions

B.1) A first principles theory for the rotor turbulence ingestion noise demonstrated pronounced differences between quasi-tonal peak amplitudes for isotropic atmospheric turbulence and non-isotropic turbulence at the rotor face. The largest difference occurs for hover and low speed vertical ascent where turning and contraction of the flow, result in approximately a 3 dB increase in the acoustic spectrum energy. In addition, quasi-tonal peaks at multiples of blade passage frequency become more pronounced with peak amplitudes increasing by 10 dB and high frequency broadband noise increasing by approximately 5 dB. Negligible differences exist between isotropic and non-isotropic turbulent inflows for high speed vertical ascent and forward flight operating conditions.

B.2) Predicted acoustic spectra are sensitive to the non-homogeneous turbulence vorticity distribution over the rotor face. Non-homogeneous distributions are presently not modeled in the acoustic analysis and qualitative assessment of the sensitivity requires selecting vorticity deformation tensors from various segments of the rotor plane. Differences of 4 dB in acoustic energy and 10 dB in quasi-tonal peak amplitude exist due to differences in vorticity distortions between various streamtubes over the rotor disk.

B.3) Accurate predictions of turbulence ingestion noise requires modeling the differential drift of fluid particles on adjacent streamlines. Failure to account for this effect results in pronounced differences in the quasi-tonal peak amplitudes and tone width.

B.4) Polar directivity patterns exhibit dipole characteristics for both isotropic and non-isotropic incident turbulence with minimum sound pressure level occurring in the plane of the rotor. Azimuthal directivity patterns vary strongly with helicopter flight condition. Vertical ascent operating conditions exhibit an azimuthally uniform directivity pattern for both isotropic and anisotropic turbulence.

B.5) Detailed statistics of the atmospheric turbulence field are critical for accurate predictions of turbulence ingestion noise. Stability length is the most sensitive parameter as indicated by a 20 dB increase in acoustic energy between stable and unstable atmospheric conditions. Decreases in altitude and increases in wind speed also enhance the turbulence ingestion noise. Changes in stability length, altitude, and wind speed have the strongest impact for hover and takeoff (vertical ascent) operating conditions.

B.6) Differences of 3 dB in acoustic energy occur between various helicopter operating conditions. The most intense turbulence ingestion noise condition is the low speed vertical ascent case, and the quietest condition is the fast forward flight case. Increasing forward flight speed tended to decrease quasi-tonal peak amplitudes in addition to broadening the peaks.

B.7) Compared to trailing edge noise, turbulence ingestion noise is the dominant noise mechanism below approximately 30 rotor harmonics. Above 100 harmonics, trailing edge noise levels exceed turbulence ingestion noise by 25 dB.

APPENDIX

THE SPECTRUM OF TURBULENCE UNDERGOING A RAPID DISTORTION

The purpose of the following analysis is to relate the upstream vector values for wavevector and fluid velocity to the corresponding downstream values. The analysis begins by deriving the relations between vorticity and velocity for a particular wavevector component. These equations do not relate upstream and downstream quantities, but only the quantities at a point; these results are derived from the assumed sinusoidal variation for the velocity field of a wavevector component.

In the second section the equations for the transport of vorticity are used to derive a relation between the upstream and downstream velocity vectors of a wavevector component. In the third section the same transport equations are used to derive a relation between the upstream and downstream wavevectors.

Finally, in the last section the present results are compared to the results of Ribner and Tucker. Agreement is found for both the wavevector and the fluid velocity transformation.

Relations Between Velocity and Vorticity

In calculating the noise generated by a rotor moving through a turbulent field, a required input is the turbulence spectrum as a function of the wavevector

$$\underline{k} = \underline{i}\, k_x + \underline{j}\, k_y + \underline{k}\, k_z \tag{A.1}$$

The velocity field $\underline{q}$ of a single wavevector Fourier component can be written

$$\underline{q}^D(\underline{k}^D, \underline{x}) = \underline{Q}^D(\underline{k}^D)\, e^{i\underline{k}^D \cdot \underline{x}} \tag{A.2}$$

where the D superscript refers to the downstream post-contraction location, at the rotor face. The U superscript will refer to the upstream pre-contraction velocity field. The object of this analysis is to relate the two velocity fields. In Equation A.2 $\underline{Q}$ and $\underline{k}$ are orthogonal from the assumption of incompressible flow (see Fig. 23). Thus, $\underline{Q}$ can be written as the cross product of $\underline{k}$ with some vector $\underline{P}$; i.e.,

$$\underline{Q}(\underline{k}) = \underline{k} \times \underline{P}\ (\underline{k}) \tag{A.3}$$

The superscripts U and D are not used here since the equation can be applied to either region.

The vorticity field $\underline{\omega}$ of the wavevector Fourier component is given by

$$\underline{\omega} = \nabla \times \underline{q} \tag{A.4}$$

so that from Equations A.2 and A.3

$$\underline{\omega}\ (\underline{k}, \underline{x}) = i\underline{k} \times Q(\underline{k})\, e^{i\,\underline{k}\cdot\underline{x}} = i\left[\underline{k}(\underline{k}\cdot\underline{P}) - \underline{P}\ k^2\right] e^{i\,\underline{k}\cdot\underline{x}} \tag{A.5}$$

From Equation A.5 it will be noted that

$$\underline{k}\cdot\underline{\omega} = 0 \tag{A.6}$$

Writing

$$\underline{\omega}(\underline{k}, \underline{x}) = \underline{\Omega}(\underline{k})\, e^{i\,\underline{k}\cdot\underline{x}} \tag{A.7}$$

we wish to solve for $\underline{Q}$ in terms of $\underline{\Omega}$. Then knowing how $\underline{\Omega}$ transforms between upstream and downstream locations, the behavior of the velocity field will be known. From Equations A.5 and A.7

$$\underline{\Omega}(\underline{k}) = i\left[\underline{k}(\underline{k}\cdot\underline{P}) - \underline{P}\,k^2\right] \tag{A.8}$$

On taking the cross product of this equation with $\underline{k}$, the first term on the right hand side drops out leaving

$$\underline{k} \times \underline{\Omega} = -ik^2\,\underline{k} \times \underline{P} = -ik^2\,\underline{Q} \tag{A.9}$$

This then leaves us with two equivalent expressions for relating vorticity and velocity of a Fourier component

$$\underline{\Omega} = i\,\underline{k} \times \underline{Q} \tag{A.10a}$$

$$\underline{Q} = i\,\underline{k} \times \underline{\Omega}/k^2 \tag{A.10b}$$

Relating Upstream and Downstream Velocities

We now consider the relation between upstream and downstream properties. The vorticity of a fluid particle is related by the deformation tensor. Thus, using an expression attributed to Cauchy (Ref. 56, p. 205)

$$\Omega_i{}^D = \Omega_j{}^U \frac{\partial \xi_i}{\partial x_j} \tag{A.11a}$$

$$\Omega_i{}^U = \Omega_j{}^D \frac{\partial x_i}{\partial \xi_j} \tag{A.11b}$$

where x_i represents the upstream coordinate system and ξ_i the downstream coordinate system. Both coordinate systems are assumed right handed and orthogonal. The coordinates of a fluid particle also transform according to Equation A.11. For example, consider a cube of fluid downstream with edges parallel to the axes. The edges can then be written $(\ell,0,0)$, $(0,\ell,0)$, $(0,0,\ell)$ where ℓ is the length of the side of the cube. By writing each of these vectors as a row vector, the three together form a 3x3 matrix

$$C^D = \ell\, I \tag{A.12}$$

where I is the unity matrix. The three upstream transformed vectors denoting the cube are then given by

$$C^U = C^D \left[\frac{\partial x_i}{\partial \xi_j}\right] = \ell \left[\frac{\partial x_i}{\partial \xi_j}\right] \tag{A.13}$$

where $\left[\frac{\partial x_i}{\partial \xi_j}\right]$ denotes the deformation tensor

$$\frac{\partial x_i}{\partial \xi_j} = \begin{bmatrix} \frac{\partial x_1}{\partial \xi_1} & \frac{\partial x_1}{\partial \xi_2} \cdots \\ \frac{\partial x_2}{\partial \xi_1} & \vdots \\ \frac{\partial x_3}{\partial \xi_1} & \vdots \end{bmatrix} \tag{A.14}$$

The volume of the cube upstream is then given by the cross product of two of the vectors with the dot product of the third, which is the same as the value of the determinant of the matrix. For incompressible flow this must be ℓ^3, the same as downstream. This requires that the determinant of the deformation matrix in Equation A.14 be 1.

The following paragraphs will give the detailed procedure for transforming between the upstream (pre-contraction) and downstream (post-contraction) velocity fields. One basic assumption of the analysis to follow is that fluid planes in one coordinate system remain fluid planes in the other; that is, planes before distortion remain planes after distortion. This assumption will be grossly incorrect, in general, on a macroscopic scale. However, it becomes more and more accurate as restriction to smaller and smaller scales is made. The assumption should thus be adequate if the turbulence scale is small compared to the scale of the distorted flow. The assumption arises when a one-to-one correspondence is made between an upstream and a downstream Fourier component of the turbulence. Each Fourier component consists of a vorticity distribution over all space, whereas the deformation tensor applies only on a local basis; that is, the deformation tensor is a function of position, and the flow is distorted by different amounts at different points.

The relation between upstream and downstream wavevectors has yet to be determined. For the present they will be denoted by $\underline{k}^U$ and $\underline{k}^D$ with the assumption that the two wavevectors are related by the deformation tensor in some manner to be determined later. Equations A.10 and A.11 can then be combined to obtain a relation between the upstream and downstream velocity field. Equation A.11 relate upstream and downstream vorticity levels while Equations A.10 relate velocity to vorticity at either the upstream or downstream location.

Combining Equations A.10b and A.11b gives

$$Q_i^u(\underline{k}^u) = i\,(k_j^u/k^{u2})\,\Omega_n^D(\underline{k}^D)\,\frac{\partial x_k}{\partial \xi_n}\,\epsilon_{ijk} \tag{A.15}$$

where Cartesian tensor notation is used. Summation over repeated indices is assumed, and ϵ_{ijk} is the alternating tensor. Using Equation A.10a to substitute for Ω_n^D gives

$$Q_i^U(\underline{k}^U) = -(k_j^U / k^{U^2})\, k_\ell^U \; Q_m^D(\underline{k}^D)\, \epsilon_{\ell mn} \frac{\partial x_k}{\partial \xi_n} \epsilon_{ijk} \qquad \text{(A.16)}$$

This equation relates the upstream and downstream velocities if the relation between the upstream and downstream wavevectors $\underline{k}^U$ and $\underline{k}^D$ is known; this relation will be determined shortly. It should be noted that although the spatial coordinates of the upstream and downstream locations do not appear explicitly, they do appear implicitly through the deformation tensor. Thus, even though the velocity field has been decomposed into spatial Fourier components, this is in some sense a local decomposition.

In applying Equation A.16, in addition to specifying the deformation tensor and the wavevector of interest, the velocity $\underline{Q}^D$ must be specified. The amplitude of $\underline{Q}^D$ is not of concern since the ratio of amplitudes is all that is needed. The direction of $\underline{Q}^D$must be specified, however. Once k^D is specified, Q^Dcan lie anywhere in the plane normal to $\underline{k}^D$ since $\underline{k}^D$ and $\underline{Q}^D$ are normal for the velocity modes considered. For the specific case of an airfoil moving through the turbulence let us consider a plane formed by the vector $\underline{k}^D$ and a unit vector $\underline{n}$ normal to the airfoil surface. Then for the specific $\underline{k}^D$ vector chosen, the velocity field can be decomposed into a component in the plane formed by the vectors $\underline{k}^D$ and $\underline{n}$ and a component normal to this plane. In calculating the airfoil response to turbulence using a linearized analysis, only the velocity component along $\underline{n}$ will give a contribution. Thus, any component of $\underline{Q}^D$ normal to the $\underline{k}^D$, $\underline{n}$ plane can be neglected. This allows $\underline{Q}^D$ to be specified as normal to $\underline{k}^y$ and in the $\underline{k}^D$, $\underline{n}$ plane.

Relating Upstream and Downstream Wavevectors

The only remaining relation to be determined in Equation A.16 is that between $\underline{k}^U$ and $\underline{k}^D$; i.e., how the wavevectors of the mode considered becomes distorted in going from upstream to downstream. As with $\underline{Q}^U$ and $\underline{Q}^D$, the wavevectors will be related through the deformation tensor. The three vectors $\underline{\Omega}^D$, $\underline{Q}^D$ and $\underline{k}^D$ form an orthogonal system. In addition, $\underline{k}^D$ will be assumed to be in the direction $\underline{\Omega}^D \times \underline{Q}^D$ so that the system is right handed. Define vectors $\underline{e}_1^D$, $\underline{e}_2^D$, $\underline{e}_3^D$ along $\underline{\Omega}^D$, $\underline{Q}^D$ and $\underline{k}^D$ respectively. Likewise, for the upstream values $\underline{\Omega}^U$, $\underline{Q}^U$, $\underline{k}^U$ define the coordinate system with unit vectors $\underline{e}_1^U$, $\underline{e}_2^U$, $\underline{e}_3^U$. First the relations between $\underline{e}_\alpha^U$ and $\underline{e}_\beta^D$ will be determined and then the relation between $\underline{k}^U$and $\underline{k}^D$. As a matter of notation, note that subscripts here can refer to either components of a vector as in the Cartesian tensor notation of Equation A.16, or to a specific vector such as $\underline{e}_1$, $\underline{e}_2$, $\underline{e}_3$. Generally the meaning will be clear from the context since the

underlined $\underline{e}$ already indicates a vector and the 1, 2, 3 then indicate a specific vector, not the component of a vector.

The relation between $\underline{e}_1^U$ and $\underline{e}_1^D$ is readily obtained from the knowledge that vortex lines follow fluid particles. Since $\underline{e}_1$ is parallel to $\underline{\Omega}$, Equation A.11 immediately gives $\underline{e}_1^D$; i.e.,

$$(f_1^U)_i = (e_1^D)_j \frac{\partial x_i}{\partial \xi_j} \tag{A.17a}$$

$$\underline{e}_1^U = \underline{f}_1^U / \left| \underline{f}_1^U \right| \tag{A.17b}$$

where the j subscript on e^D, now indicates one of three Cartesian components of the vector $\underline{e}_1^D$. Also, the summation convection over repeated indices is assumed.

To calculate the vector $\underline{e}_2^U$, it is not sufficient to just substitute a subscript 2 for 1 in Equation A.17. The resulting vector so defined would not necessarily be orthogonal to $\underline{e}_1^U$. Therefore, a different approach will be used, first calculating $\underline{e}_3^U$, then $\underline{e}_2^U$. First define a vector

$$(f_2^U)_i = (e_2^D)_j \frac{\partial x_i}{\partial \xi_j} \tag{A.18}$$

As noted above, this vector will not in general be orthogonal to $\underline{e}_1^U$. However, it will lie in the same plane of vorticity as $\underline{e}_1^D$ and $\underline{e}_2^D$. For example, consider a plane of vortex lines defined by the vectors $\underline{e}_1^D$ and $\underline{e}_2^D$. Because the vorticity moves with the fluid and because Equation A.18 is a Lagrangian type of equation following fluid particles, $\underline{f}_2^U$ must lie in the same plane of vortex lines. Thus, although we haven't yet determined $\underline{e}_2^U$, $\underline{e}_3^U$ can be determined since it must be normal to the plane defined by $\underline{e}_1^U$ and $\underline{f}_1^U$; i.e.,

$$\underline{e}_3^U = \underline{e}_1^U \times \underline{f}_2^U / \left| \underline{e}_1^U \times \underline{f}_2^U \right| \tag{A.19}$$

where, as in Equation A.17, the denominator is for the purpose of normalizing the result to a unit vector.

Finally, $\underline{e}_2^U$ can be found directly from $\underline{e}_1^U$ and $\underline{e}_3^U$; i.e.,

$$\underline{e}_2^U = \underline{e}_3^U \times \underline{e}_1^U \tag{A.20}$$

Now the relation between $\underline{k}^U$ and $\underline{k}^D$ can be determined. This relation is found from the relations between wavenumber k and wavelength λ

$$k^U = 2\pi/\lambda^U \tag{A.21a}$$

$$k^D = 2\pi/\lambda^D \tag{A.21b}$$

along with the value of $\underline{f}_3^U$ from Equation A.19a and the knowledge that $\underline{k}^U$ and $\underline{k}^D$ are parallel to the vectors $\underline{e}_3^U$ and $\underline{e}_3^D$ respectively. Consider a vector $\lambda^D \underline{e}_3^D$ in the downstream fluid. If this vector begins on the crest of a wave of the turbulence wavevector component, it will reach just to the next crest since the vector has magnitude λ^D; see Figure 24. In the pre-contraction fluid upstream, the vector will again begin and end on the corresponding adjacent crests, but not necessarily along the shortest distance; i.e., the vector will not necessarily be along $\underline{e}_3^U$. If this upstream vector is denoted $\underline{g}_3^U$, then

$$(g_3^U)_i = \lambda^D (e_3^D)_j \frac{\partial x_i}{\partial \xi_j} \tag{A.22}$$

The component of $\underline{g}_3^U$ in the direction of $\underline{e}_3^U$ must have a length λ^U from the above discussion. Thus

$$\lambda^U = \underline{g}_3^U \cdot \underline{e}_3^U = \lambda^D (e_3^U)_i (e_3^D)_j \frac{\partial x_i}{\partial \xi_j} \tag{A.23}$$

From Equation A.21

$$k^D/k^U = (e_3^U)_i (e_3^D)_j \frac{\partial x_i}{\partial \xi_j} \tag{A.24}$$

From the above equations the relations between the upstream and downstream values of both wavenumber and velocity can be determined. The procedure is first to find the upstream $\underline{e}_\alpha^U$ vectors from the downstream $\underline{e}_\beta^D$ vectors using Equations A.17 through A.20. The ratio k^D/k^U can then be found from Equation A.24. Finally, $\underline{Q}^U$ can be found from Equation A.16.

It should be pointed out that the several vector operations in Equation A.16 need not actually be carried out. The necessary operations have already been performed in deriving $\underline{e}_\alpha^U$. Thus, since k_ℓ^D and Q_m^D are orthogonal,

$$k_\ell^D \, Q_m^D \, \epsilon_{\ell mn} = - (e_l^D)_n \, k^D \, Q^D \tag{A.25}$$

Now, $(e_{l_U}^D)_j \, \partial x_i / \partial \xi_j$ has already been calculated in Equation A.17 and it is a vector $\underline{f}_l^U$ parallel to $\underline{e}_l^U$. Thus, Equation A.16 can be written

$$\underline{Q}^U (\underline{k}^U) = Q^D (\underline{k}^D) \, f_l^U \, \underline{e}_2^U \, k^D / k^U \tag{A.26}$$

A computer program was initially written using Equation A.16. This was later changed to the simplified version using Equation A.26. The programs were found to agree, so Equation A.16 need only be used for descriptive purposes.

Comparison with Results of Ribner and Tucker

Wavenumber Relation. Ribner and Tucker (Ref. 38) have performed this same analysis, but for the restricted case where the deformation tensor is diagonal. The present results will be examined to see if they reduce to the results of Reference 38. The deformation considered by Reference 38 is

$$\left[\frac{\partial x_i}{\partial \xi_j}\right] = \begin{bmatrix} \ell_1^{-1} & 0 & 0 \\ 0 & \ell_2^{-1} & 0 \\ 0 & 0 & \ell_3^{-1} \end{bmatrix} \tag{A.27}$$

The relation between upstream and downstream wavevectors given in Reference 38 is

$$\underline{k}^D = \left(\frac{k_1^U}{\ell_1}, \frac{k_2^U}{\ell_2}, \frac{k_3^U}{\ell_3} \right) \tag{A.28}$$

This can be shown to follow from Equations A.24 and A.27; i.e., multiplication of Equation A.24 by k^D gives

$$k^{D^2} = k_i^U k_j^D \frac{\partial x_i}{\partial \xi_j} = k_1^U k_1^D \ell_1^{-1} + k_2^U k_2^D \ell_2^{-1} + k_3^U k_3^D \ell^{-1}{}_3 \quad \text{(A.29)}$$

This equation will hold for all k values if

$$\begin{aligned} k_1^U / \ell_1 &= k_1^D \\ k_2^U / \ell_2 &= k_2^D \\ k_3^U / \ell_3 &= k_3^D \end{aligned} \quad \text{(A.30)}$$

Equations A.30 agree with Equation A.28. Thus, the procedure for calculation of $\underline{k}^U$ from $\underline{k}^D$ presented here reduces to that of Ribner and Tucker for a diagonal deformation tensor.

Velocity Relation. Equation A.16 for the relation between upstream and downstream velocities can similarly be reduced to the form given in Reference 38. Notation presents a minor problem in that the use of the Cartesian indices can be confusing. Here the notation will be that a subscript in parentheses is a duplicate index and is not summed over unless the index appears twice elsewhere in the expression. Thus, $A_i B_{(i)}$ implies no summation over i but the variable B has the same subscript as A. However, for $A_i B_i C_{(i)}$, summation over i is assumed with C in each term of the summation taking the same subscript as A and B.

Rewriting Equation A.16 into the form used by Reference 38 which relates the downstream velocity $\underline{Q}^D$ to the upstream value $\underline{Q}^U$ (rather than vice versa as in Equation A.16)

$$Q_i^D = -(k_j^D / k^{D^2})\, k_\ell^U \; Q_m^U \, \epsilon_{\ell mn} \, \epsilon_{ijk} \frac{\partial \xi_k}{\partial x_n} \quad \text{(A.31)}$$

Using the inverse of Equation A.27 gives

$$Q_i^D = -(k_j^D / k^{D^2}) \; k_\ell^U \; Q_m^U \; \epsilon_{\ell mn} \, \epsilon_{ijk} \; \ell_{(n)} \quad \text{(A.32)}$$

Now

$$\ell_1 \ \ell_2 \ \ell_3 = 1 \tag{A.33}$$

for incompressible flow since the determinant of the deformation matrix must be 1 as discussed previously. Then since $\epsilon_{ijn} = 0$ unless i=j=n, Equation A.32 can be written

$$Q_i^D = -\left(k_j^D / k^{D^2}\right) k_\ell^U \ Q_m^U \ \epsilon_{\ell mn} \ \epsilon_{ijk} \left[\ell_{(i)} \ \ell_{(j)}\right]^{-1} \tag{A.34}$$

Using the relation

$$\epsilon_{ijn} \ \epsilon_{\ell mn} = \delta_{i\ell} \ \delta_{jm} - \delta_{im} \ \delta_{j\ell} \tag{A.35}$$

Equation A.34 becomes

$$Q_i^D = \left(k_j^D / k^{D^2}\right) \left[\ell_{(i)} \ \ell_{(j)}\right]^{-1} \left(k_j^U \ Q_i^U - k_i^U \ Q_j^U\right) \tag{A.36}$$

Introducing Equation A.30

$$Q_i^D = \frac{1}{\ell_{(i)}} \left[Q_i^U - \frac{k_j^U \ k_i^U}{\ell_{(j)}^2 \ k^{D^2}} \ Q_j^U\right] \tag{A.37}$$

But this is exactly Equation 13 of Reference 38. Thus, the present result relating upstream and downstream velocity reduces to the previously derived result of Ribner and Tucker for the case of diagonal deformation tensor.

REFERENCES

1. George, A. R.: "Helicopter Noise: State-of-the-Art," Journal of Aircraft, Vol. 15, No. 11, pp. 707-715, November 1978.

2. Brooks, T. F. and R. H. Schlinker: "Progress in Rotor Broadband Noise Research," Vertica, Vol. 7, No. 4, pp. 287-307, 1983.

3. Sharland, I. J.: "Sources of Noise in Axial Flow Fans," J. Sound and Vibration, Vol. 1, pp. 302-322, 1964.

4. Dean, L. W.: "Broadband Noise Generated by Airfoils in Turbulent Flow," AIAA Paper 71-587, June 1971.

5. Mugridge, B. D.: "Sound Radiation from Airfoils in Turbulent Flow," J. Sound and Vibration, Vol. 13, No. 3, pp. 362-363, Nov. 1970.

6. Mani, R.: "Noise Due to Interaction of Inlet Turbulence With Isolated Stators and Rotors," J. Sound and Vibration, Vol. 17, No. 2, pp. 251-260, 1971.

7. Amiet, R. K.: "Acoustic Radiation from an Airfoil in a Turbulent Stream," J. Sound and Vibration, Vol. 41, pp. 407-420, 1975.

8. Paterson, R. W. and R. K. Amiet: "Acoustic Radiation and Surface Pressure Characteristics of an Airfoil Due to Incident Turbulence," NASA CR-2733, 1976.

9. Homicz, G. F. and A. R. George: "Broadband and Discrete Frequency Radiation from Subsonic Rotors," J. Sound and Vibraton, Vol. 36, pp. 151-177, 1974.

10. Amiet, R. K.: "Noise Produced by Turbulent Flow into a Propeller or Helicopter Rotor," AIAA Paper 76-560, 1976. (Also published in synoptic form in AIAA Journal, Vol. 15, No. 3, pp. 307-308, March 1977.

11. George, A. R. and S. J. Chow: "Broadband Rotor Noise Analyses," NASA CR-3797, 1984.

12. George, A. R. and Y. N. Kim: "High Frequency Broadband Rotor Noise," AIAA Journal, Vol. 15, pp. 538-545, 1977.

13. Paterson, R. W. and R. K. Amiet: "Noise of a Model Helicopter Rotor Due to Ingestion of Turbulence," NASA CR-3213, 1979.

14. Teunissen, H. W., "Characteristics of the Mean Wind and Turbulence in the Planetary Boundary Layer," UTIAS Review 32, University of Toronto Institute for Aerospace Studies, October 1970.

15. Snyder, W. H., "Guideline for Fluid Modeling of Atmospheric Diffusion," Environmental Protection Agency, Fluid Modeling Report No. 10, April 1981.

16. Fairall, C. W., K. L. Davidson, and G. E. Schacher, "A Review and Evaluation of Integrated Atmospheric Boundary-Layer Models for Maritime Applications," Naval Postgraduate School Report NPS-63-81-004, November, 1981.

17. Campbell, C. W., "A Spatial Model of Wind Shear and Turbulence for Flight Simulation," NASA TP-2313, May, 1984.

18. Gunter, D. E., G. W. Jones, J. W. Jones, and K. R. Monson, "Low altitude Atmospheric Turbulence, Lo-Locat Phases I and II," ASD-TR-69-12, Wright-Patterson Air Force Base, Ohio, February 1969.

19. Counihan, J., "Adiabatic Atmospheric Boundary Layer: A Review and Analysis of Data from the Period 1880-1972," Atmos. Envir., Vol. 9, No. 10, pp. 871-905, 1975.

20. Deardorff, J. W., "Numerical Investigation of Neutral and Unstable Planetary Boundary Layers," J. Atmos. Sci., Vol. 29, pp. 91-115, January, 1972.

21. Blackadav, A. K. and H. Tennekes, "Asymptotic Similarity in Neutral Barotropic Planetary Boundary Layers," J. Atmos. Sci., Vol. 25, pp. 1015-1020, 1968.

22. Arya, S. P. S., "Suggested Revisions to Certain Boundary Layer Parameterization Schemes Used in Atmospheric Circulation Models," Monthly Weather Review, Vol. 105, No. 2, pp. 215-227, February 1977.

23. Kaimal, J. C., "Turbulence Spectra, Length Scales and Structure Parameters in the Stable Surface Layer," Boundary Layer Meteorol., Vol. 4, pp. 289-309, 1973.

24. Sadler, S. G., "Method for Predicting Helicopter Wake Geometry, Wake-Induced Flow and Wake Effects on Blade Airloads," American Helicopter Society Paper 71-523, 1971.

25. Reddy, K. R., "Rotor Wake Model for Forward Flight Simulation Studies," ARL Aero Note 402, June 1981.

26. Caradonna, F. X. and M. P. Isom, "Numerical Calculation of Unsteady Transonic Potential Flow over Helicopter Rotor Blades," AIAA Paper 75-168, January 1975.

27. Roberts, T. W. and E. M. Murman, "A Computational Method for Helicopter Vortex Wakes," AIAA Paper No. 84-1554, June 1984.

28. Thuy, T. C., and J. Renaud, "Theoretical Prediction of Aerodynamic and Dynamic Phenomena on Helicopter Rotors in Forward Flight," ONERA TP 1976-16, 1976.

29. Landgrebe, A. J., "An Analytical Method for Predicting Rotor Wake Geometry," AIAA Paper No. 69-196, February 1969.

30. Egolf, T. A., and A. J. Landgrebe, "Helicopter Rotor Wake Geometry and Its Influence in Forward Flight. Volume I - Generalized Wake Geometry," NASA CR-3726, October 1983.

31. Egolf, T. A., and A. J. Landgrebe, "Helicopter Rotor Wake Geometry and Its Influence in Forward Flight. Volume II - Wake Geometry Charts," NASA CR-3727, October 1983.

32. Lighthill, M. J., "Drift," Vol. 1, pp. 31-53, 1956 (Corrigenda, Vol. 2, pp. 311-312, 1957).

33. Landgrebe, A. J., and T. A. Egolf, "Rotorcraft Wake Analysis for the Prediction of Induced Velocities," United Technologies Research Center, USAAMRDL Technical Report 75-45, U.S. Army Air Mobility Research and Development Laboratory, Fort Eustis, VA, January 1976.

34. Gessow, A., and G. C. Myers, Aerodynamics of the Helicopter, MacMillan, New York, 1952.

35. Kuchemann, D. and J. Weber, Aerodynamics of Propulsion, McGraw-Hill, 1953.

36. Castles, W., Jr., and J. H. De Leeuw, "The Normal Component of the Induced Velocity in the Vicinity of a Lifting Rotor and Some Examples of Its Application," NACA TR 1184, 1953.

37. Shampine, L. F. and M. F. Gordon, Computer Solution of Ordinary Differential Equations: The Initial Value Problem, Freeman Pub., 1975.

38. Ribner, H. S. and M. Tucker, "Spectrum of Turbulence in a Contracting Stream," NACA Technical Report 1113, 1953.

39. Batchelor, G. K. and I. Proudman, "The Effect of Rapid Distortion of a Fluid in Turbulent Motion," Quart. Journ. Mech. and Applied Math, Vol. VII, Pt. 1, 1954.

40. Batchelor, G. K., An Introduction to Fluid Dynamics, Chapter 5, Cambridge University Press, 1967.

41. Hunt, J. C. R., "A Theory of Turbulent Flow Round Two- Dimensional Bluff Bodies," J. Fluid Mech., Vol. 61, pp. 625-706, 1973.

42. AGARD CP-214 "Secondary Flows in Turbomachines," 1977.

43. Hawthorne, W. R., "The Applicability of Secondary Flow Analysis to the Solution of Internal Flow Problems" In Fluid Mechanics of Internal Flows ed. by G. Sovran, Elsevier Press, 1967.

44. Horlock, J. H. and B. Lakshminaravana, "Generalized expressions for secondary vorticity using intrinsic co-ordinates," J. Fluid Mech., Vol. 59, pp. 97-115, 1973.

45. De Siervi, F., H. C. Viguier, E. M. Greitzer, and C. S. Tan, "Mechanisms of Inlet Vortex Formation," J. Fluid Mech., Vol. 124, pp. 173-207, 1982.

46. Hawthorne, W. R., "On the theory of Shear flow," Gas Turbine Lab. (Massachusetts Institute of Technology) Report No. 88, 1966.

47. Britter, R. E., J. C. R. Hunt, and J. C. Mumford, "The Distortion of Turbulence by a Circular Cylinder," J. Fluid Mech., Vol. 92, pp. 269-301, 1979.

48. Hunt, J. C. R., "A Review of the Theory of Rapidly Distorted Turbulent Flows and its Applications," Fluid Dynamic Transactions, Vol. 9, Ed. by W. Fiszdon. et. al., 1978.

49. Goldstein, M. E., "Unsteady Vortical and Entropic Distortions of Potential Flows Around Arbitrary Obstacles," J. Fluid Mech., Vol. 89, pp. 433-468, 1978.

50. Goldstein, M. E. and P. A. Durbin, "The Effect of Finite Turbulence Spatial Scale on the Amplification of Turbulence by a Contracting Stream," J. Fluid Mech., Vol. 98, pp. 473-508, 1980.

51. Tsuge, S., "Effects of Flow Contraction on Evolution of Turbulence," Phys. Fluids, Vol. 27, No. 8, pp. 1948-1956, 1984.

52. Lighthill, M. J., "A Simple Fluid-Flow Model of Ground Effect on Hovering," J. Fluid Mech., Vol. 93, pp. 781-797, 1979.

53. Tan-Atichat, J., H. N. Nagib, and R. E. Drubka, "Effects of Axisymmetric Contractions on Turbulence of Various Scales," NASA CR-165136, 1980.

54. Hinze, J. O., Turbulence, p. 190, McGraw-Hill, Second Edition, 1975.

55. Amiet, R. K., "The Spectrum of Turbulence Undergoing a Rapid Distortion," United Technologies Research Center Report, UTRC84-26, 1984. (Available on request).

56. Lamb, H., Hydrodynamics, Sixth Edition, Dover Publications, New York, 1932.

57. Goldstein, M. E. and H. Atassi, "A Complete Second-Order Theory for the Unsteady Flow About an Airfoil Due to a Periodic Gust," J. Fluid Mech., Vol. 74, pp. 741-765, 1976.

58. Paterson, R. W. and R. K. Amiet, "Noise and Surface Pressure Response of an Airfoil to Incident Turbulence," J. Aircraft, Vol. 14, pp. 729-736, 1977.

59. Amiet, R. K., "Noise Due to Rotor Turbulence Interaction," NASA Helicoptor Acoustics CP-2052, pp. 109-126, 1978.

60. Paterson, R. W. and R. K. Amiet, "Noise of a Model Helicopter Rotor due to Ingestion of Isotropic Turbulence," J. Sound and Vibration, Vol. 85, pp. 551-577, 1982.

61. Bendat, J. S. and A. G. Piersol, Measurement and Analysis of Random Data, John Wiley and Sons, Inc., 1965.

62. Lowson, M. V., "The Sound Field for Singularities in Motion," Proceedings Royal Society London, Ser. A, Vol. 286, No. 1407, pp. 559-572, August 1965.

63. Schlinker, R. H. and R. K. Amiet, "Helicopter Rotor Trailing Edge Noise," NASA CR-3470, 1981.

TABLE 1

ATMOSPHERIC BOUNDARY LAYER CONDITIONS

L Stability Length (m)	G Wind Speed (m/s)	Z Altitude (m)	δ Boundary Layer Thickness (m)	U_* Friction Velocity (m/s)	L_w^x Integral Length Scale (m)	$\sqrt{w^2}/U_\infty$ Turbulence Intensity
-10	2.6	50	1500	.200	20.0	.253
-10	2.6	122	1500	.200	48.8	.341
-10	2.6	152	1500	.200	61.0	.367
-10	5.1	50	1500	.334	20.0	.211
-10	5.1	122	1500	.334	48.8	.284
-10	5.1	152	1500	.334	61.0	.306
-10	10.3	50	1500	.565	20.0	.179
-10	10.3	122	1500	.565	48.8	.240
-10	10.3	152	1500	.565	61.0	.259
∞	2.6	50	600	.103	20.0	.0575
∞	2.6	122	600	.103	48.8	.0508
∞	2.6	152	600	.103	61.0	.0482
∞	5.1	50	600	.195	20.0	.0575
∞	5.1	122	600	.195	48.8	.0508
∞	5.1	152	600	.195	61.0	.0482
∞	10.3	50	600	.370	20.0	.0575
∞	10.3	122	600	.370	48.8	.0508
∞	10.3	152	600	.370	61.0	.0482
20	2.6	50	131	.070	4.05	.0275
20	2.6	122	131	.070	9.44	.0120
20	2.6	152	131	.070	*	*
20	5.1	50	183	.111	4.05	.0246
20	5.1	122	183	.111	9.44	.0158
20	5.1	152	183	.111	11.7	.0134
20	10.3	50	246	.178	4.05	.0209
20	10.3	122	246	.178	9.44	.0169
20	10.3	152	246	.178	11.7	.0152

* above boundary layer

Latitude, $\theta = 45°$
Roughness height, $Z_o = 0.02$ m
Tropopause height, $Z_T = 11{,}000$ m

TABLE 2

HELICOPTER FLIGHT CONDITIONS

Case	U_∞ Horiziontal Freestream Velocity (m/s)	V_∞ Vertical Freestream Velocity (m/s)	μ Rotor Advance Ratio	V_o Rotor Induced Velocity (m/s)	α Rotor Tip Path Plane Angle of Attack (deg.)	χ Wake Skew Angle (deg.)
FF	20.0	0.0	0.11	2.83	-2.3	79.7
SFF	8.90	0.0	0.49	5.67	-0.2	57.4
HOV5	2.57	0.0	0.014	7.68	0.0	18.5
VERT5	0.0	1.52	0.0	9.41	0.0	0.0
VERT10	0.0	3.05	0.0	10.94	0.0	0.0
VERT20	0.0	6.10	0.0	13.99	0.0	0.0

ΩR, Blade Tip Speed = 182 m/s
R, Radius = 3.854 m
C, Chord = 0.244 m
C_T, Rotor Thrust Coefficient = 0.00377

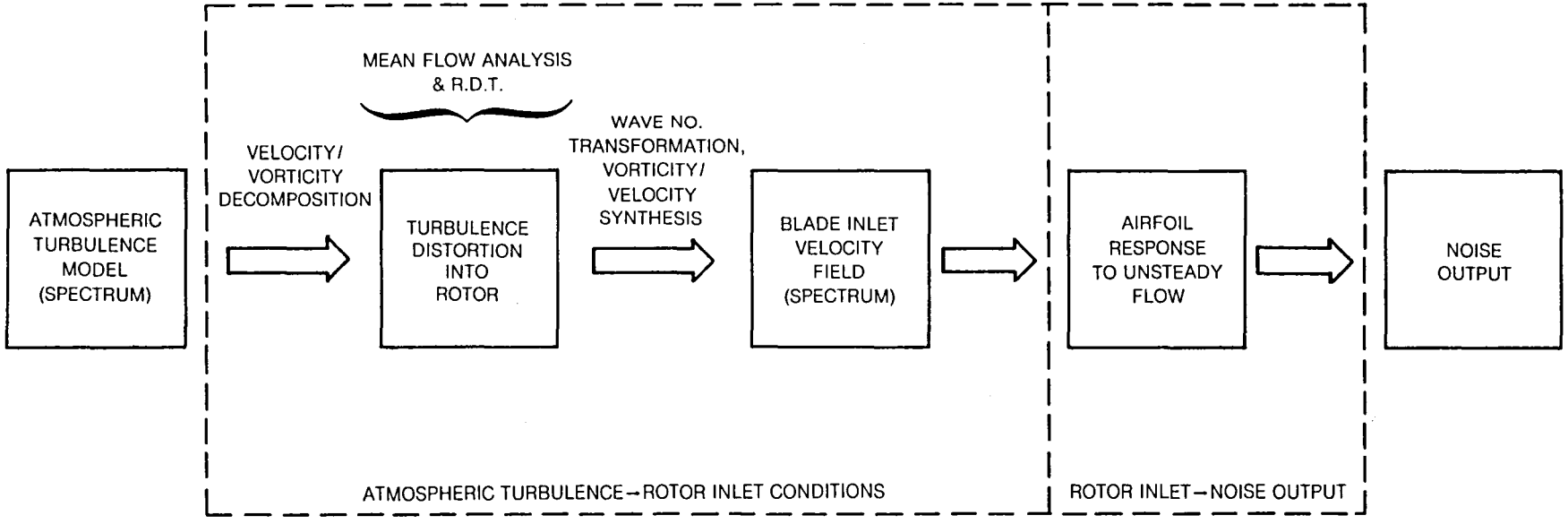

OVERALL "TRANSFER MATRIX"

SCHEMATIC OF PROCESS: $\begin{bmatrix}\text{NOISE}\\ \text{OUTPUT}\end{bmatrix} = \begin{bmatrix}\text{TRANSFER}\\ \text{MATRIX}\end{bmatrix} \begin{bmatrix}\text{ATMOSPHERIC}\\ \text{TURBULENCE}\end{bmatrix}$

Figure 1 — Modules in Overall Prediction Scheme

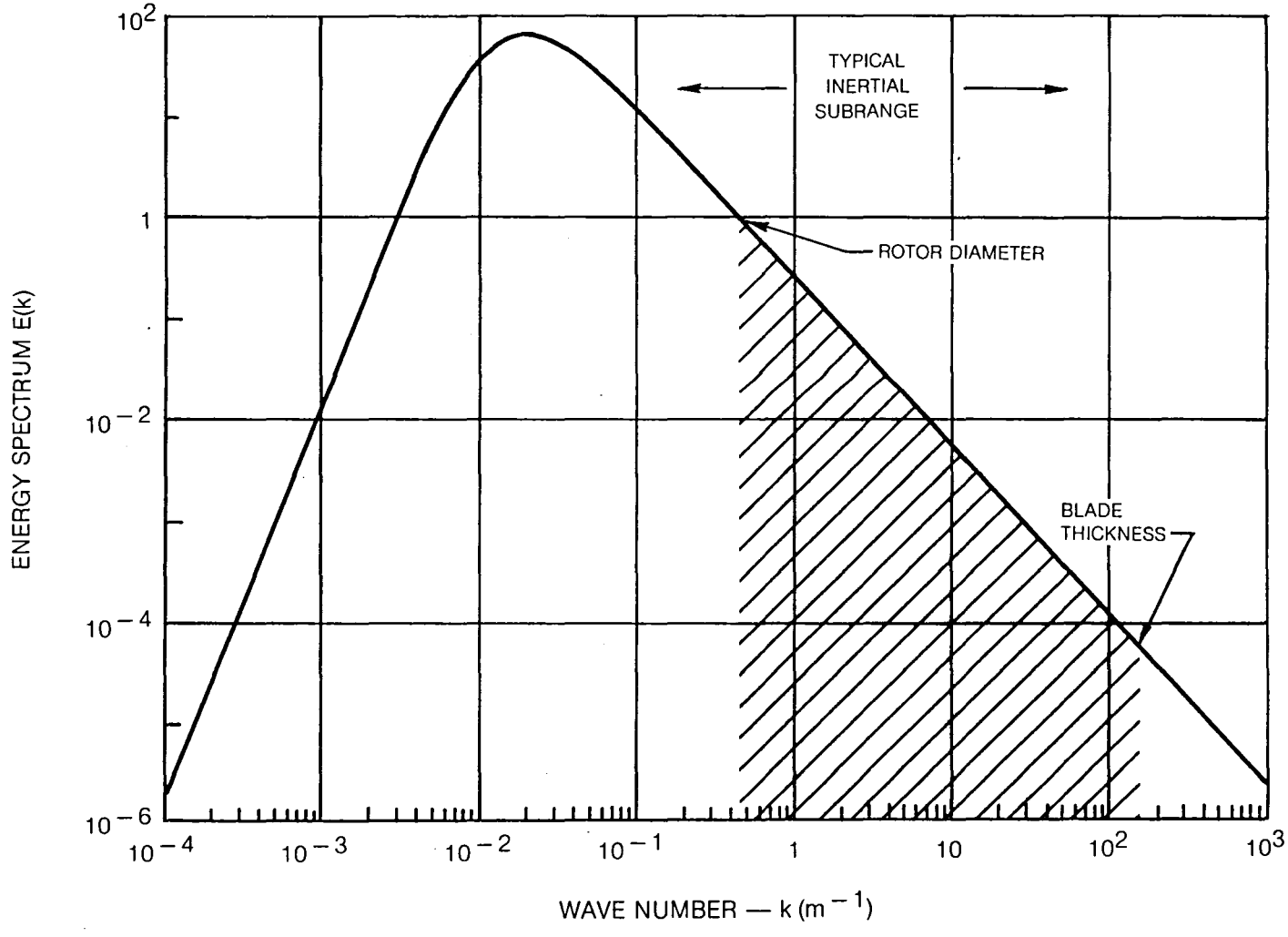

Figure 2 — Wave Number Range of Interest for a Typical Helicopter Rotor Under Typical Atmospheric Conditions

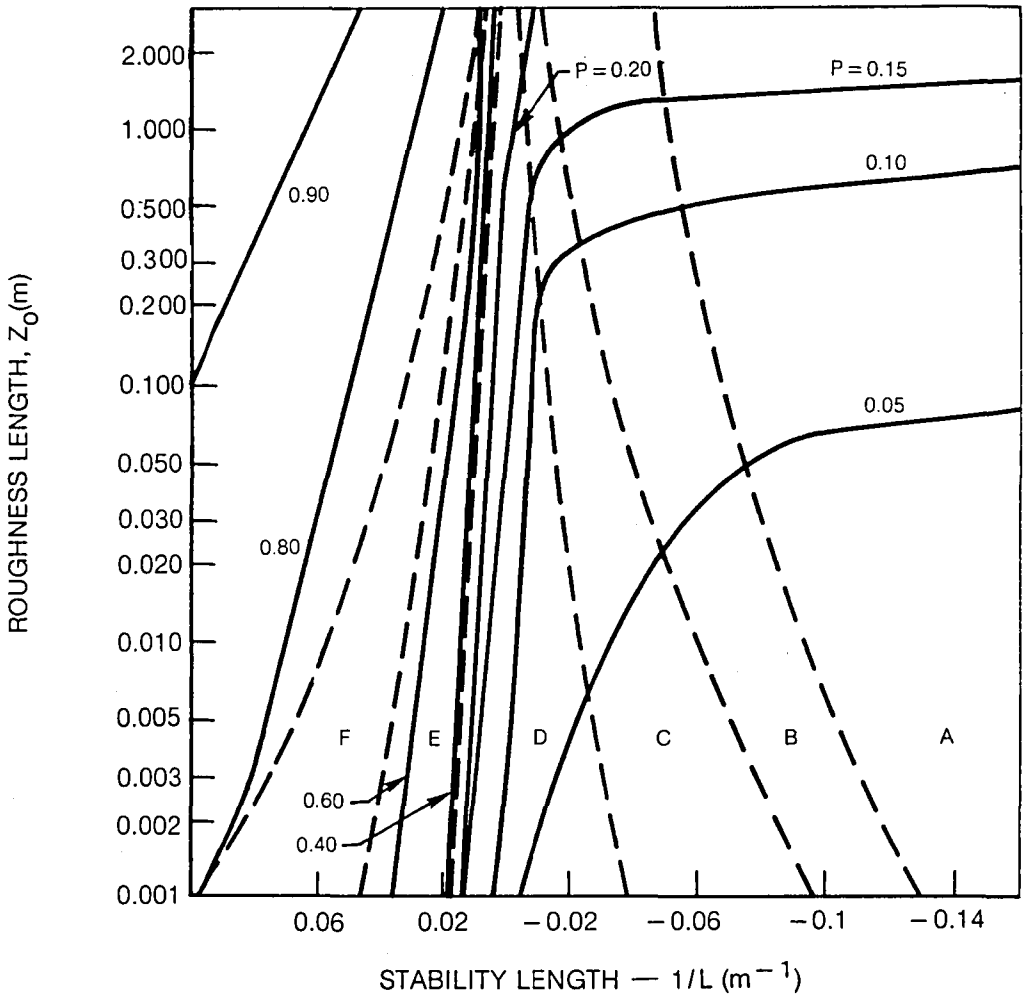

Figure 3 — Theoretical Variation of the Power-Law Exponent (from ref. 2) Dashed Curves are Limits of Pasquill Stability Classes

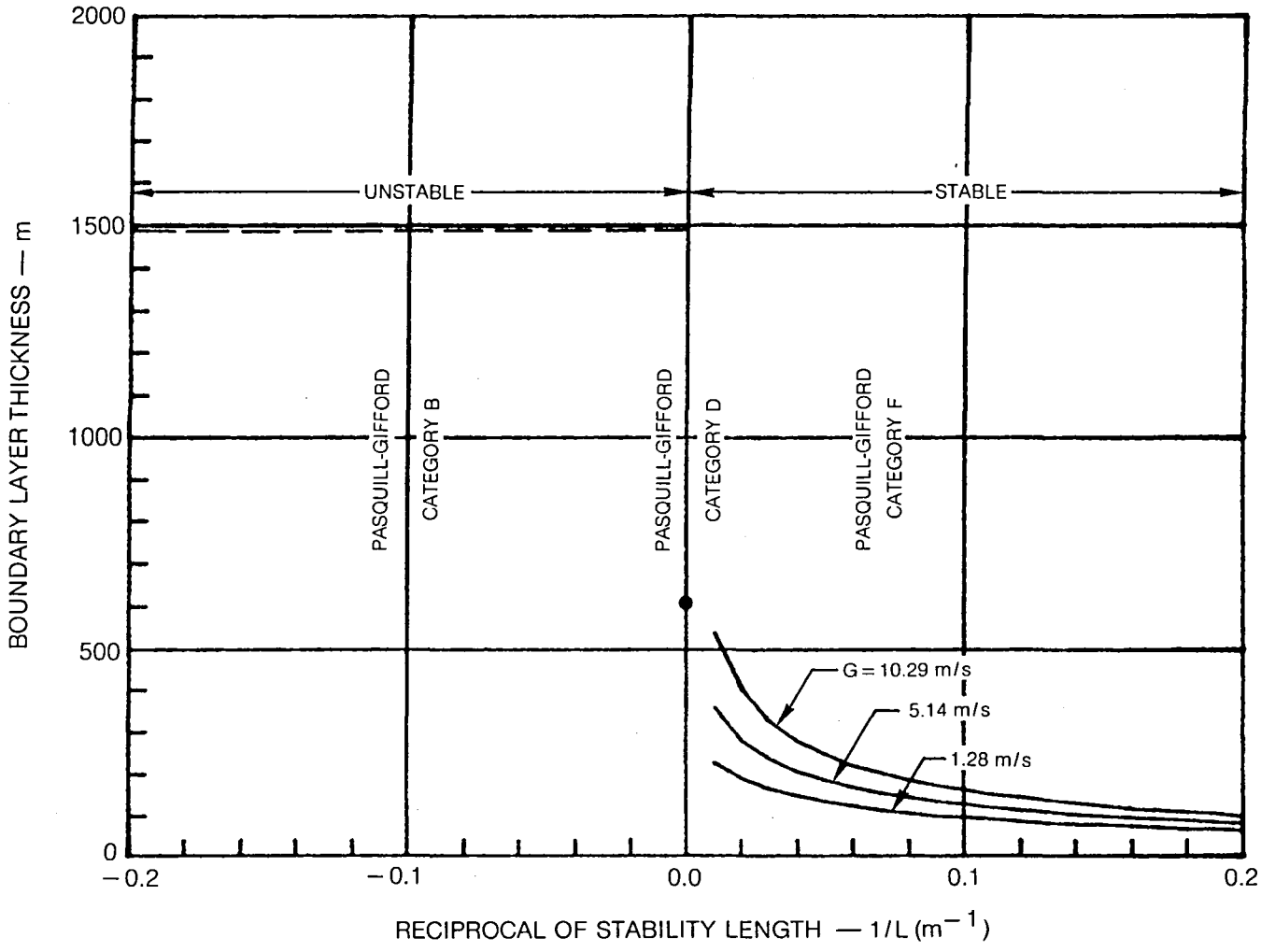

Figure 4 — Effect of Stability Length on Boundary Layer Thickness

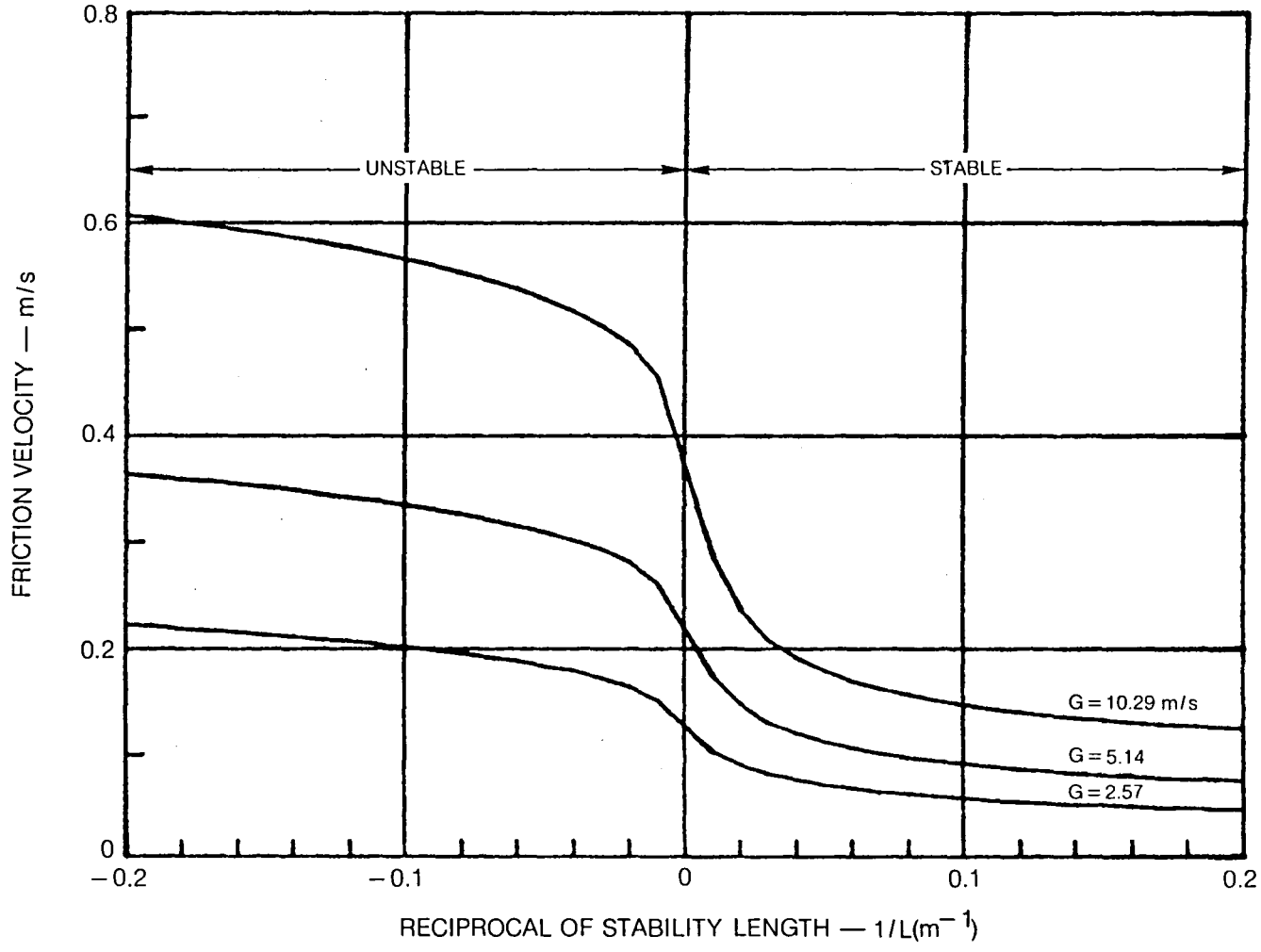

Figure 5 — Effect of Stability Length on Friction Velocity

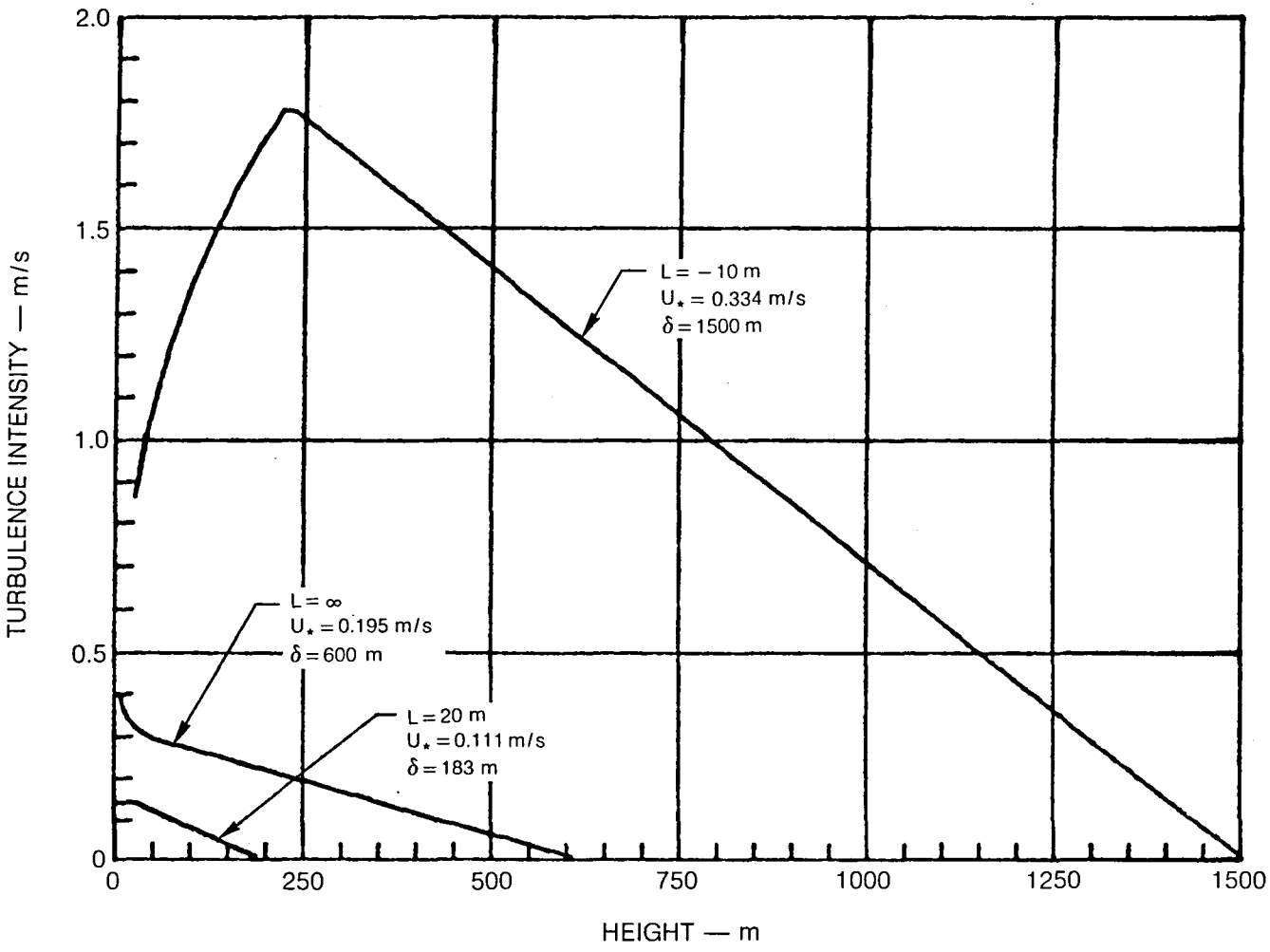

Figure 6 — Effect of Height on Turbulence Intensity, G = 5.14 m/s

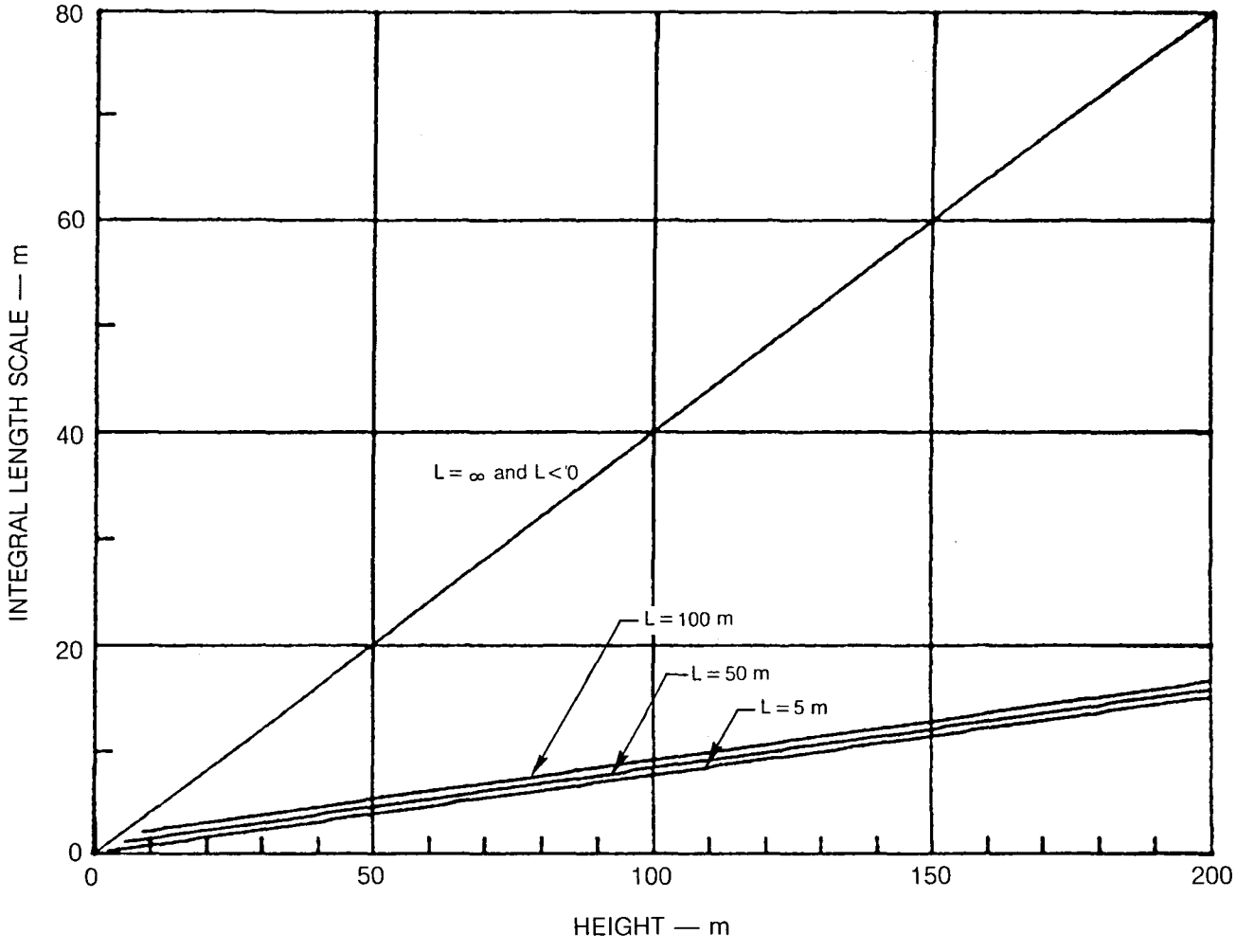

Figure 7 — Effect of Height on Integral Length Scale

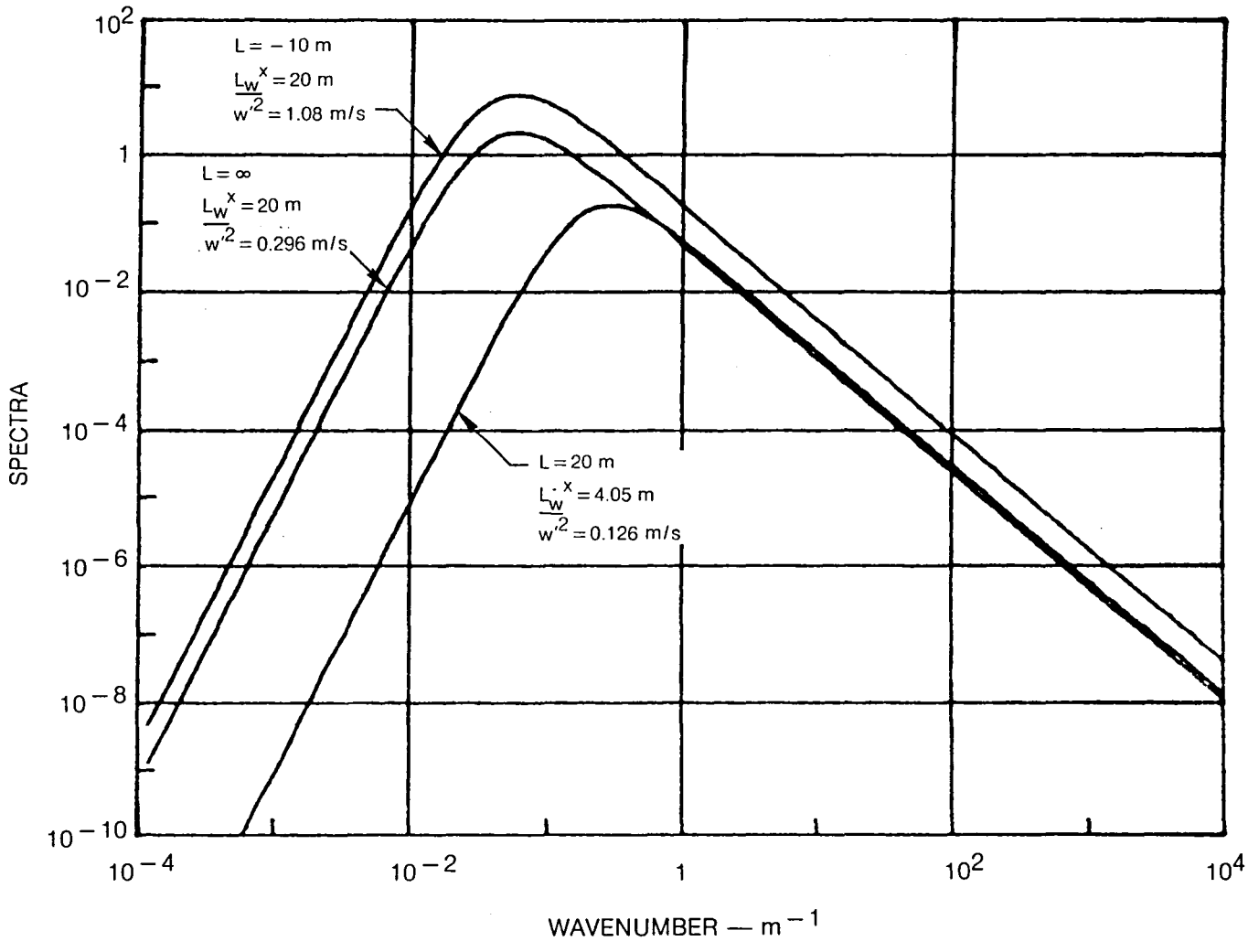

Figure 8 — Effect of Stability Length on Spectra, G = 5.14 m/s, Z = 50 m

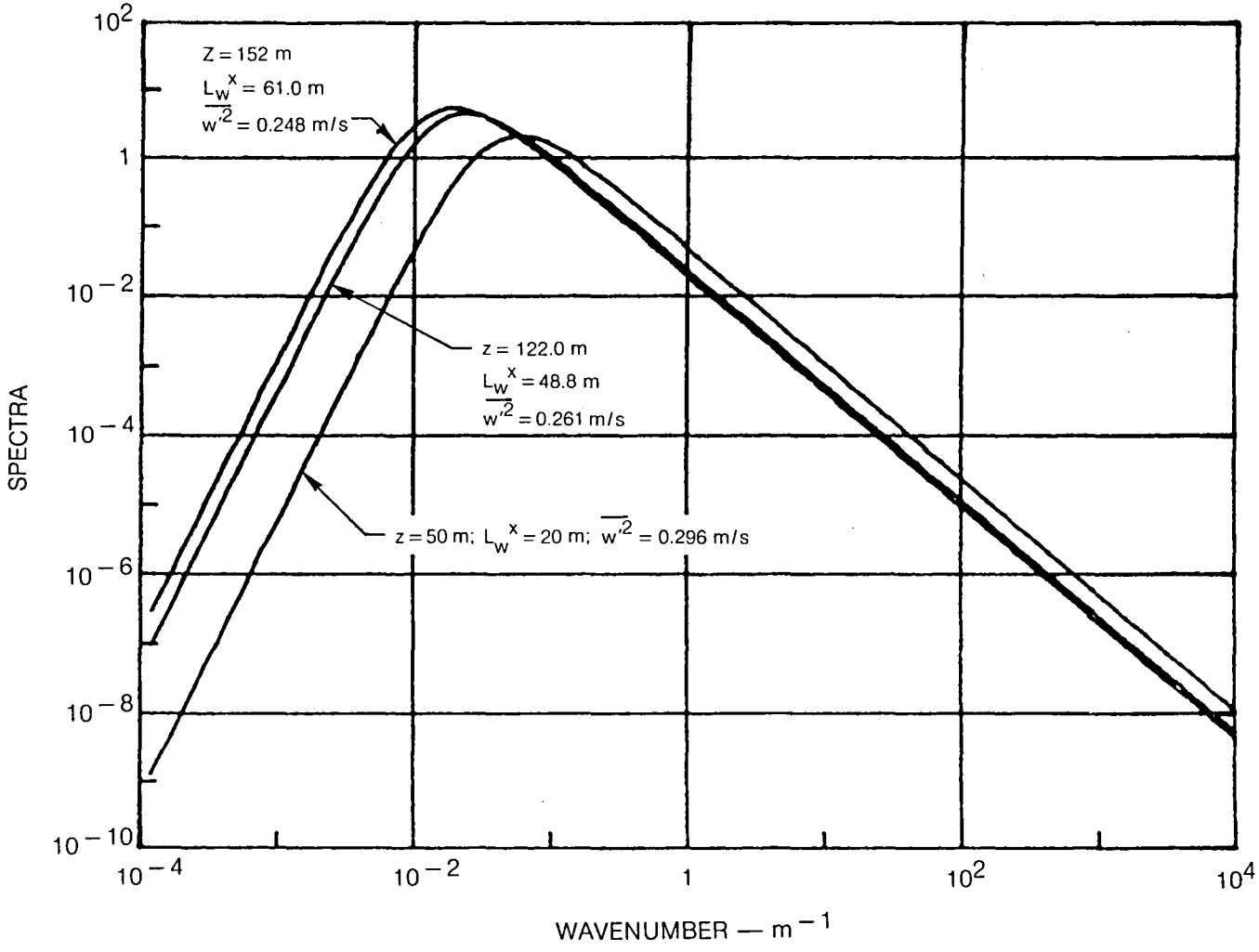

Figure 9 — Effect of Altitude on Spectra, G = 5.14 m/s, L = ∞

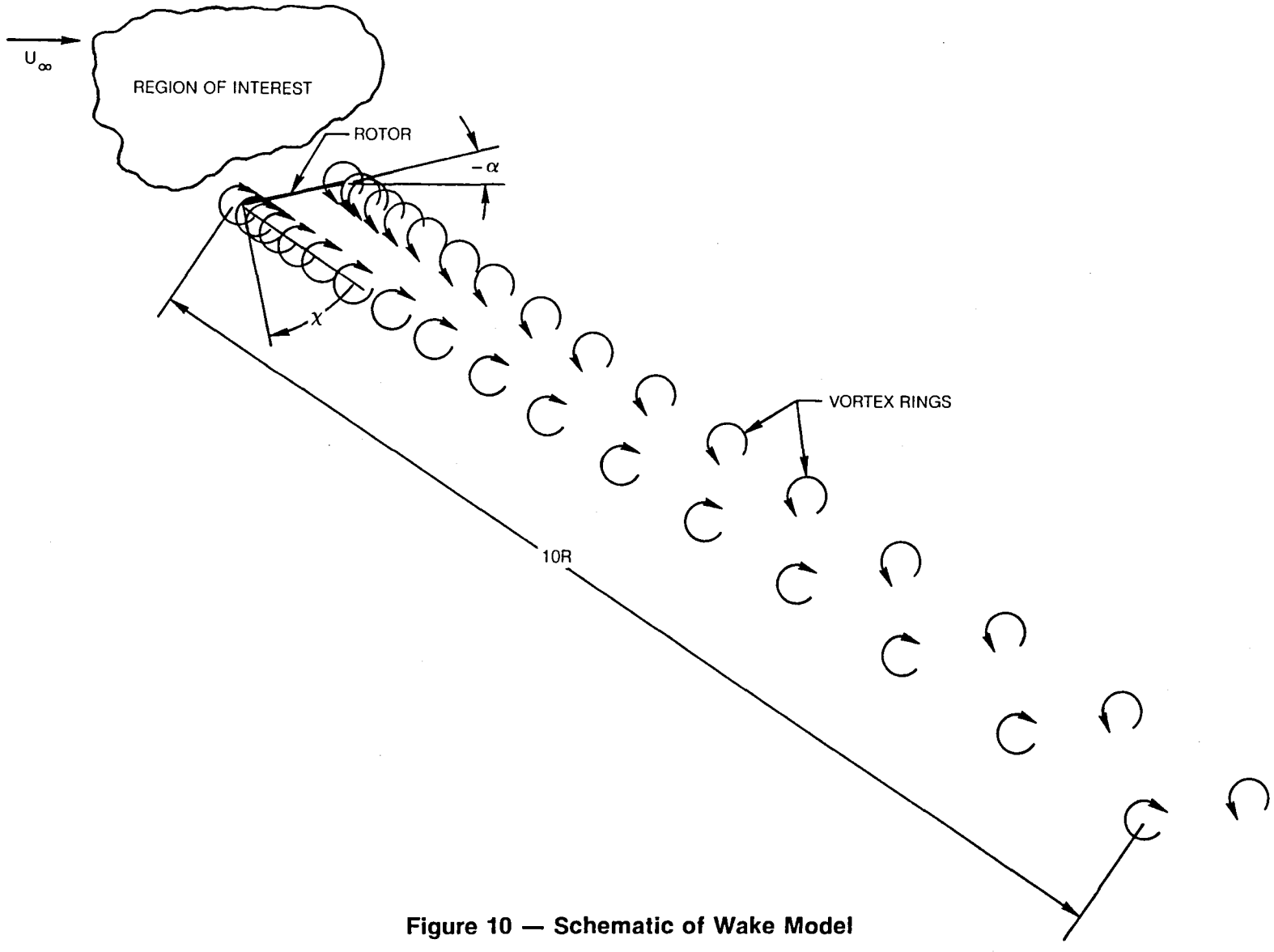

Figure 10 — Schematic of Wake Model

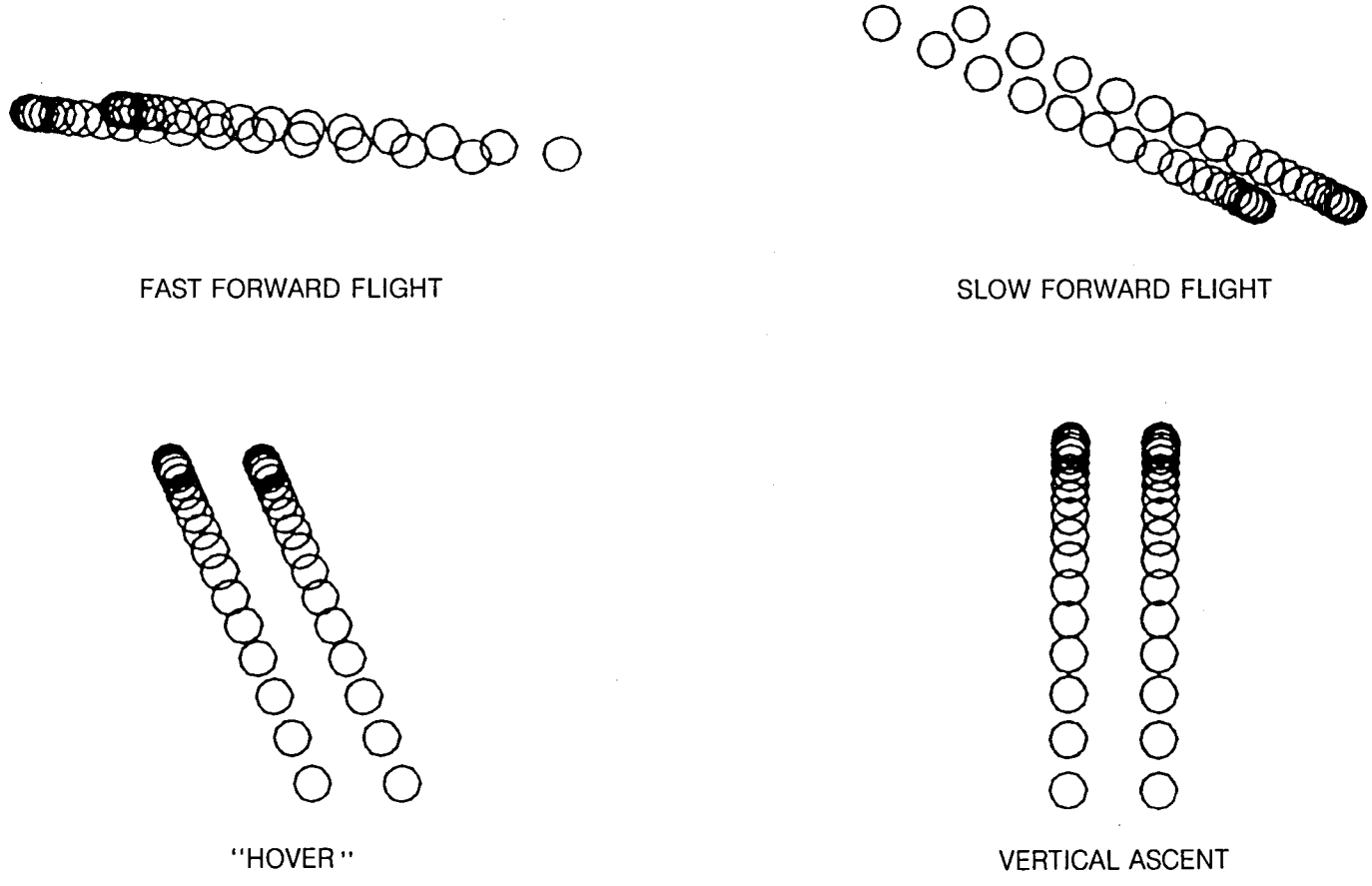

Figure 11 — Ring Vortex Wake Model for Various Flight Conditions

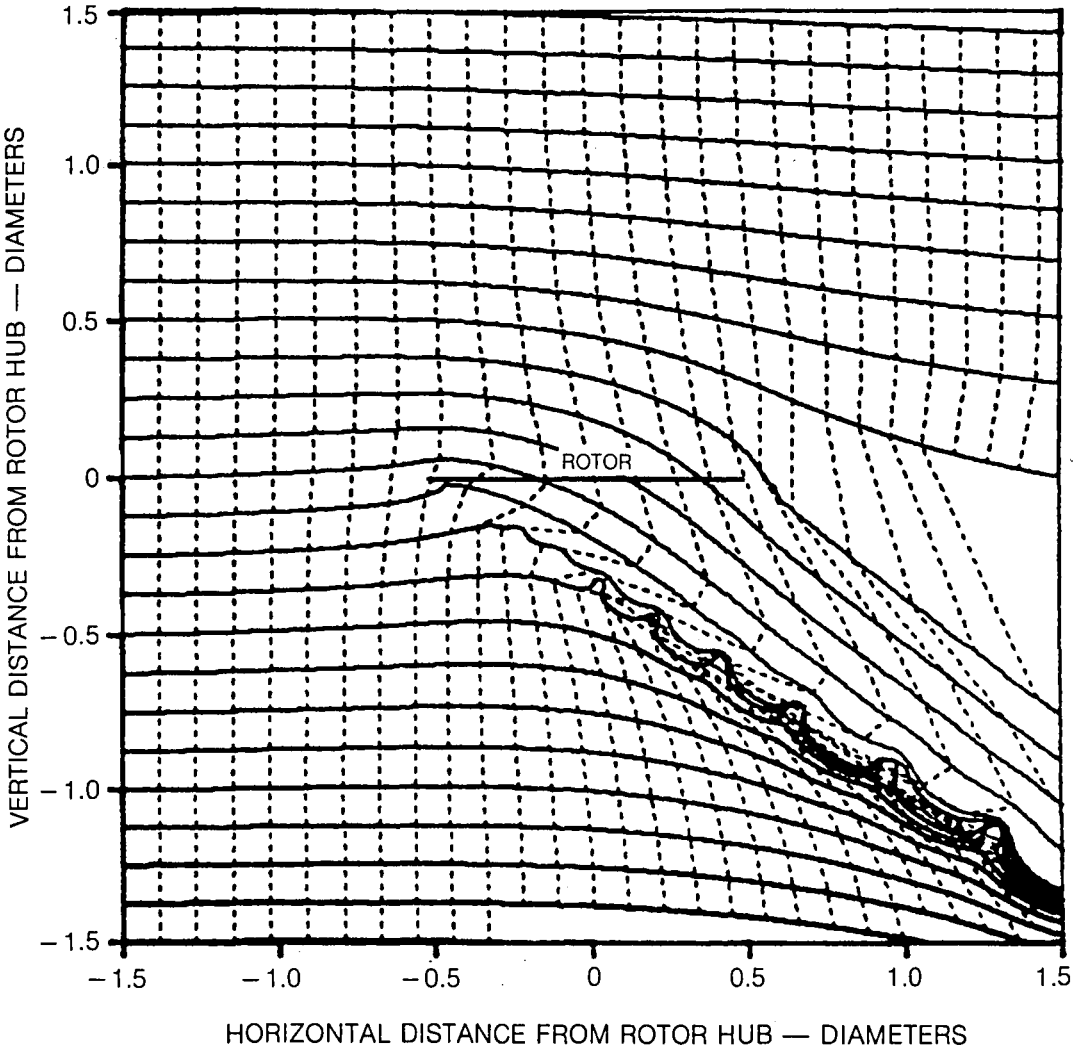

Figure 12 — Prediction of Streamlines (Solid) and Timelines (Dashed) for Flow in a Vertical Plane Through Rotor Hub

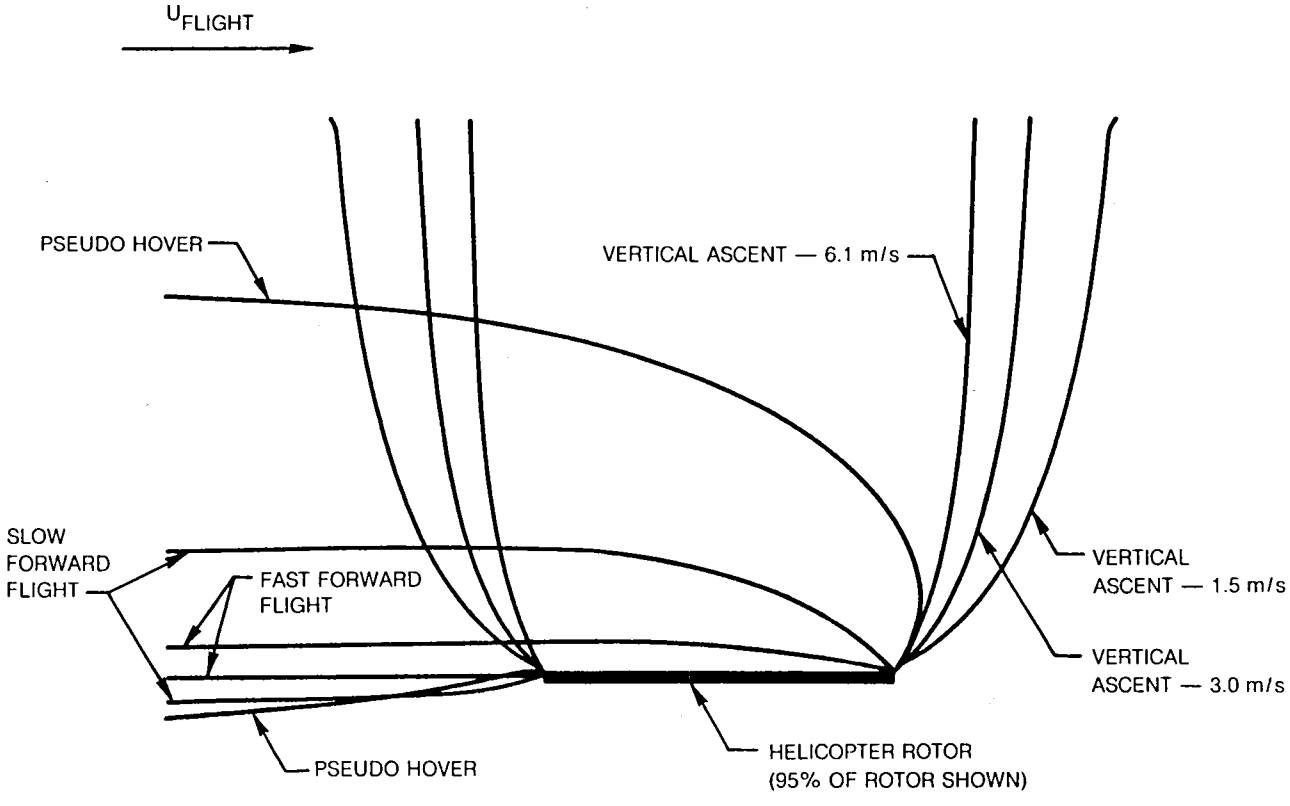

Figure 13 — Streamline Envelope in Vertical Plane Through Centerline for Six Different Operating Conditions

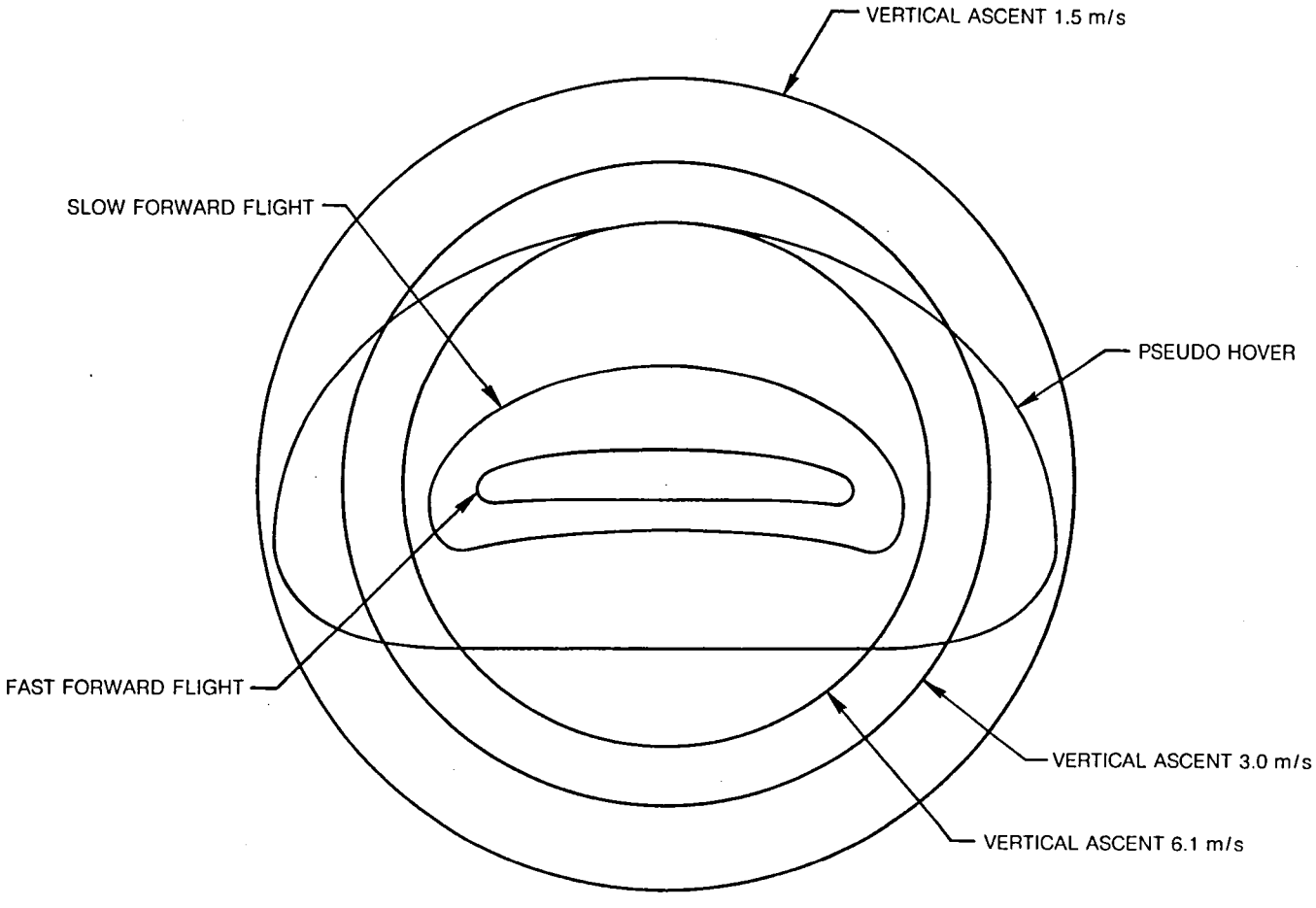

Figure 14 — Capture Surfaces for Six Different Operating Conditions

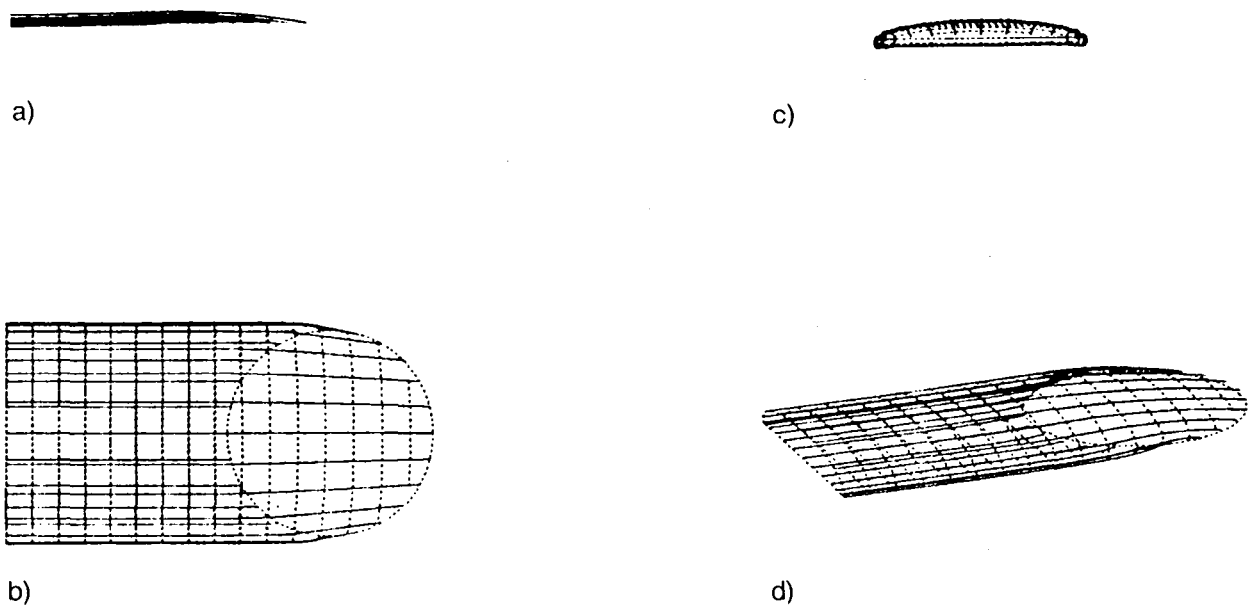

Figure 15 — Streamlines and Timelines for Fast Forward Flight Case

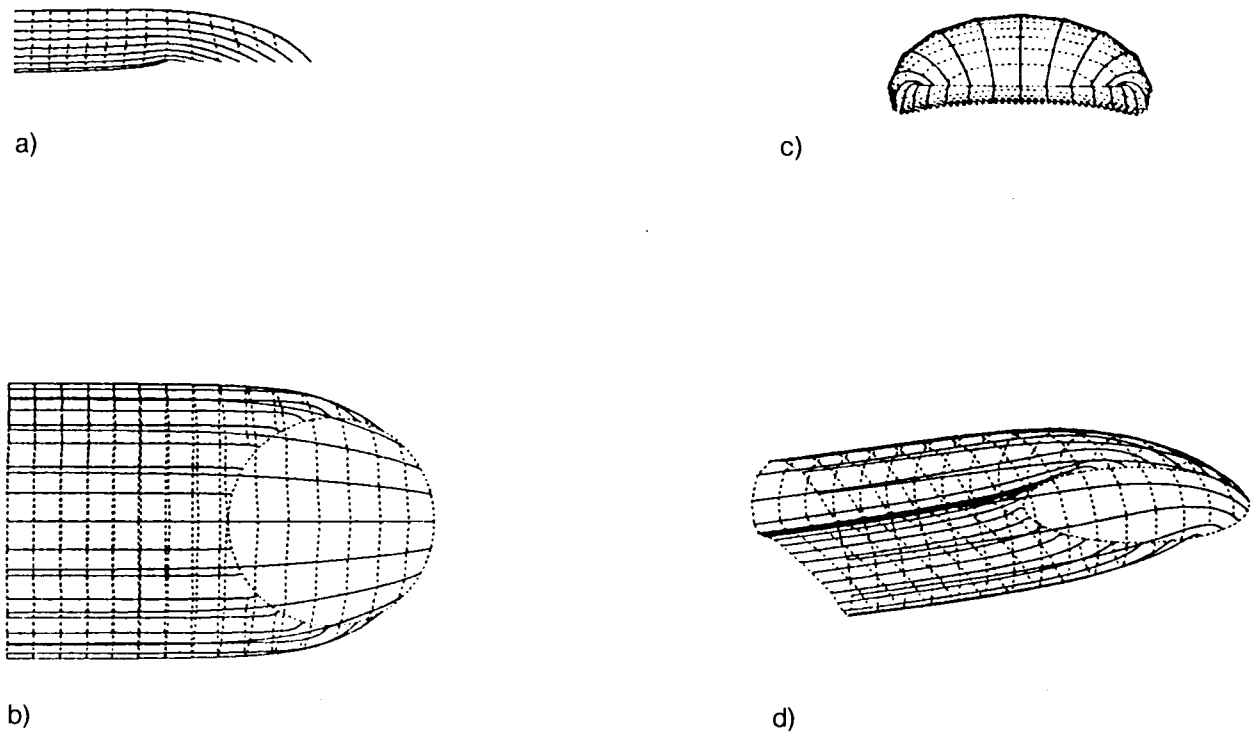

Figure 16 — Streamlines and Timelines for Slow Speed Forward Flight Case

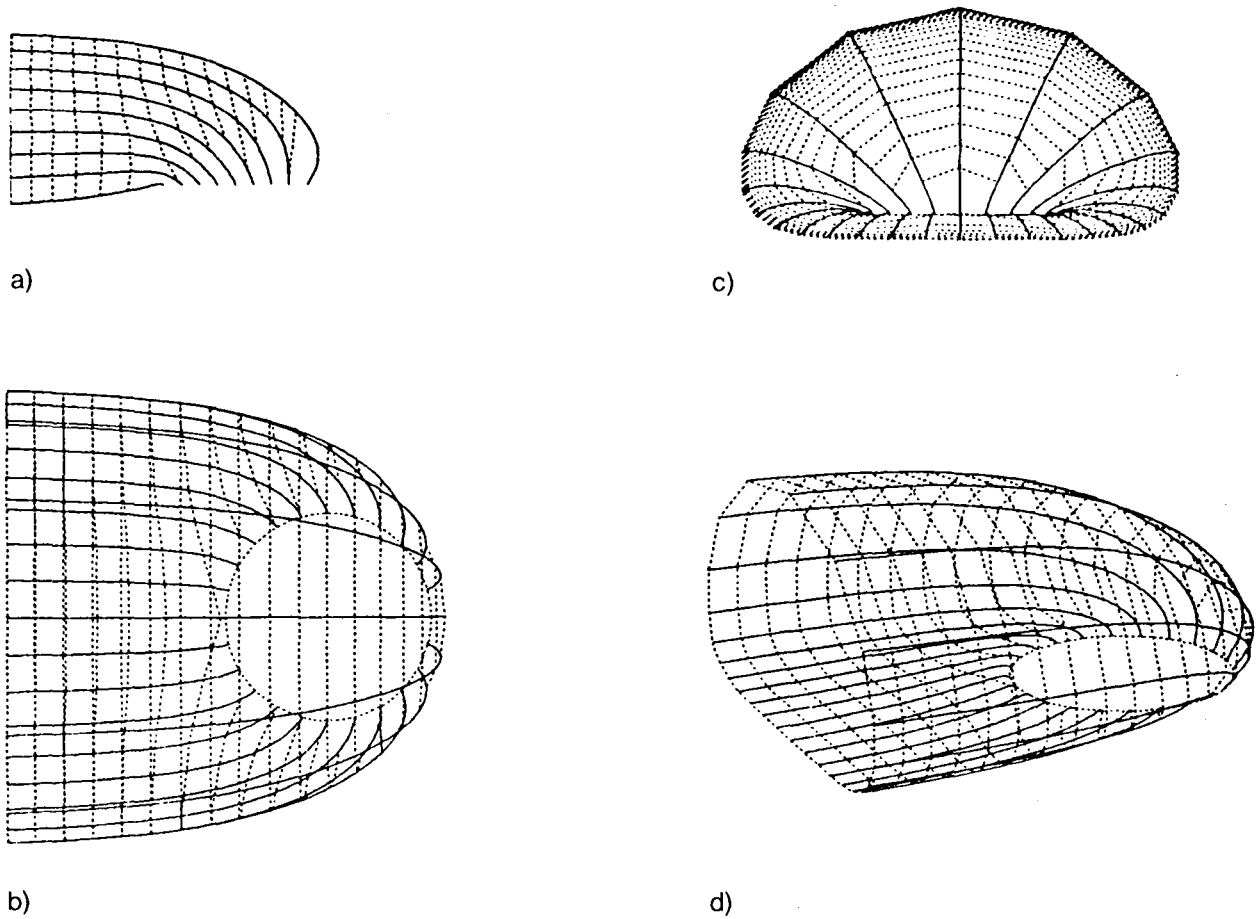

Figure 17 — Streamlines and Timelines for Hover Case

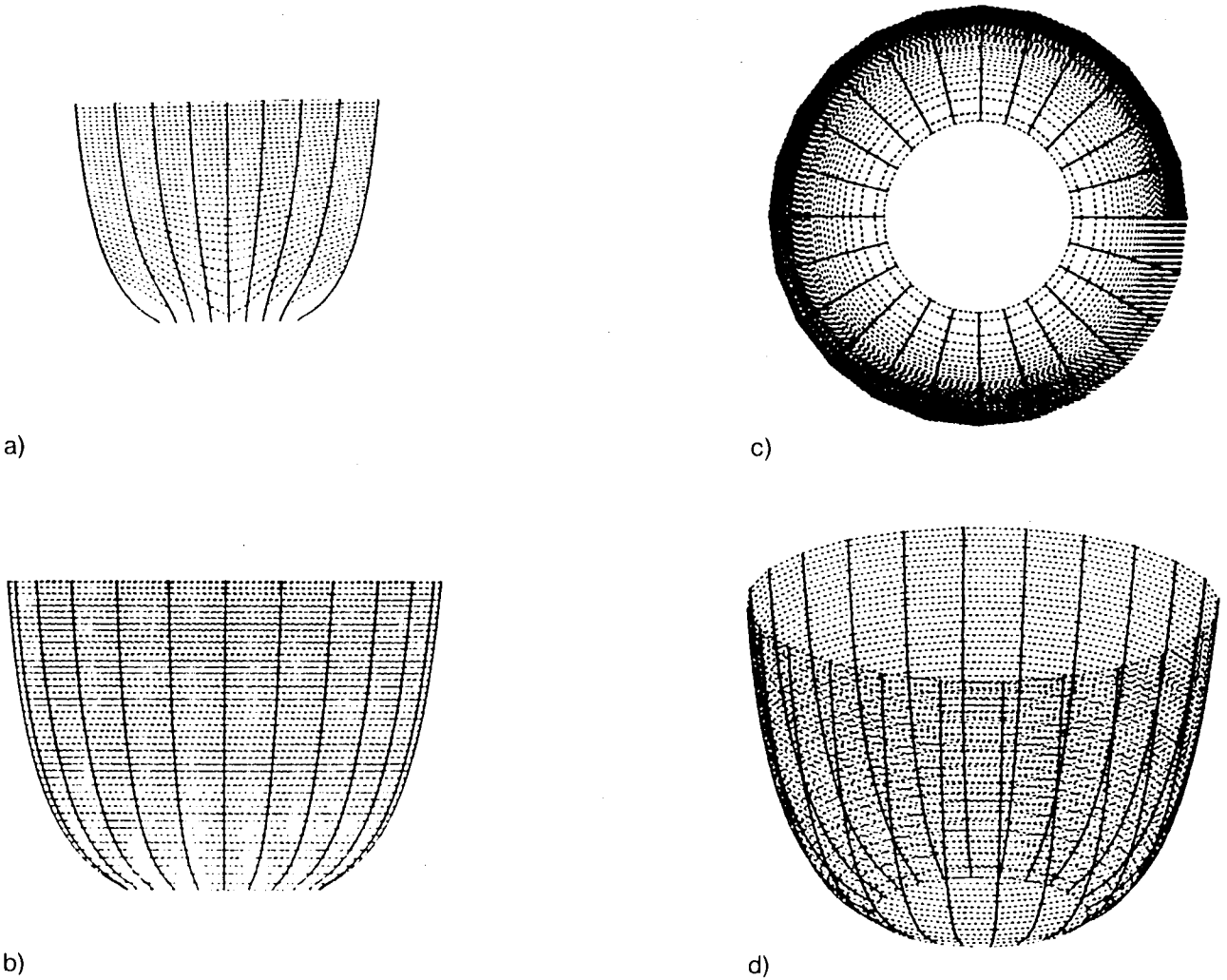

Figure 18 — Streamlines and Timelines for Low Speed Vertical Ascent Case

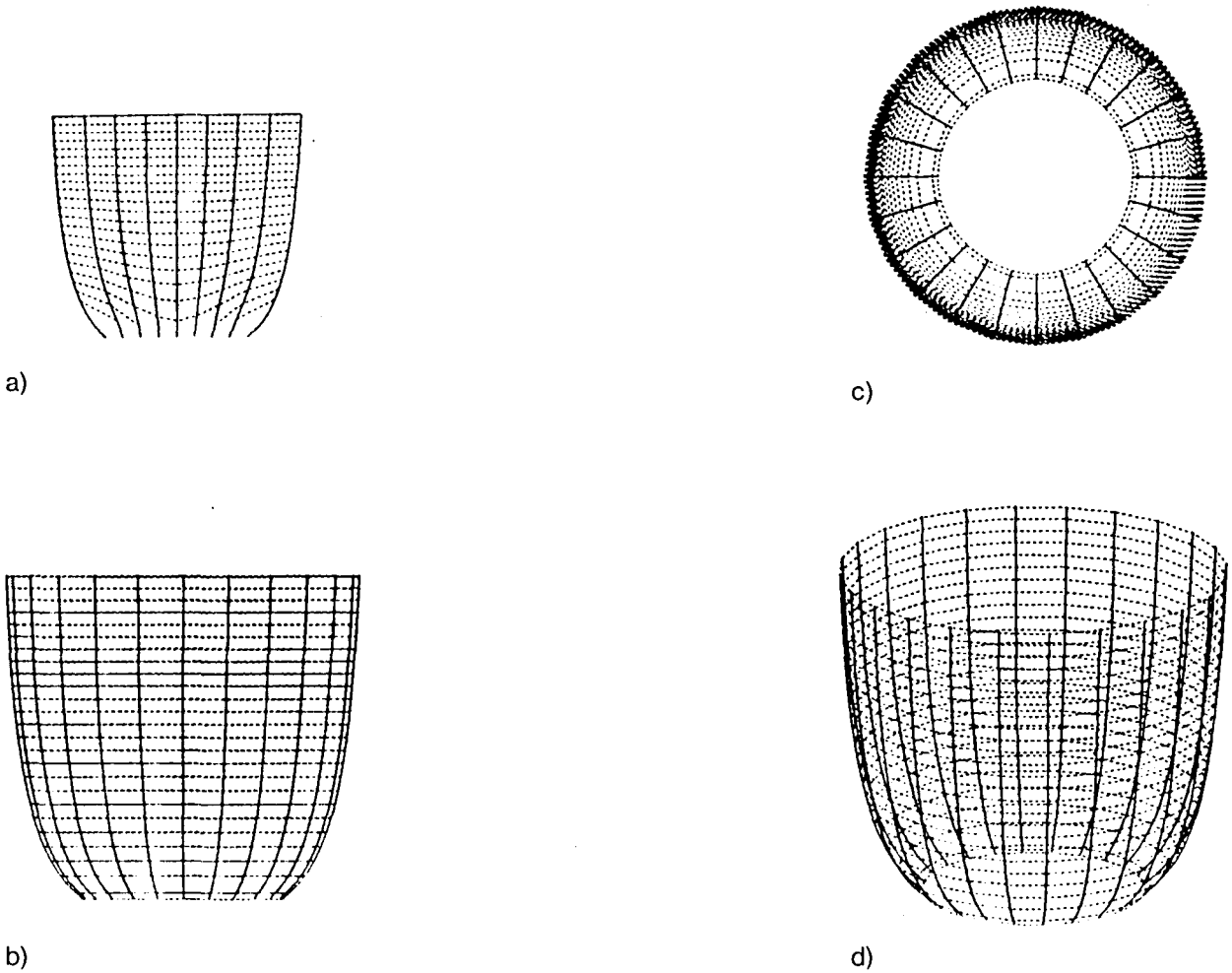

Figure 19 — Streamlines and Timelines for Mid Speed Vertical Ascent Case

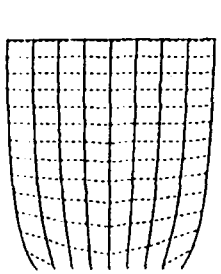

a)

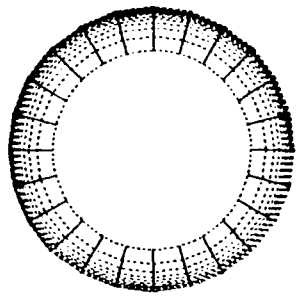

c)

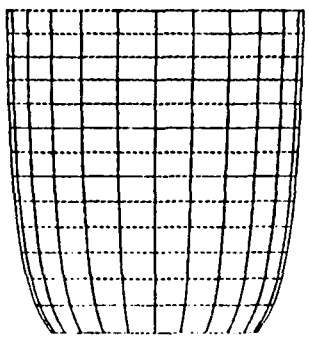

b)

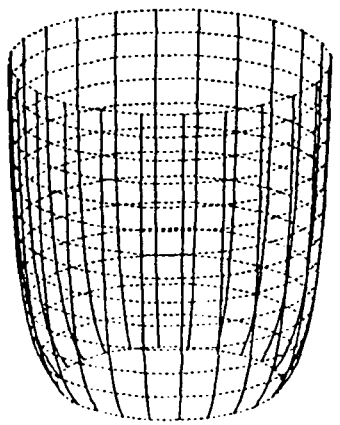

d)

Figure 20 — Streamlines and Timelines for High Speed Vertical Ascent Case

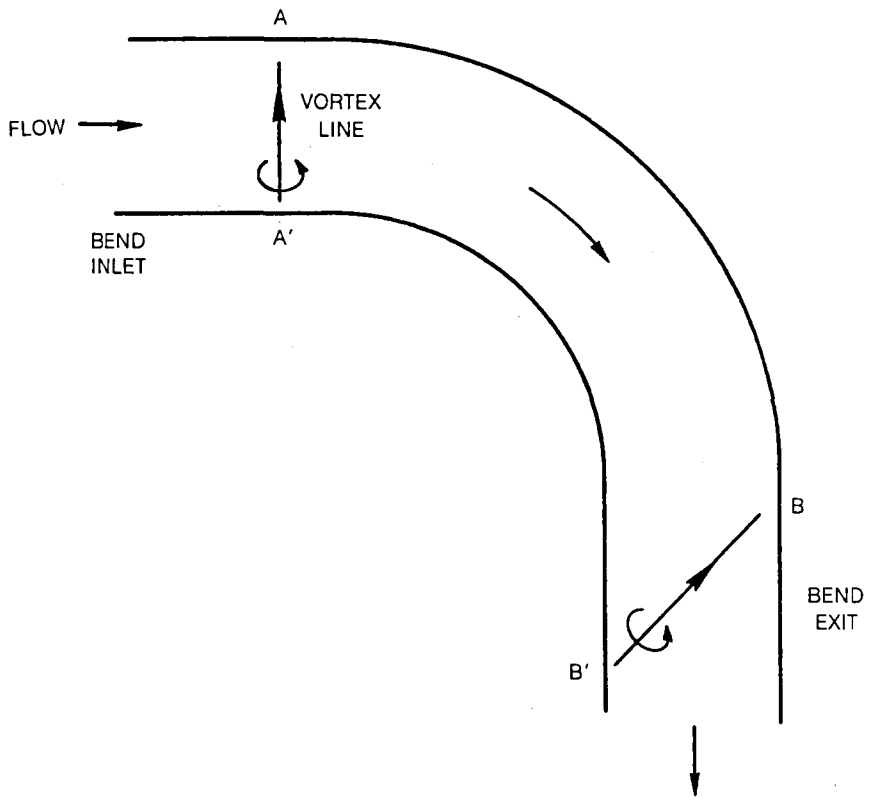

Figure 21 — Convection of Vortex Line in Constant Area Bend

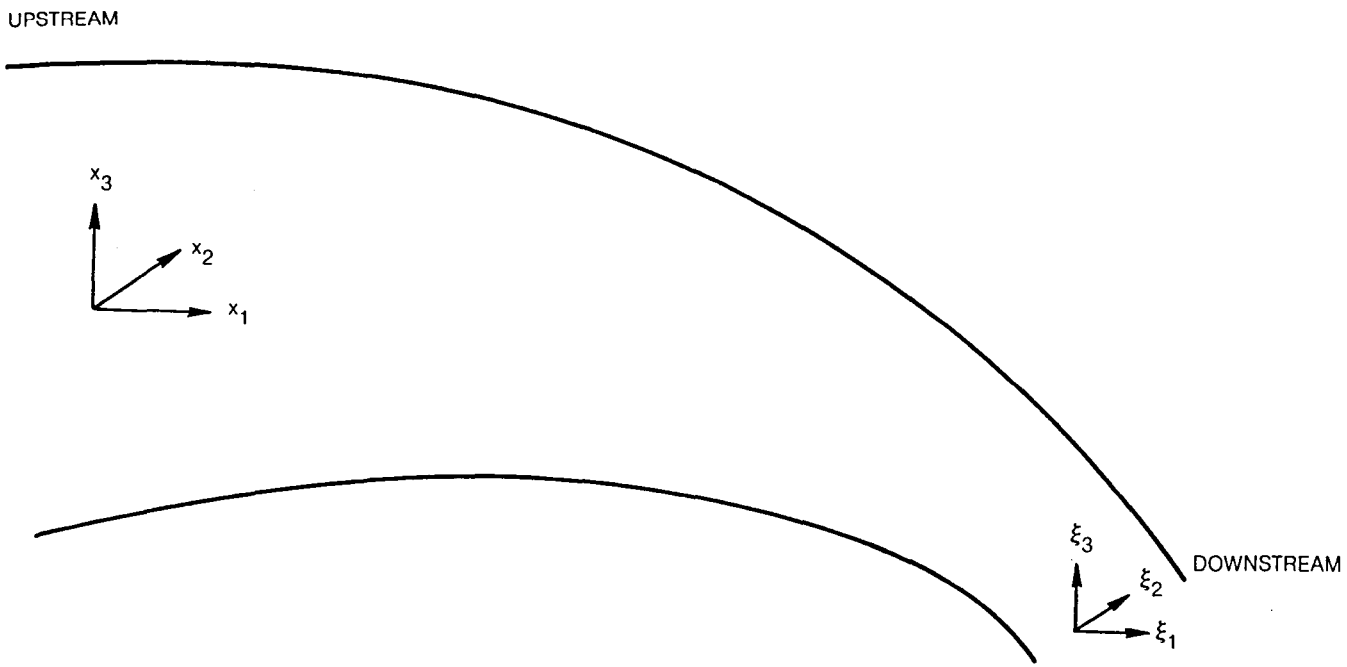

Figure 22 — Sketch Showing Upstream and Downstream Coordinate Systems in Contracting Stream

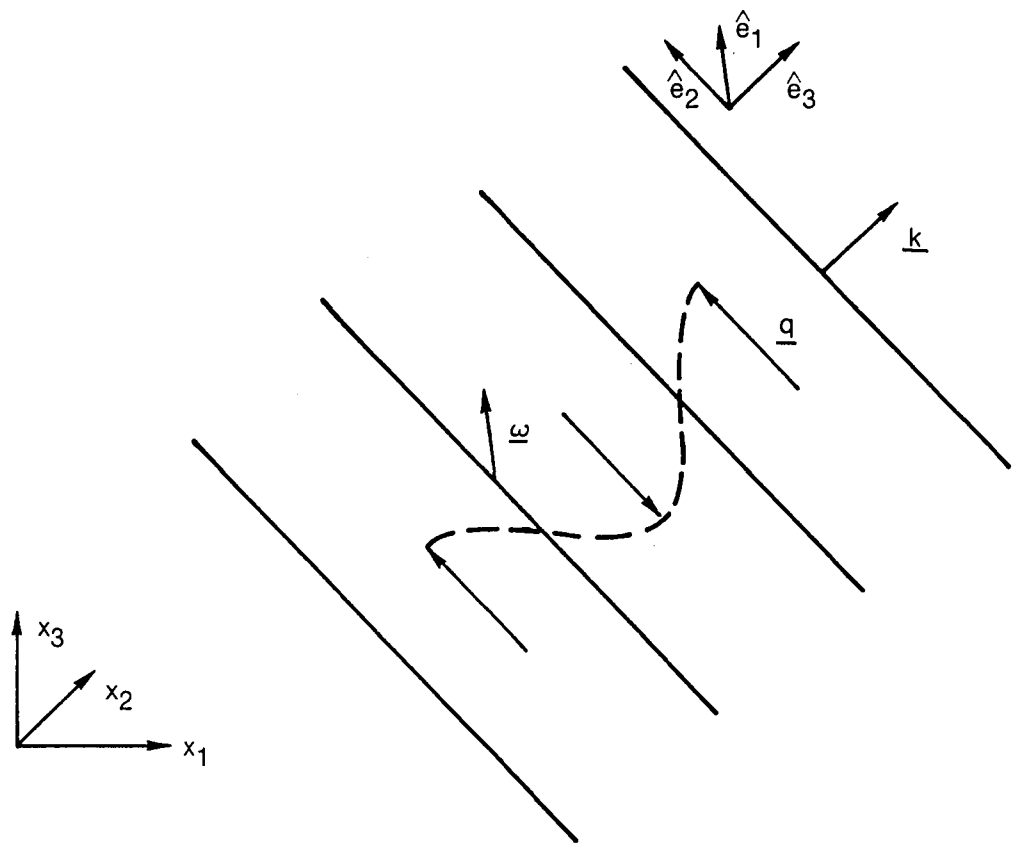

Figure 23 — Sinusoidal Velocity Variation for a Wave Vector Component of Turbulence. Also Shown are the $\hat{e}$ Vectors Introduced in Analytical Development

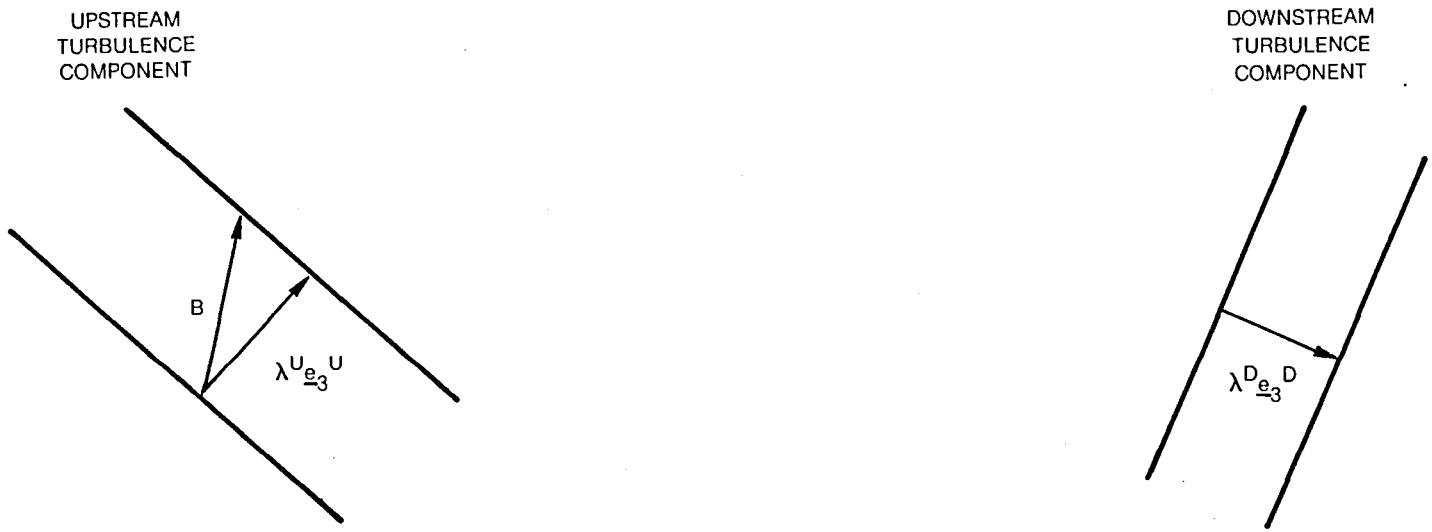

$\lambda^D \underline{e}_3{}^D$ TRANSFORMS TO A VECTOR $\underline{B}$ USING EQ. (11)

λ^U IS FOUND FROM RELATION $\lambda^U = \underline{B} \cdot \underline{e}_3{}^U$

Figure 24 — Relation of Upstream and Downstream Wavevectors

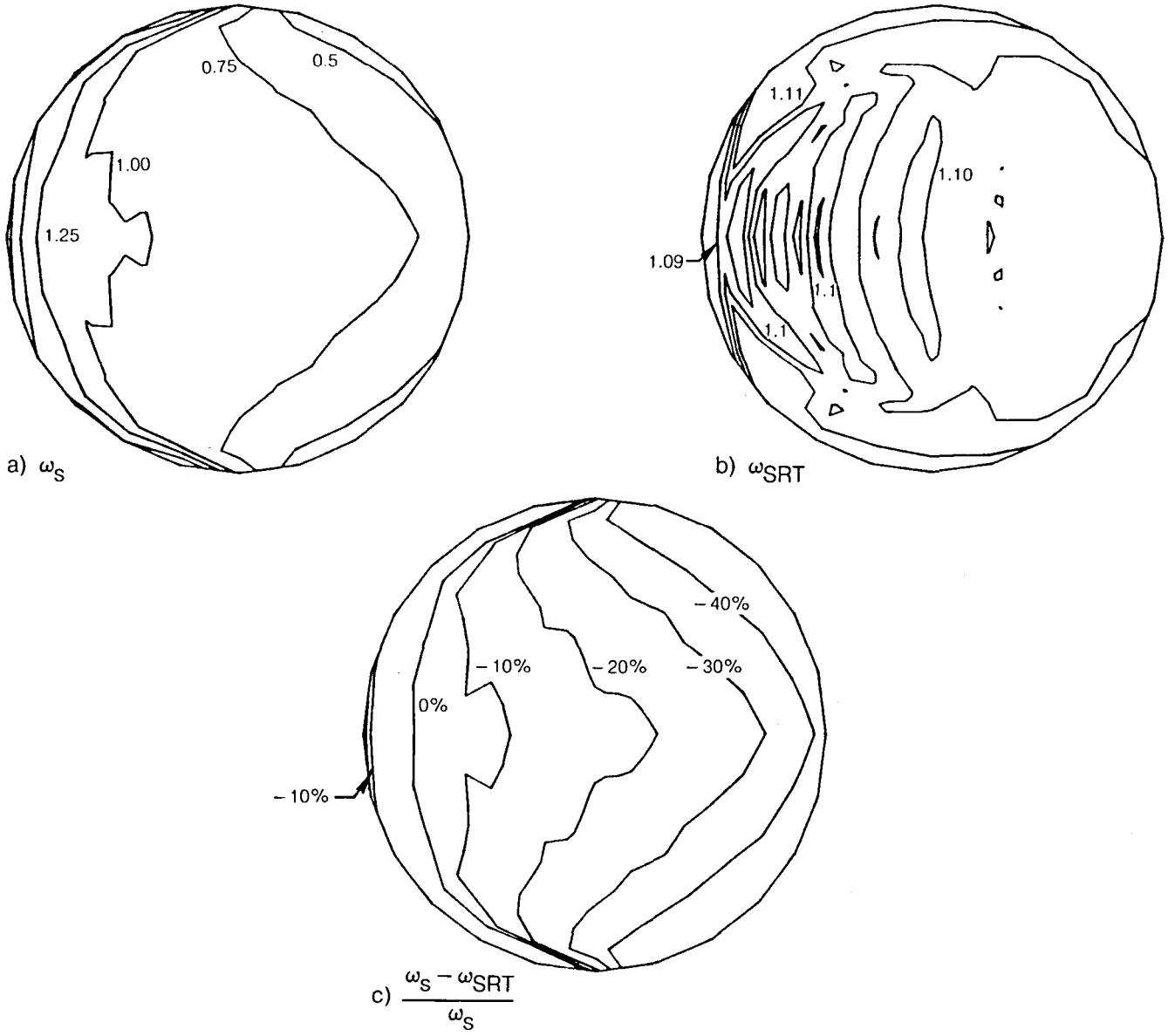

Figure 25 — Vorticity Contours for High Speed Forward Flight Case

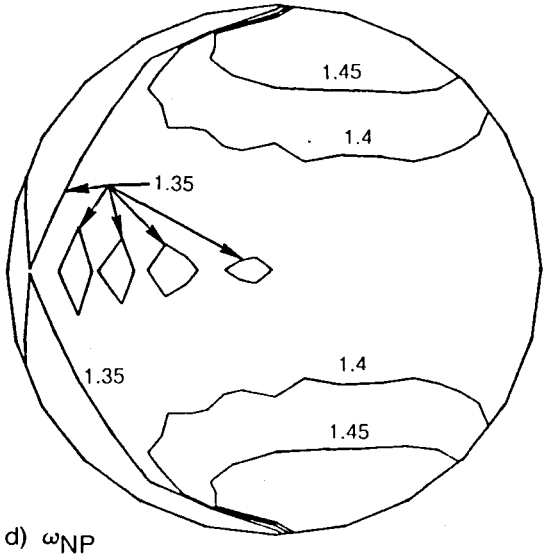

d) ω_{NP}

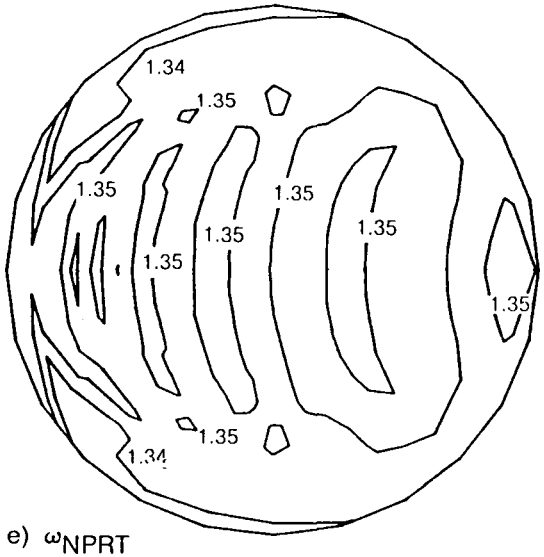

e) ω_{NPRT}

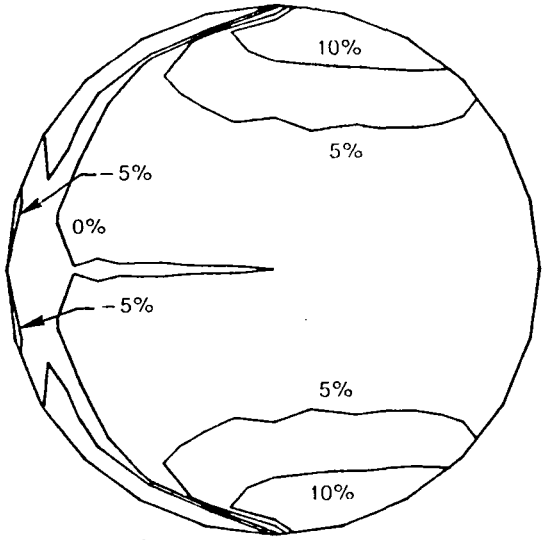

f) $\frac{\omega_{NP} - \omega_{NPRT}}{\omega_{NPRT}}$

Figure 25 — Continued

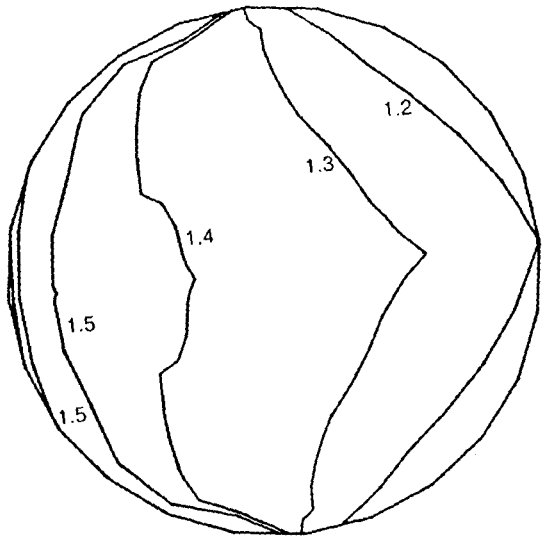

g) ω_R

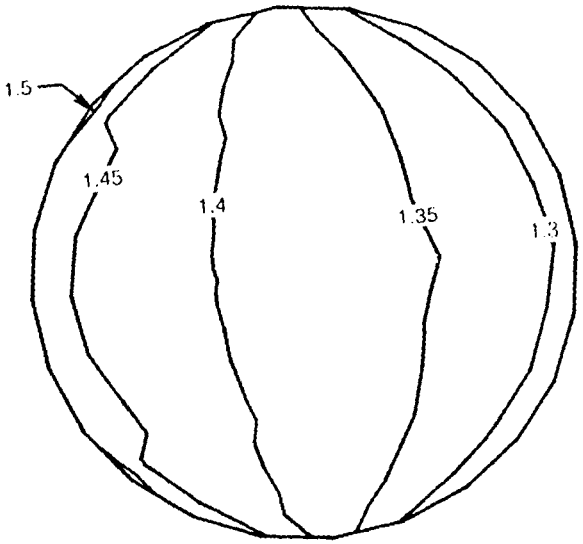

h) ω_{RRT}

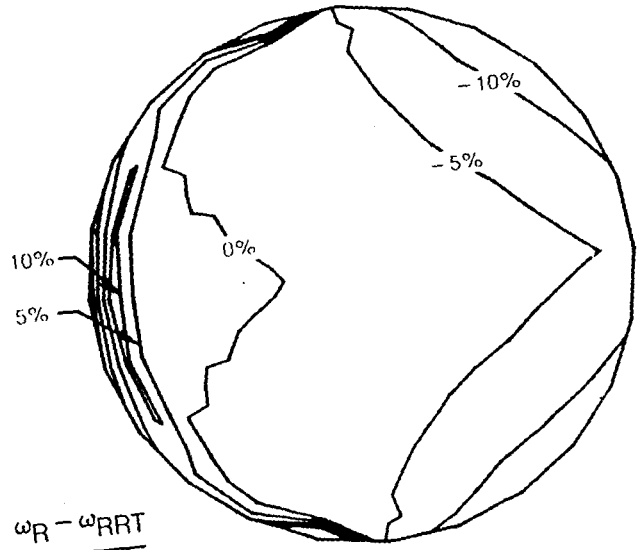

i) $\frac{\omega_R - \omega_{RRT}}{\omega_{RRT}}$

Figure 25 — Concluded

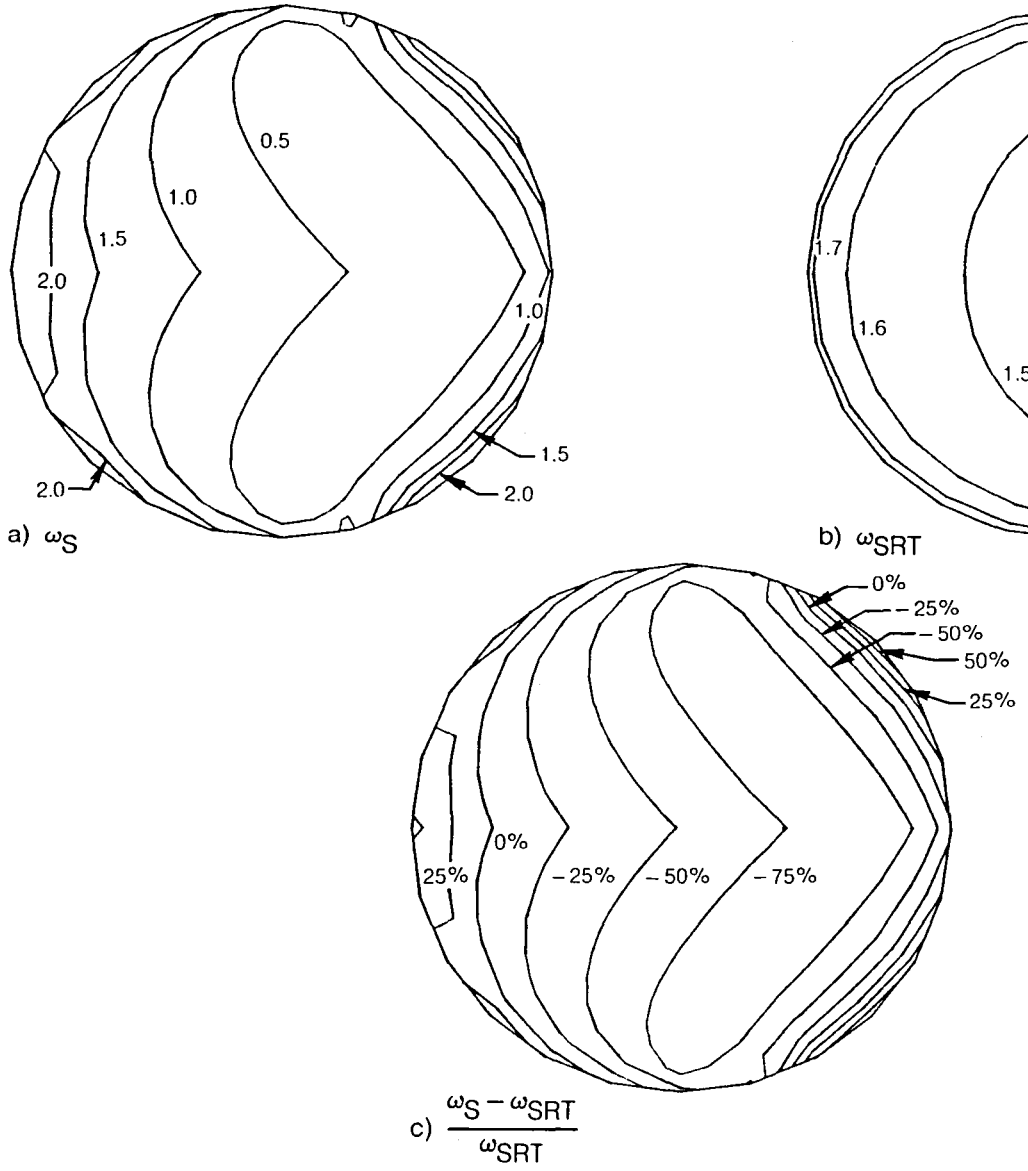

Figure 26 — Vorticity Contours for Low Speed Forward Flight Case

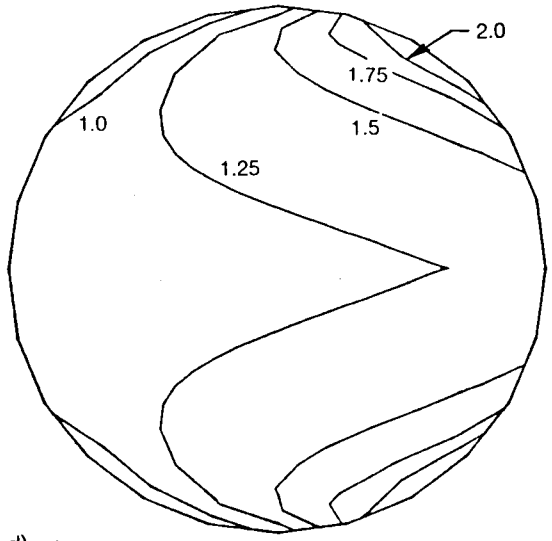

d) ω_{NP}

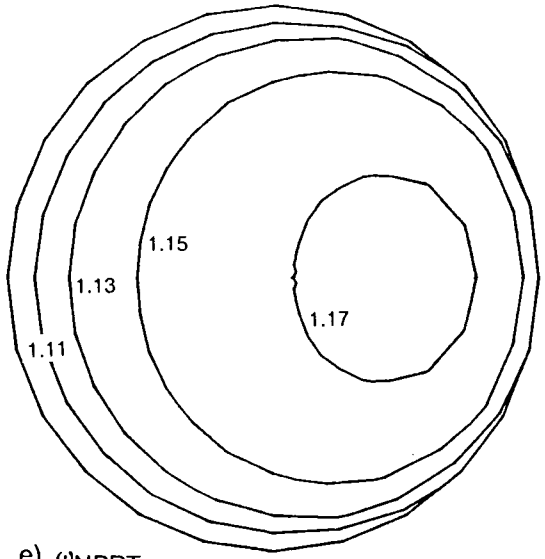

e) ω_{NPRT}

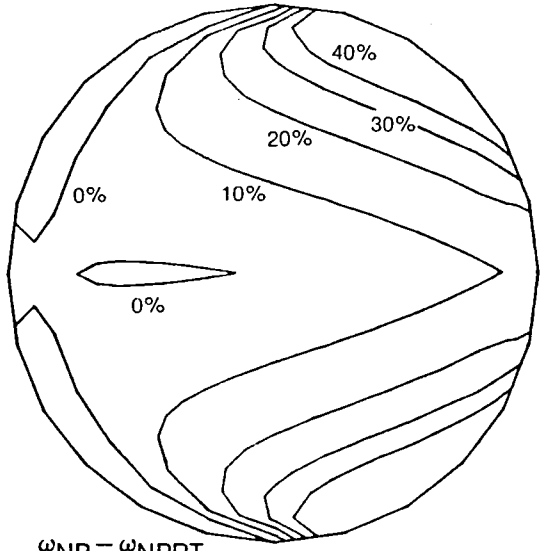

f) $\frac{\omega_{NP} - \omega_{NPRT}}{\omega_{NPRT}}$

Figure 26 — Continued

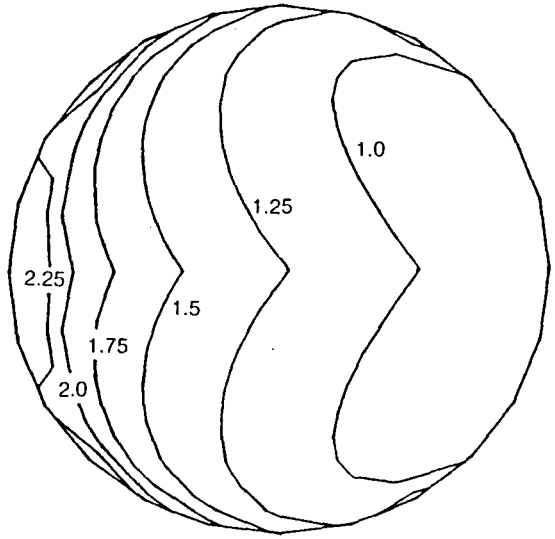

g) ω_R

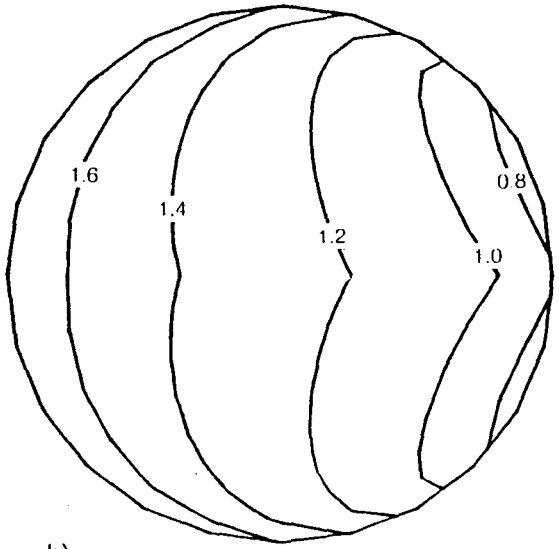

h) ω_{RRT}

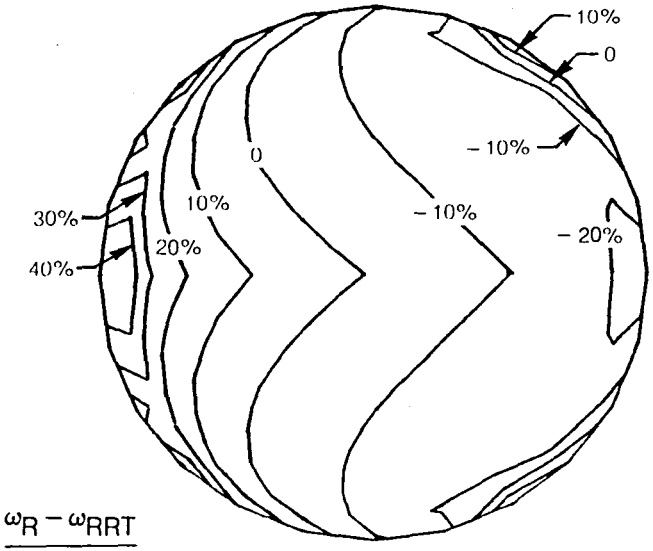

i) $\frac{\omega_R - \omega_{RRT}}{\omega_{RRT}}$

Figure 26 — Concluded

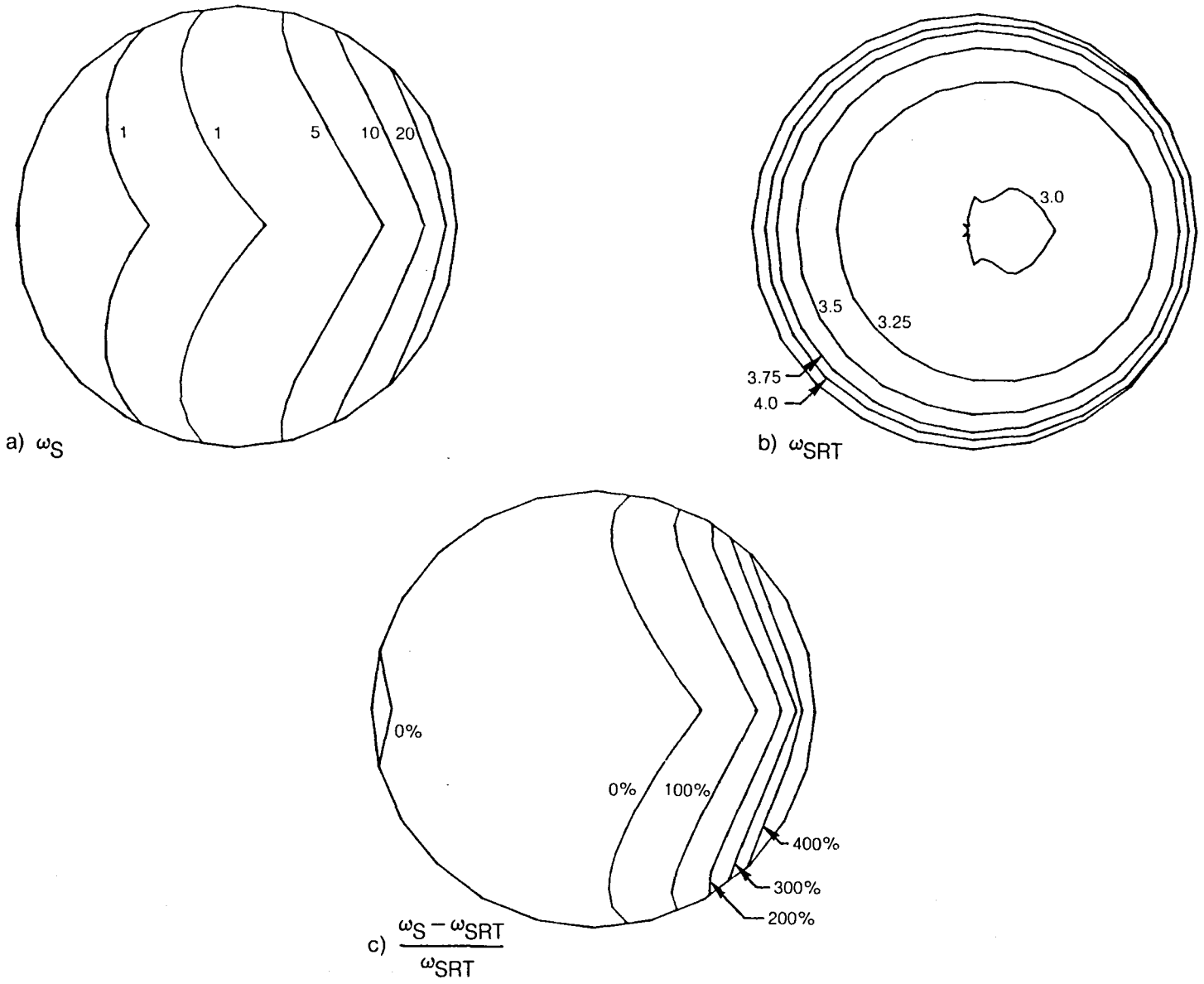

Figure 27 — Vorticity Contours for Hover Case

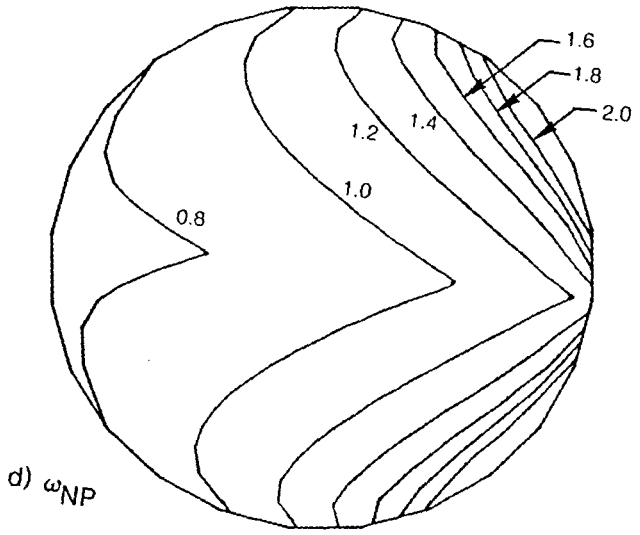

d) ω_{NP}

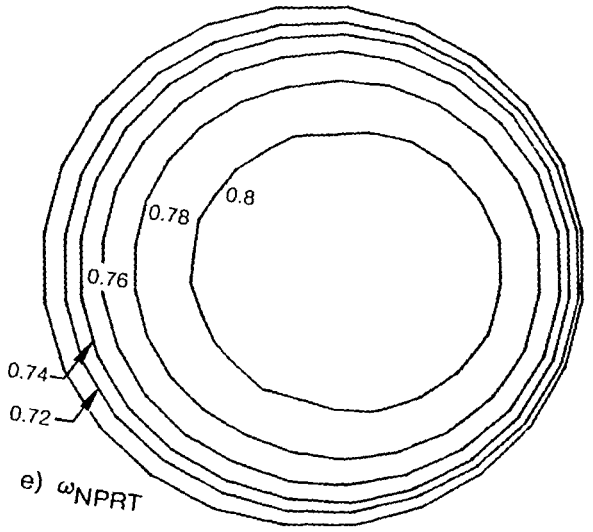

e) ω_{NPRT}

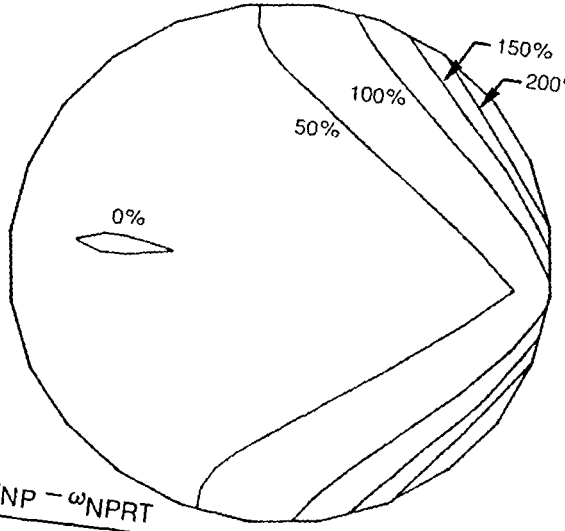

f) $\frac{\omega_{NP} - \omega_{NPRT}}{\omega_{NPRT}}$

Figure 27 — Continued

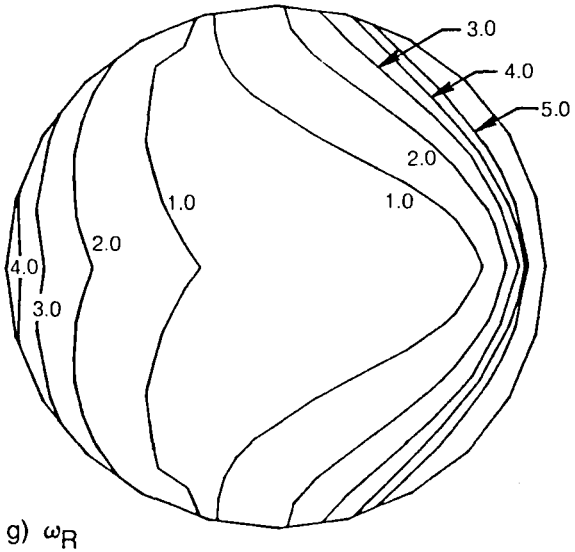

g) ω_R

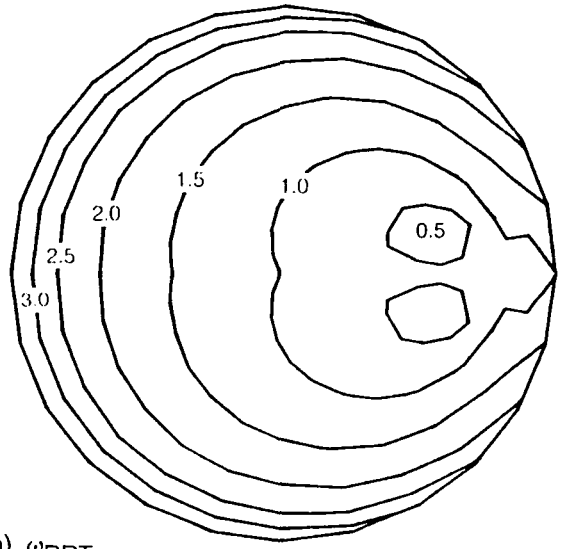

h) ω_{RRT}

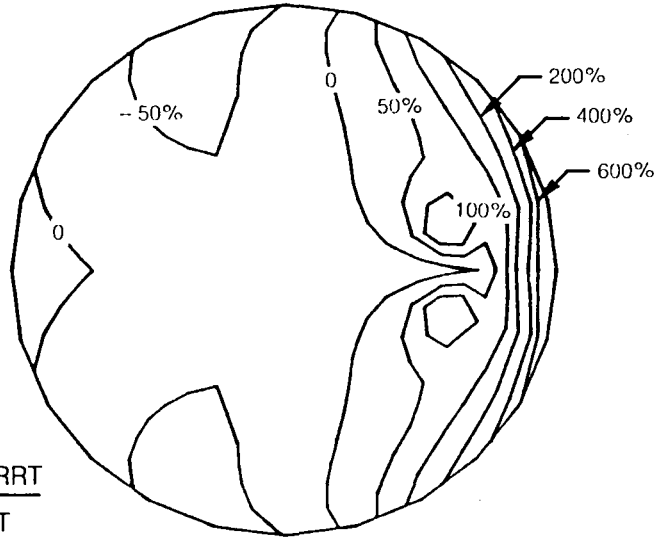

i) $\frac{\omega_R - \omega_{RRT}}{\omega_{RRT}}$

Figure 27 — Concluded

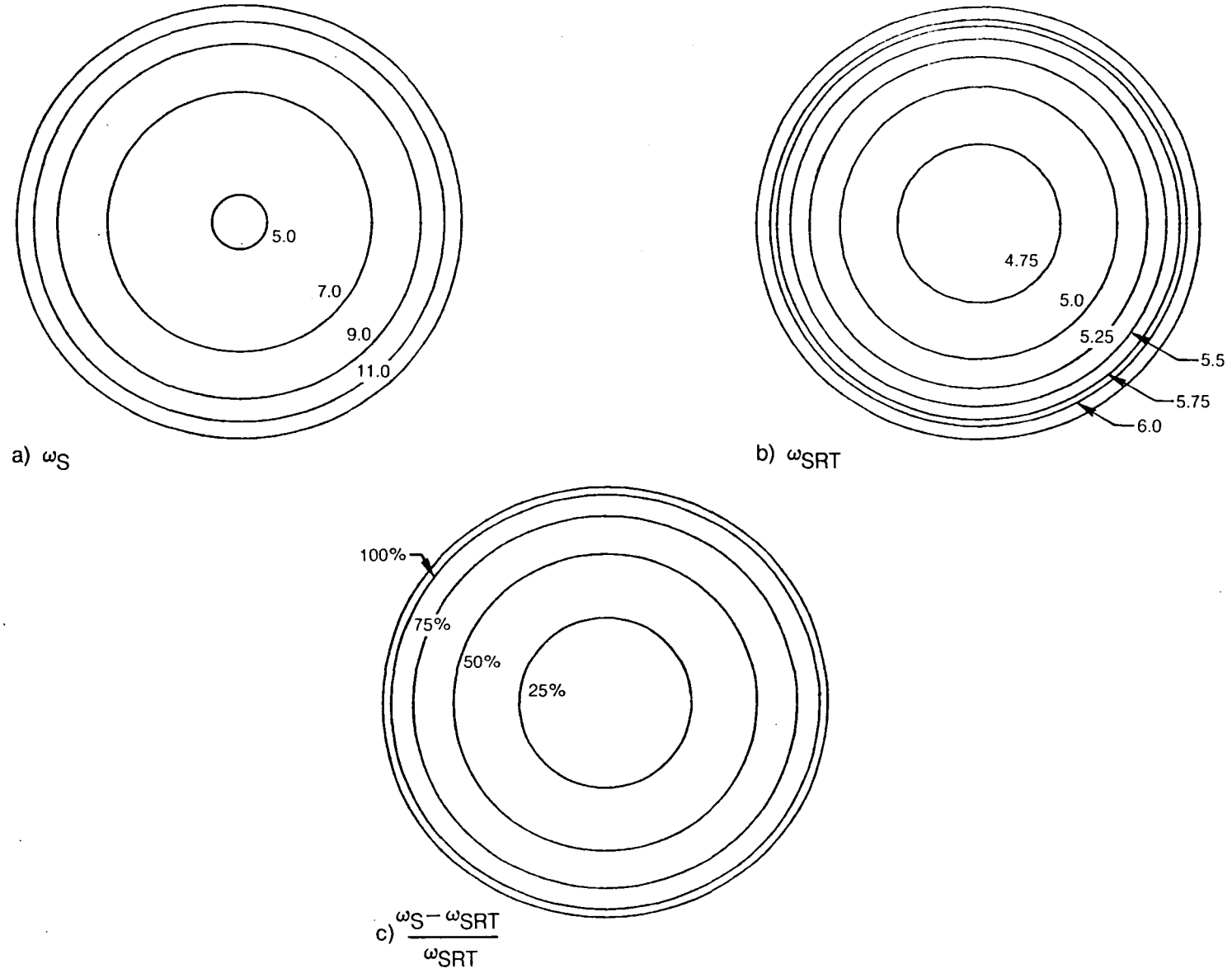

Figure 28 — Vorticity Contours for Low Speed Vertical Ascent Case

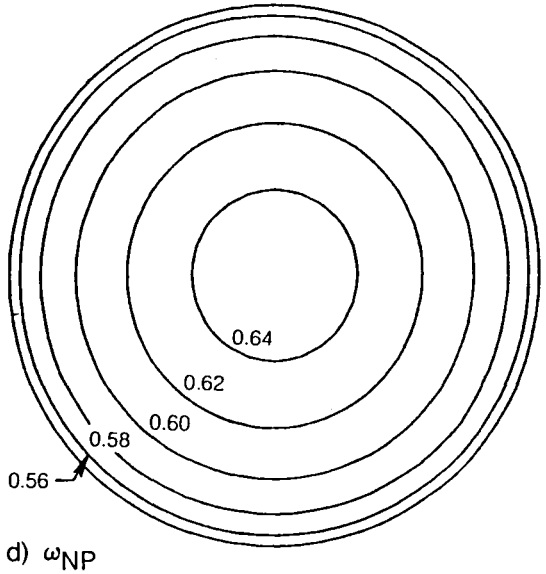

d) ω_{NP}

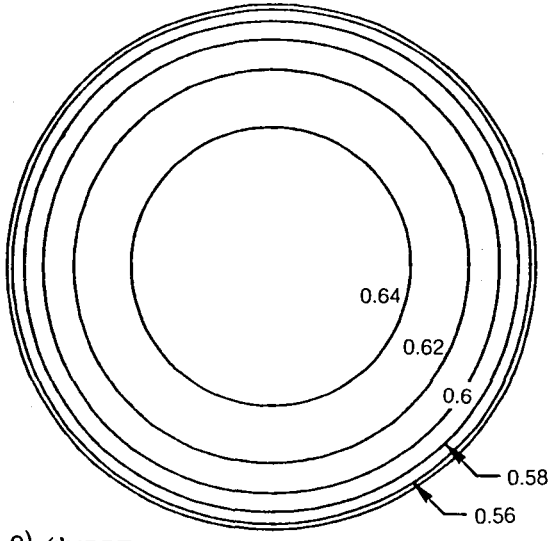

e) ω_{NPRT}

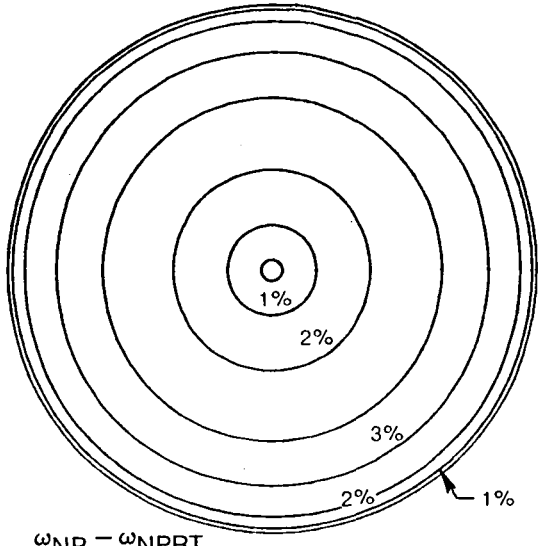

f) $\frac{\omega_{NP} - \omega_{NPRT}}{\omega_{NPRT}}$

Figure 28 — Continued

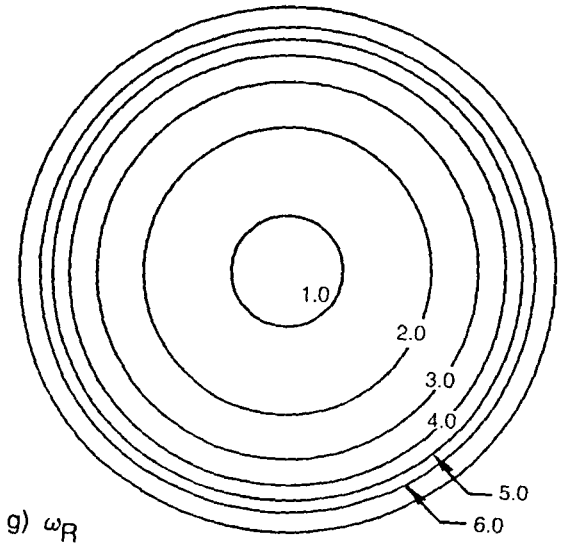

g) ω_R

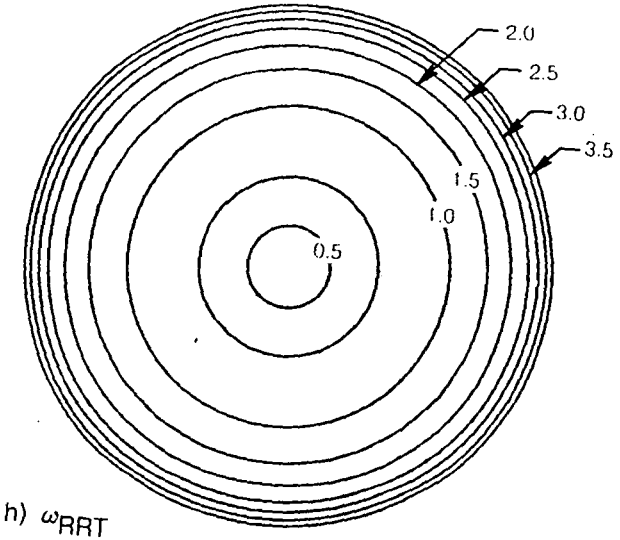

h) ω_{RRT}

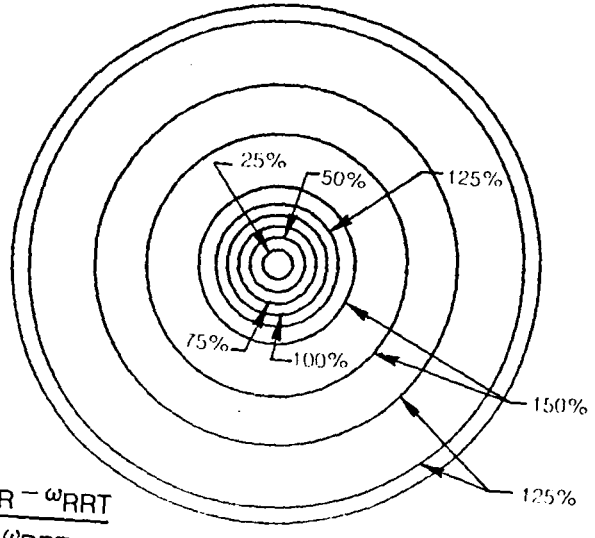

i) $\frac{\omega_R - \omega_{RRT}}{\omega_{RRT}}$

Figure 28 — Concluded

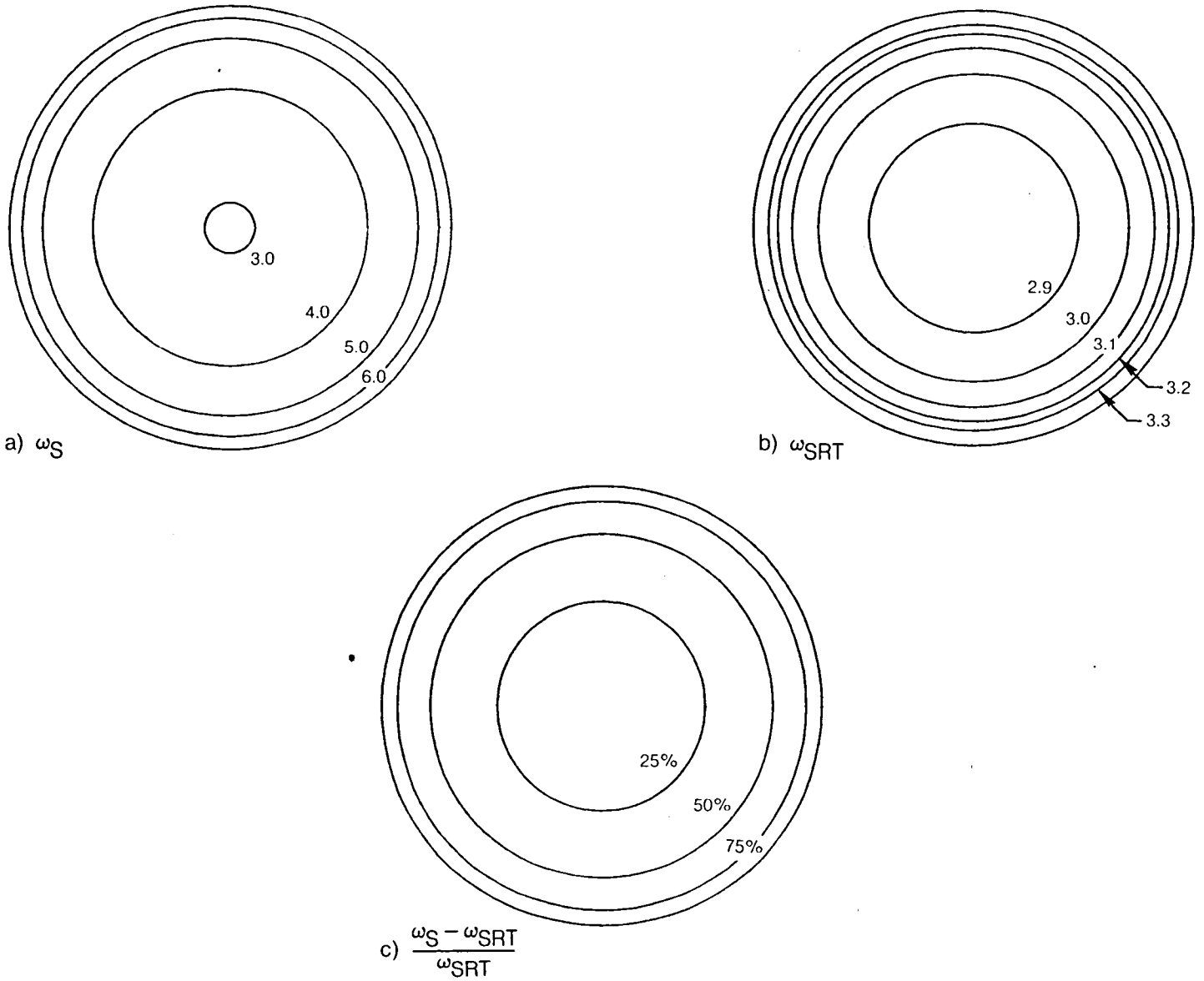

Figure 29 — Vorticity Contours for Mid Speed Vertical Ascent Case

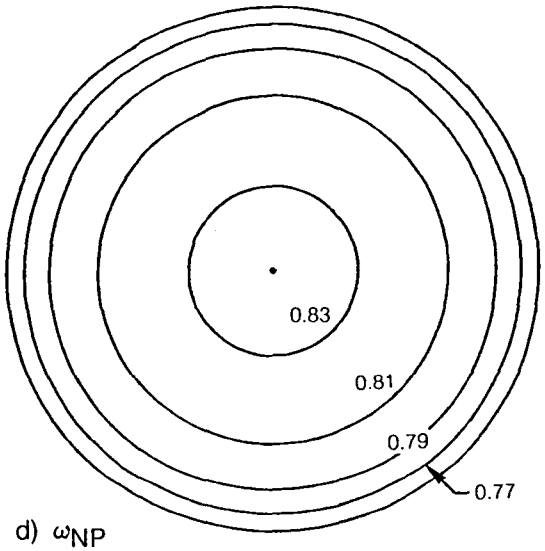

d) ω_{NP}

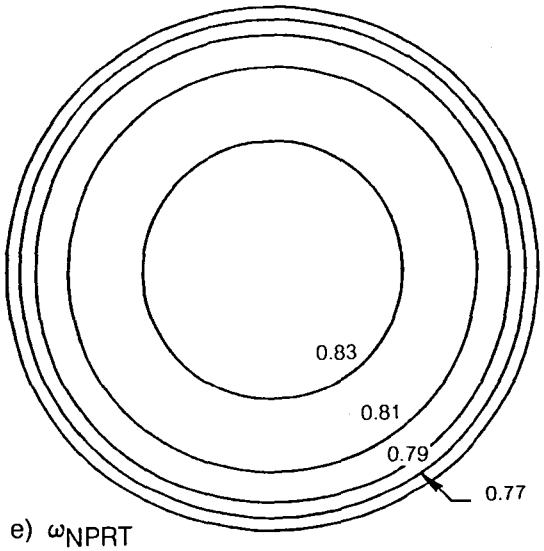

e) ω_{NPRT}

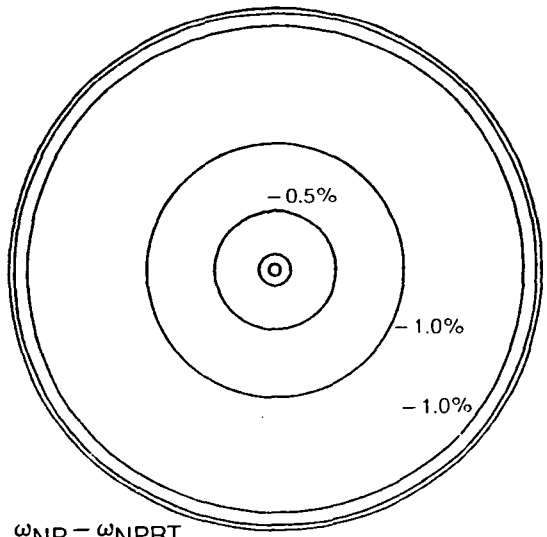

f) $\frac{\omega_{NP} - \omega_{NPRT}}{\omega_{NPRT}}$

Figure 29 — Continued

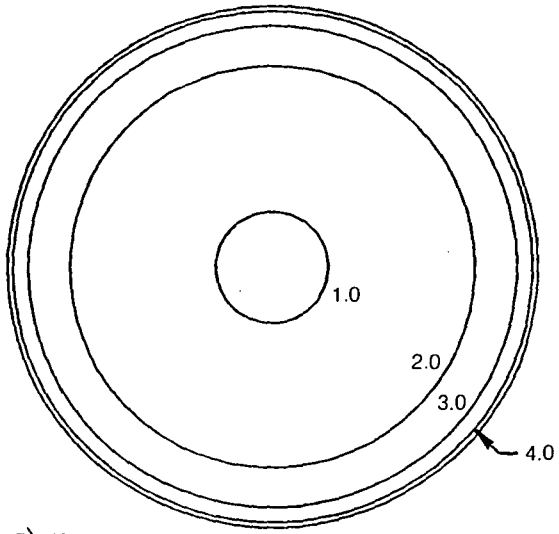

g) ω_R

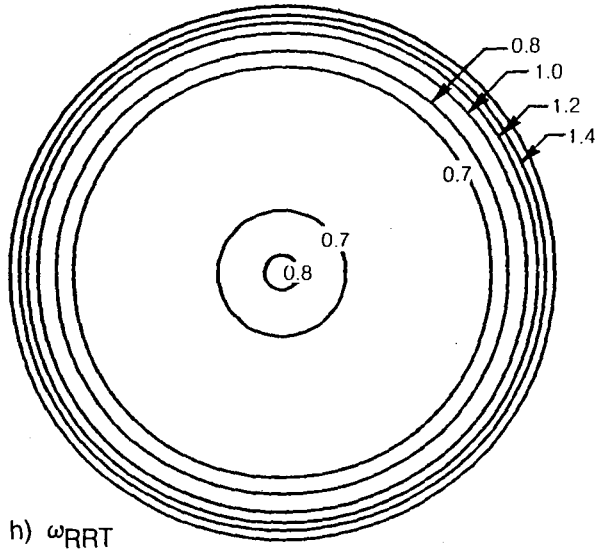

h) ω_{RRT}

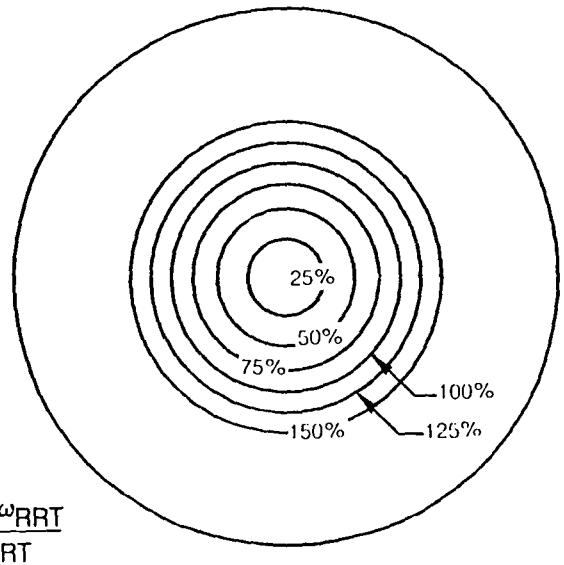

i) $\frac{\omega_R - \omega_{RRT}}{\omega_{RRT}}$

Figure 29 — Concluded

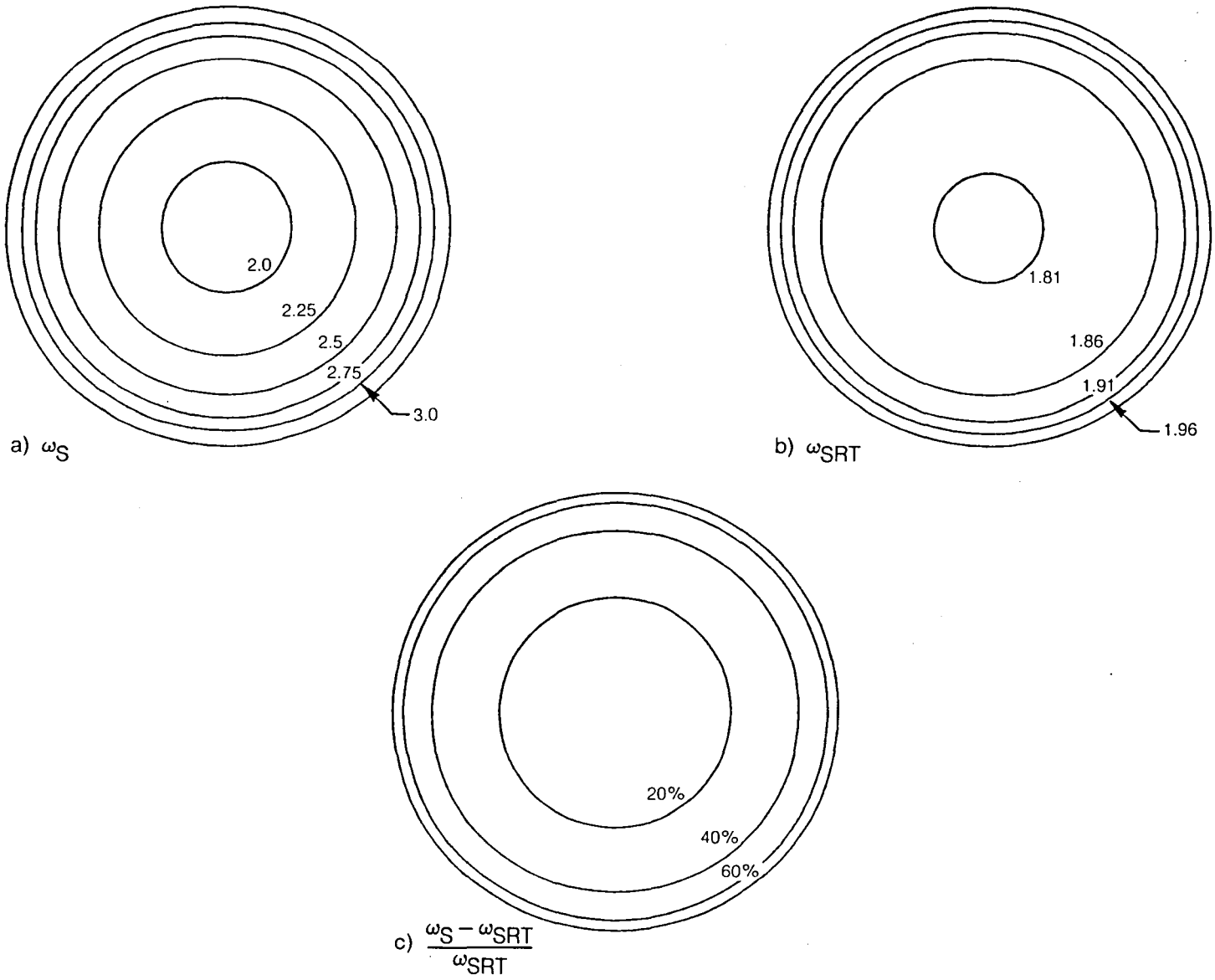

Figure 30 — Vorticity Contours for High Speed Vertical Ascent Case

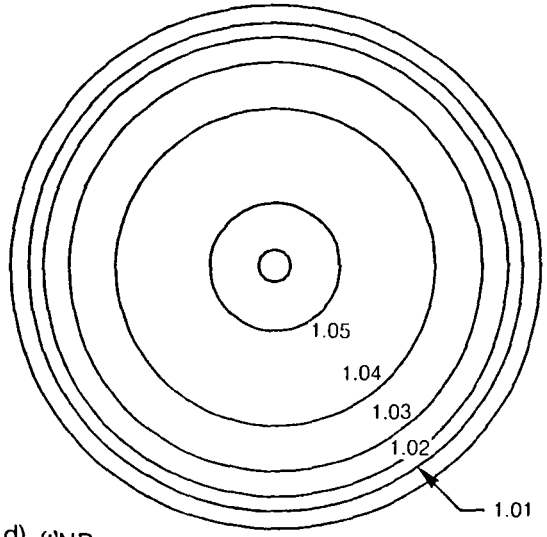

d) ω_{NP}

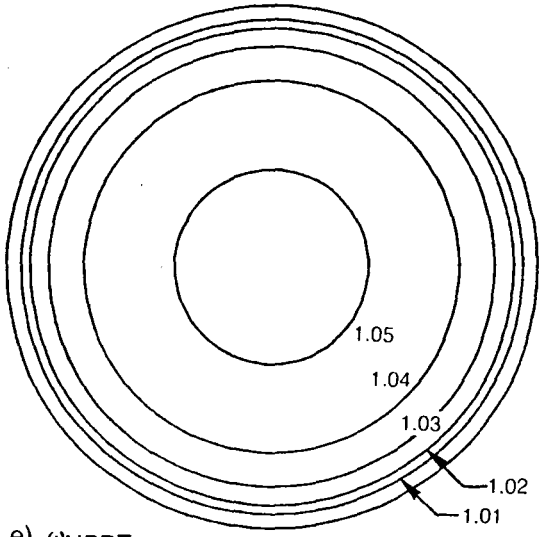

e) ω_{NPRT}

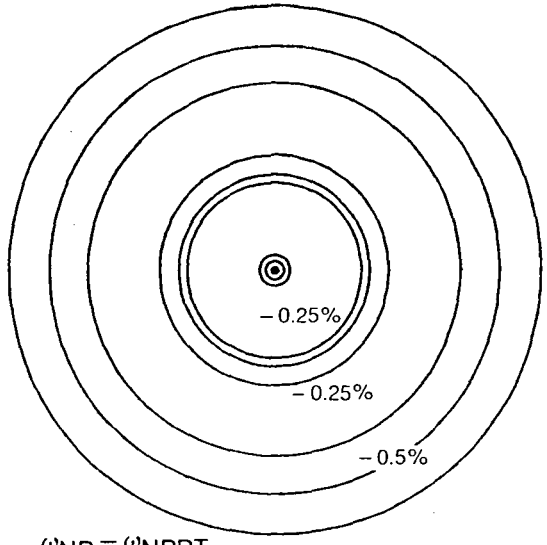

f) $\frac{\omega_{NP} - \omega_{NPRT}}{\omega_{NPRT}}$

Figure 30 — Continued

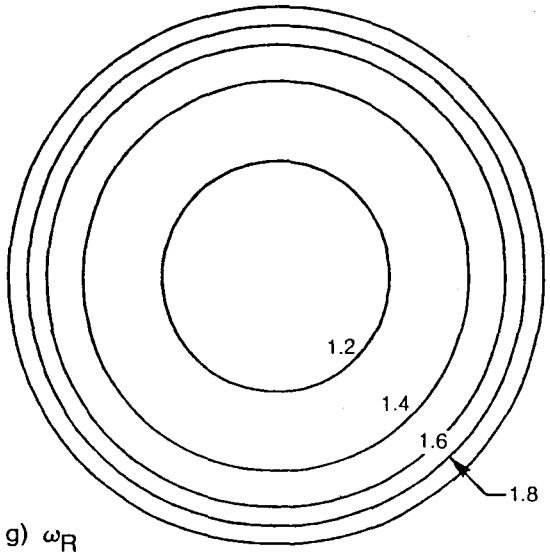

g) ω_R

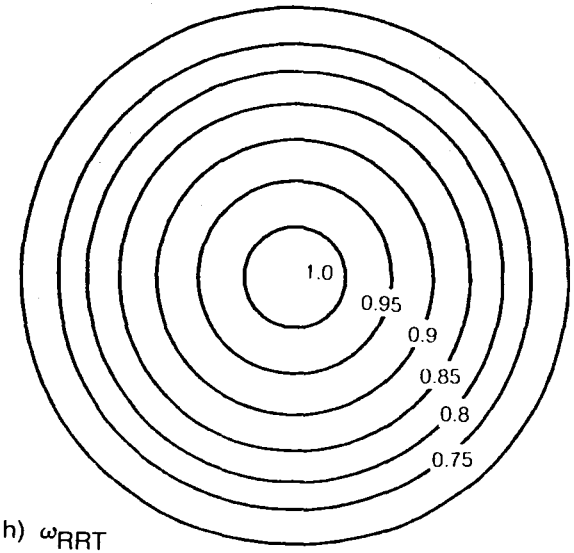

h) ω_{RRT}

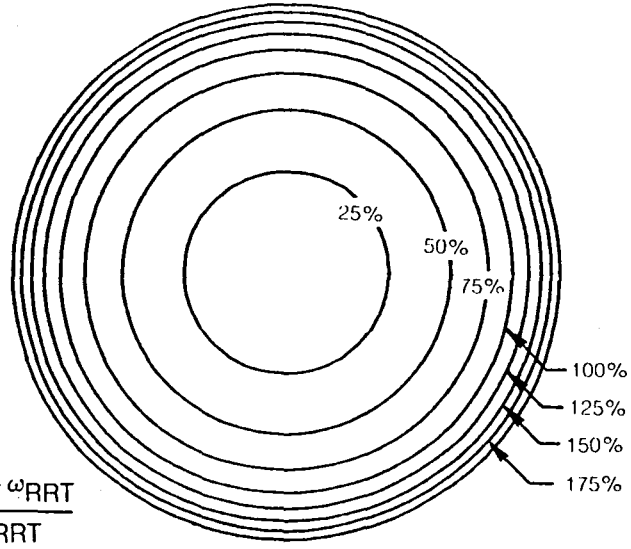

i) $\frac{\omega_R - \omega_{RRT}}{\omega_{RRT}}$

Figure 30 — Concluded

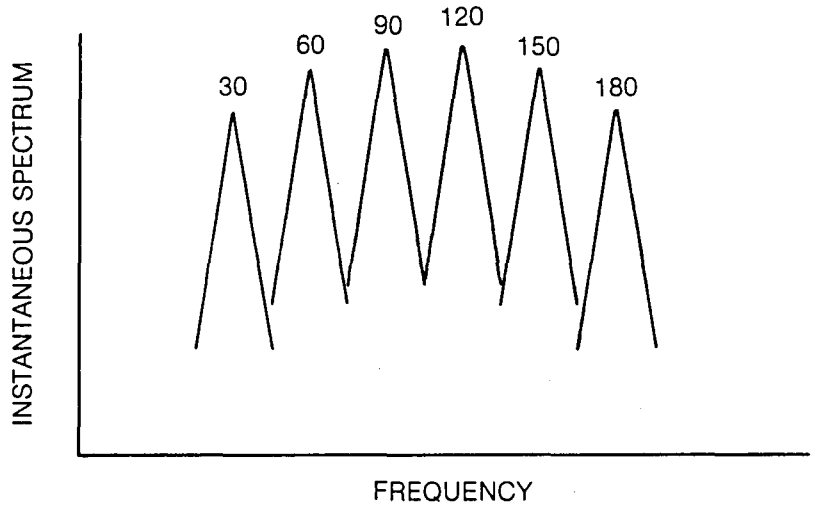

Figure 31 — Sketch of Instantaneous Spectrum for Various Azimuthal Angles

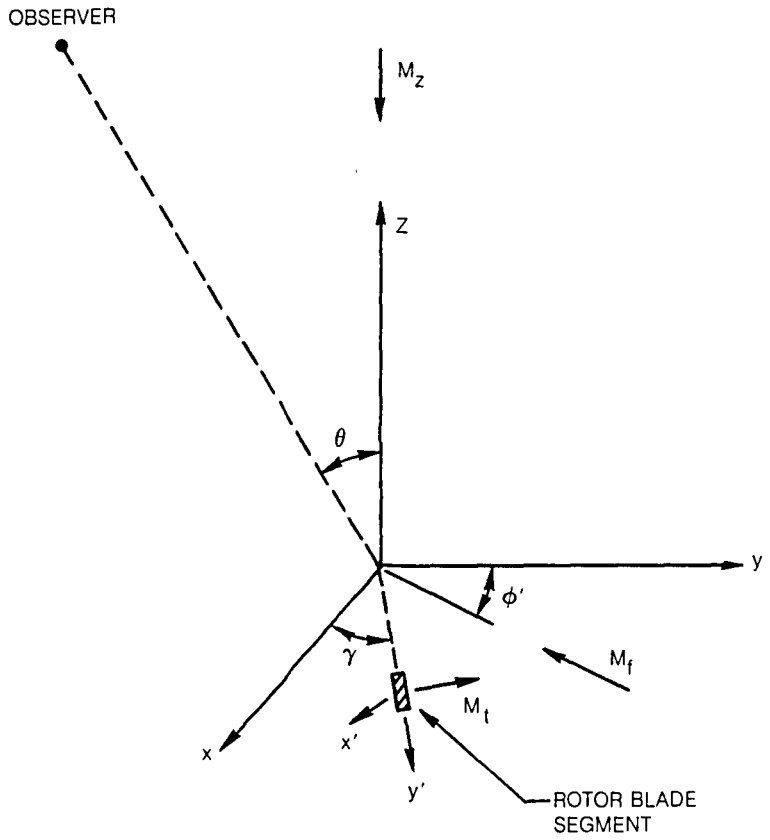

Figure 32 — Rotor Blade Segment Moving in Forward Flight

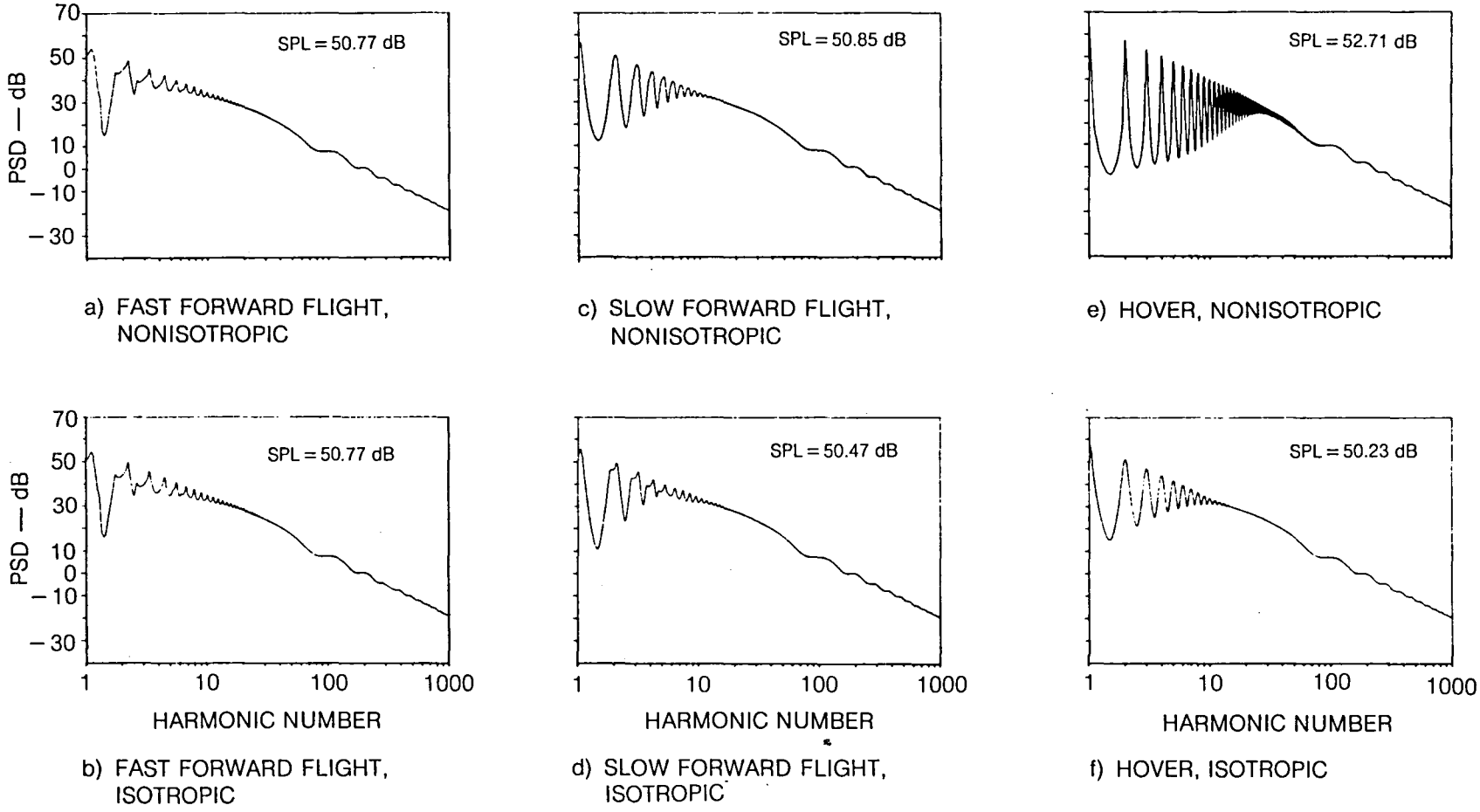

Figure 33 — Spectrum Dependences on Isotropic vs Nonisotropic Turbulence, L = ∞, G = 5.1 m/s, Z = 122 m

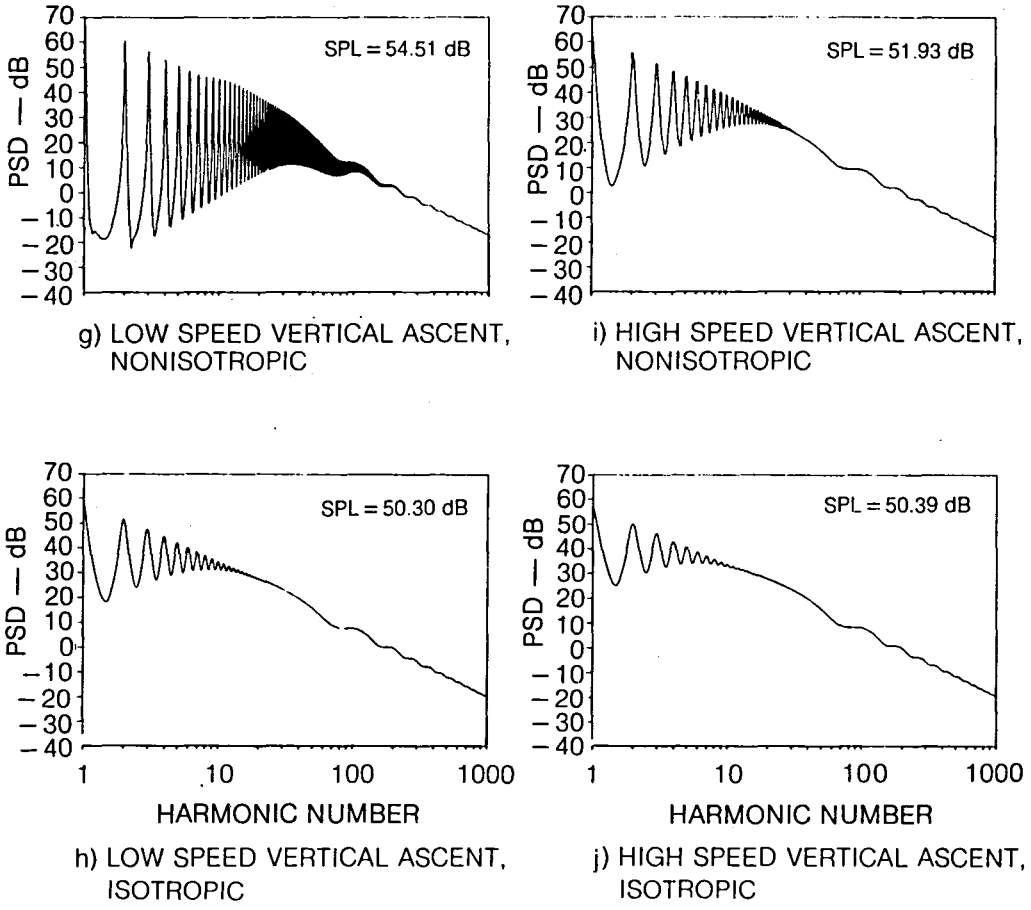

g) LOW SPEED VERTICAL ASCENT, NONISOTROPIC

i) HIGH SPEED VERTICAL ASCENT, NONISOTROPIC

h) LOW SPEED VERTICAL ASCENT, ISOTROPIC

j) HIGH SPEED VERTICAL ASCENT, ISOTROPIC

Figure 33 — Concluded

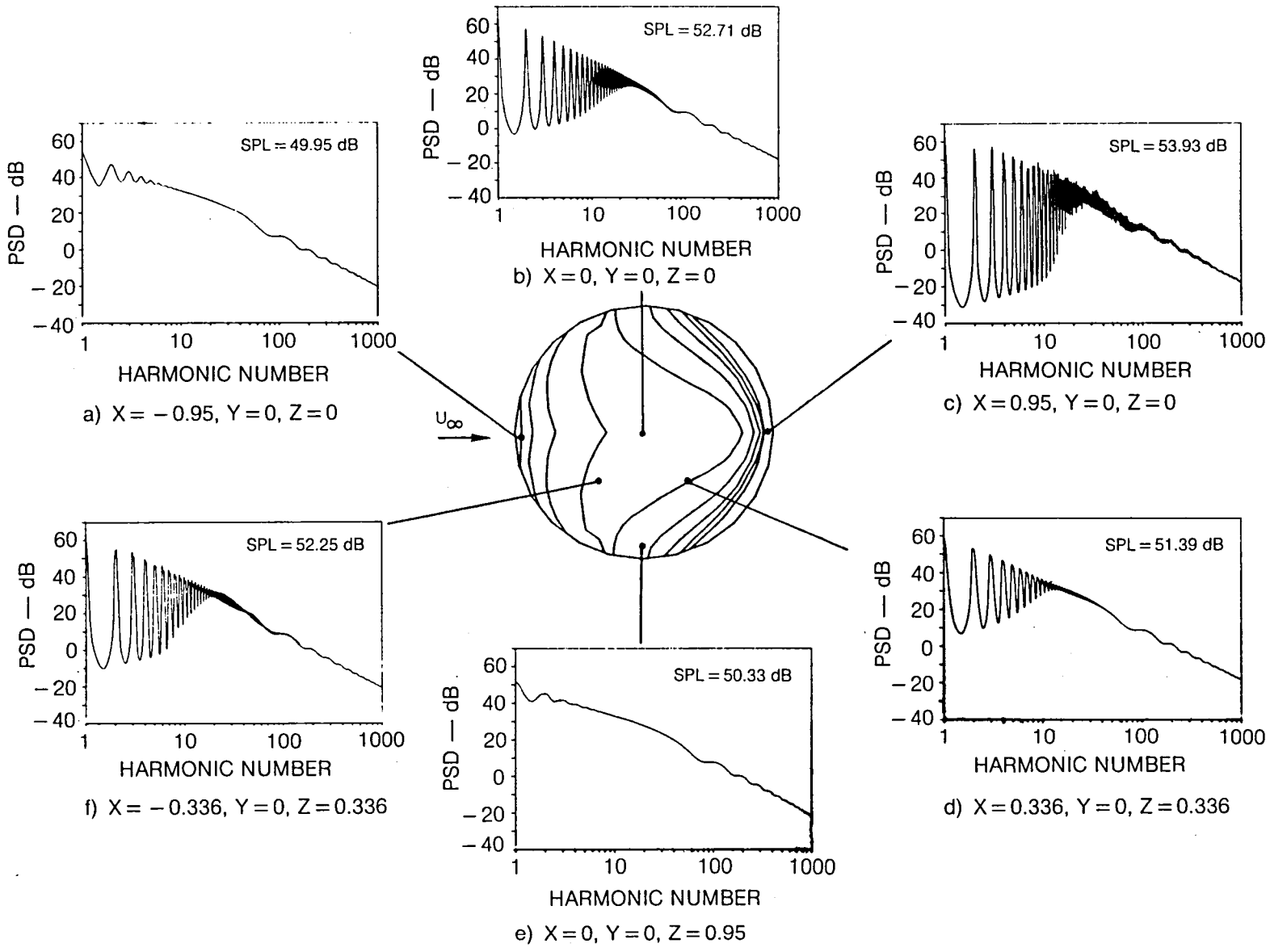

Figure 34 — Spectrum Dependence on Local Vorticity Field, Pseudo Hover Operating Condition, L = ∞, G = 5.1 m/s, Z = 122 m

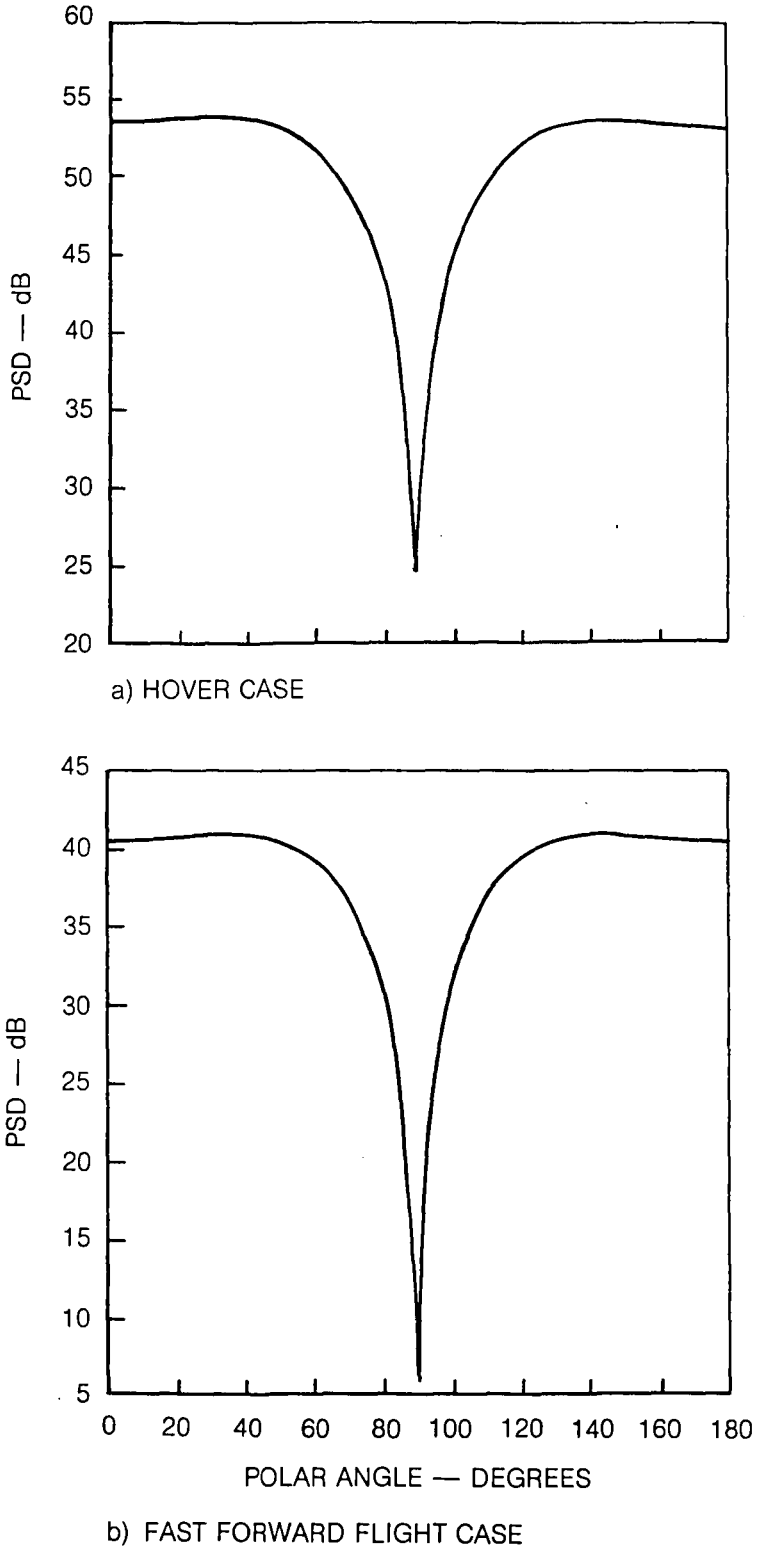

Figure 35 — Polar Directivity, 3rd Harmonic, $\phi = 0$, L = ∞, G = 5.1 m/s, Z = 122 m

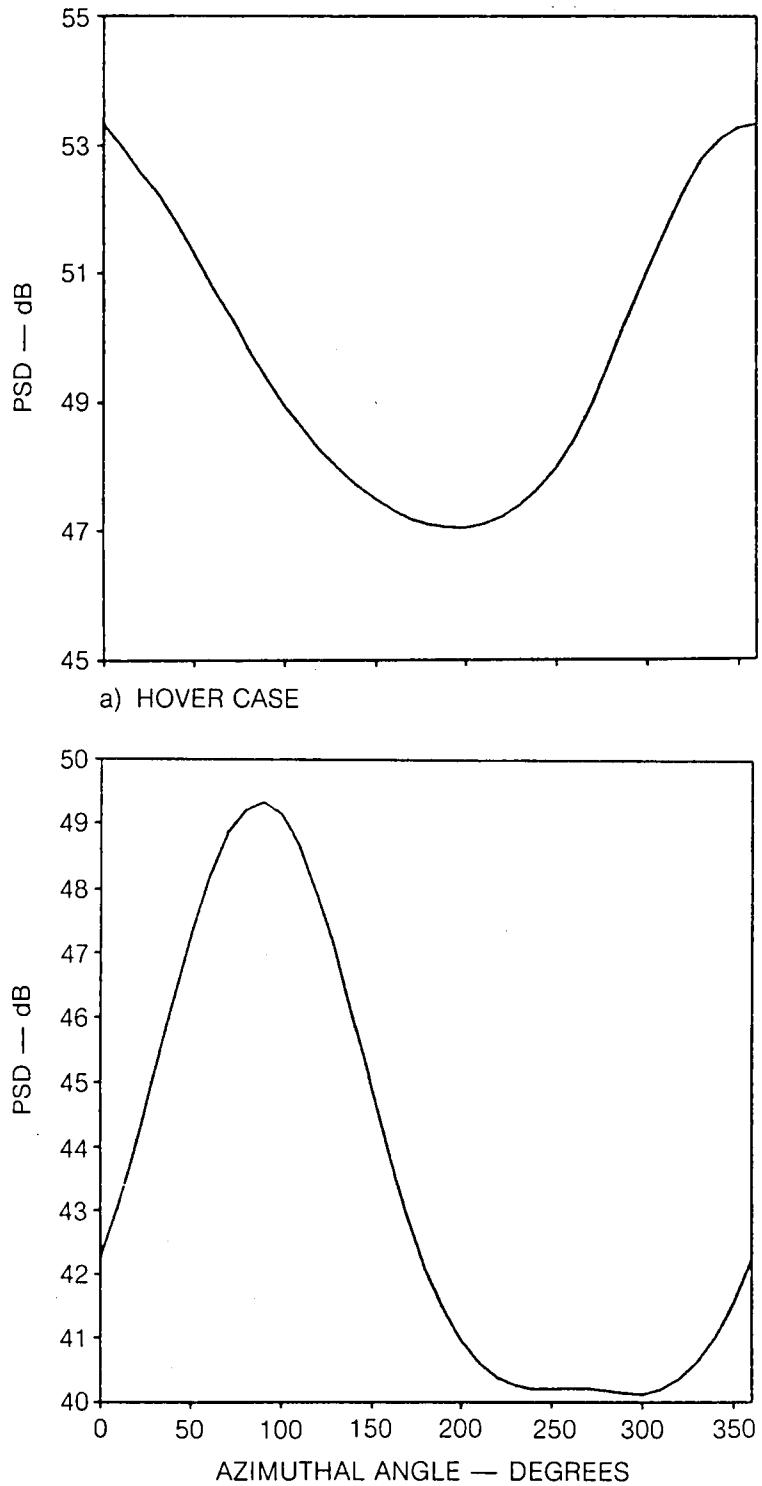

Figure 36 — Azimuthal Directivity, 3rd Harmonic, $\Theta = 45°$, $L = \infty$, $G = 5.1$ m/s, $Z = 122$ m

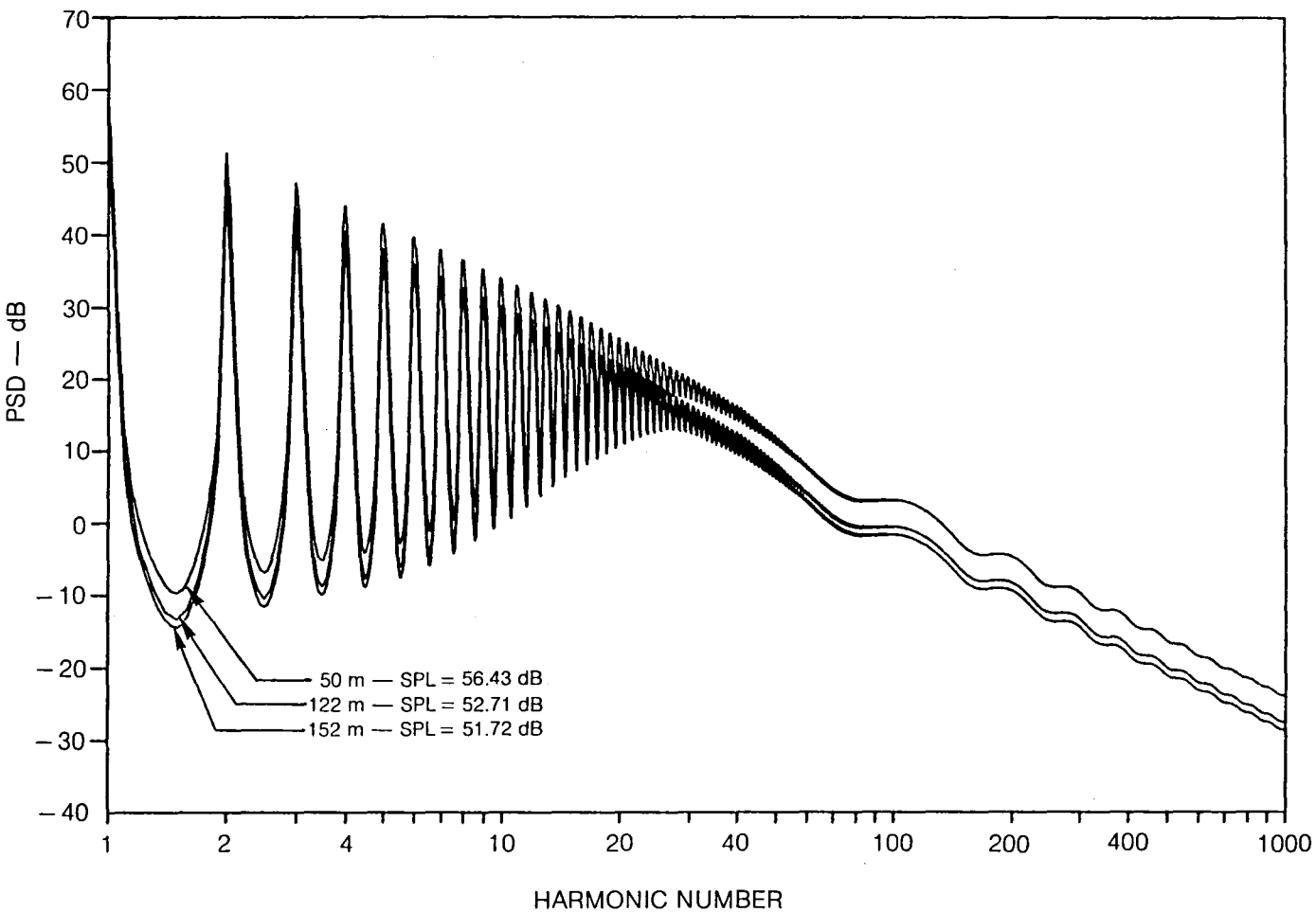

Figure 37 — Spectrum Dependence on Altitude, L = ∞, G = 5.1 m/s

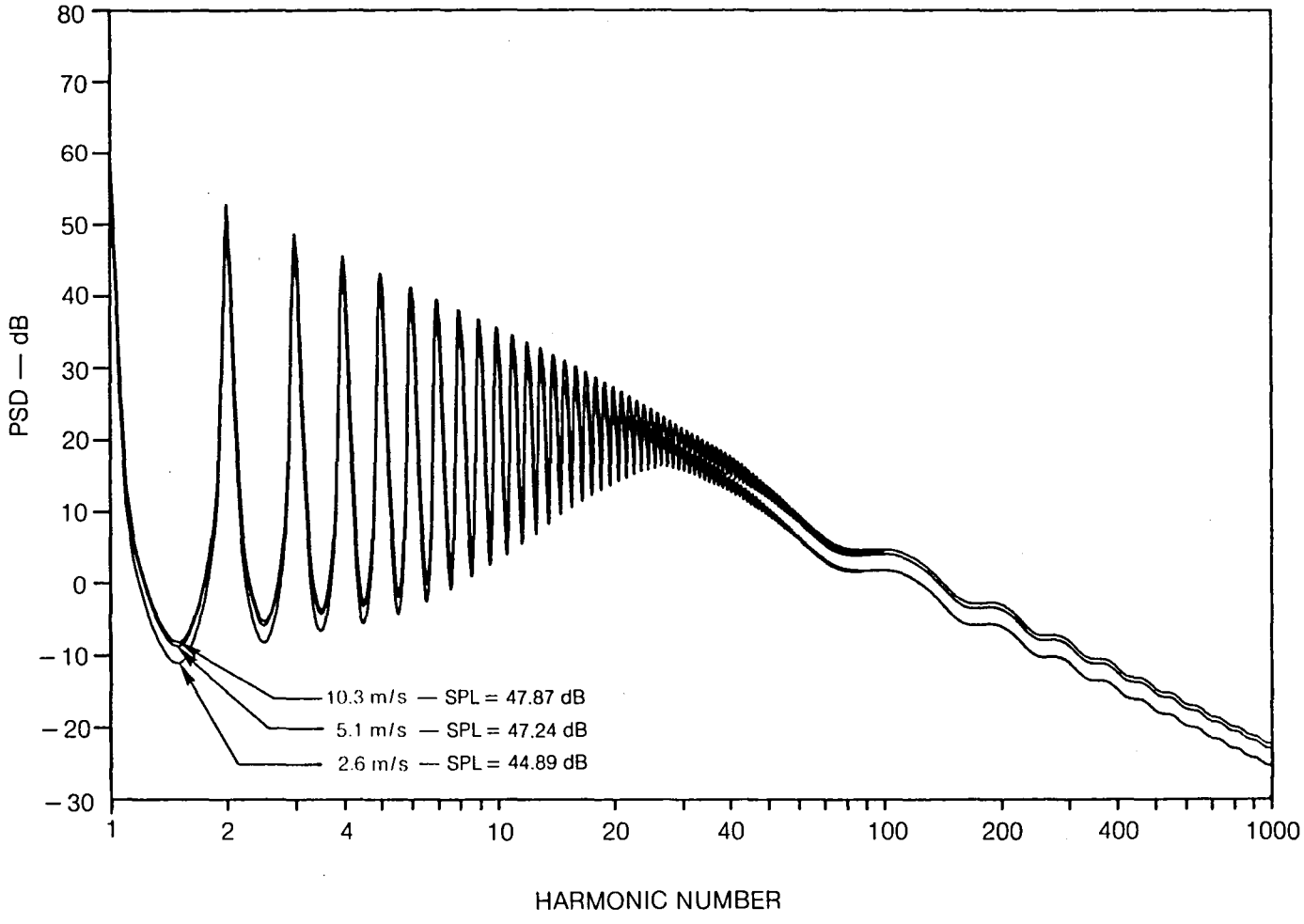

Figure 38 — Spectrum Dependence on Wind Speed, L = 20m, Z = 122 m

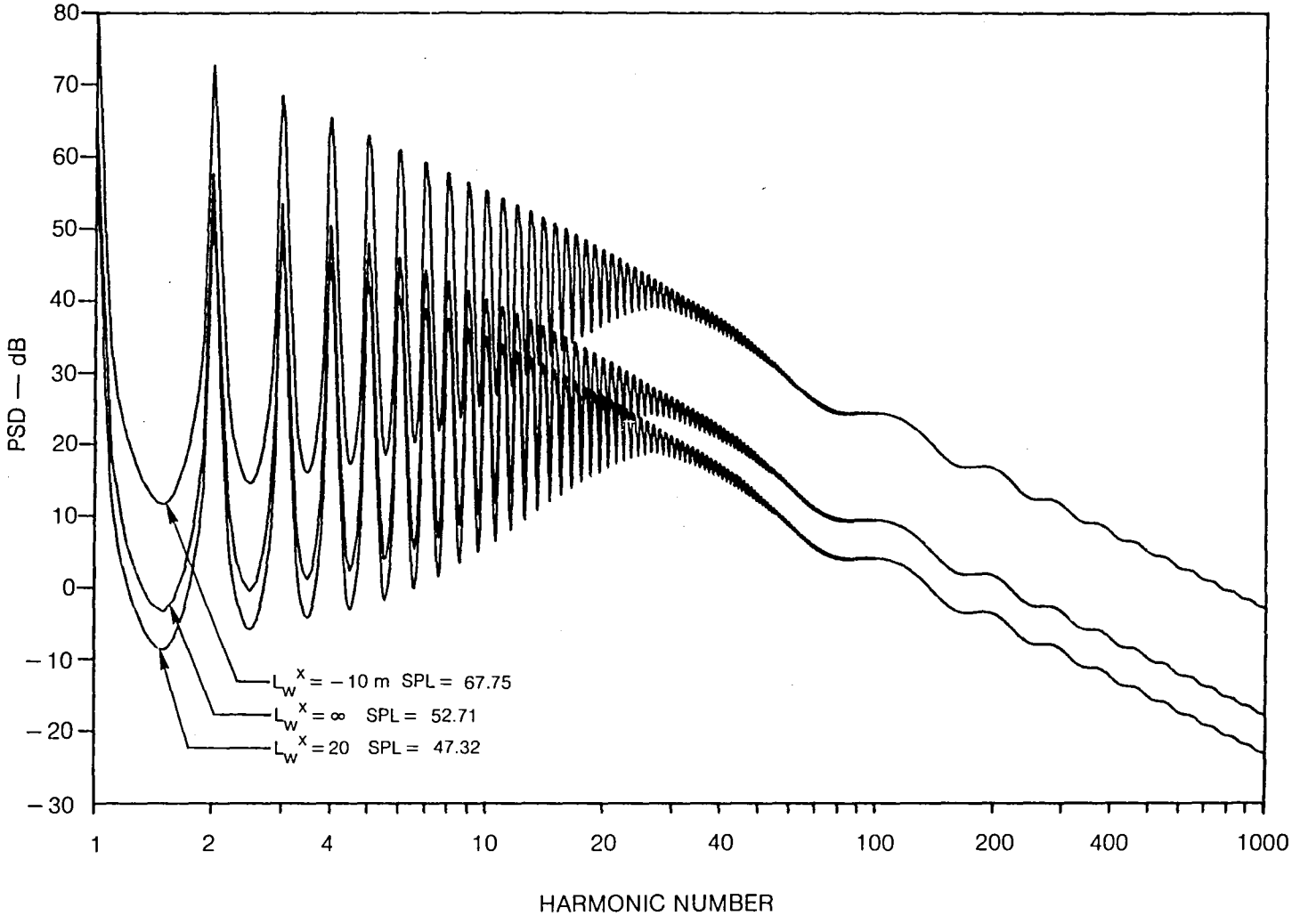

Figure 39 — Spectrum Dependencies on Stability Length, G = 5.1 m/s, Z = 122 m

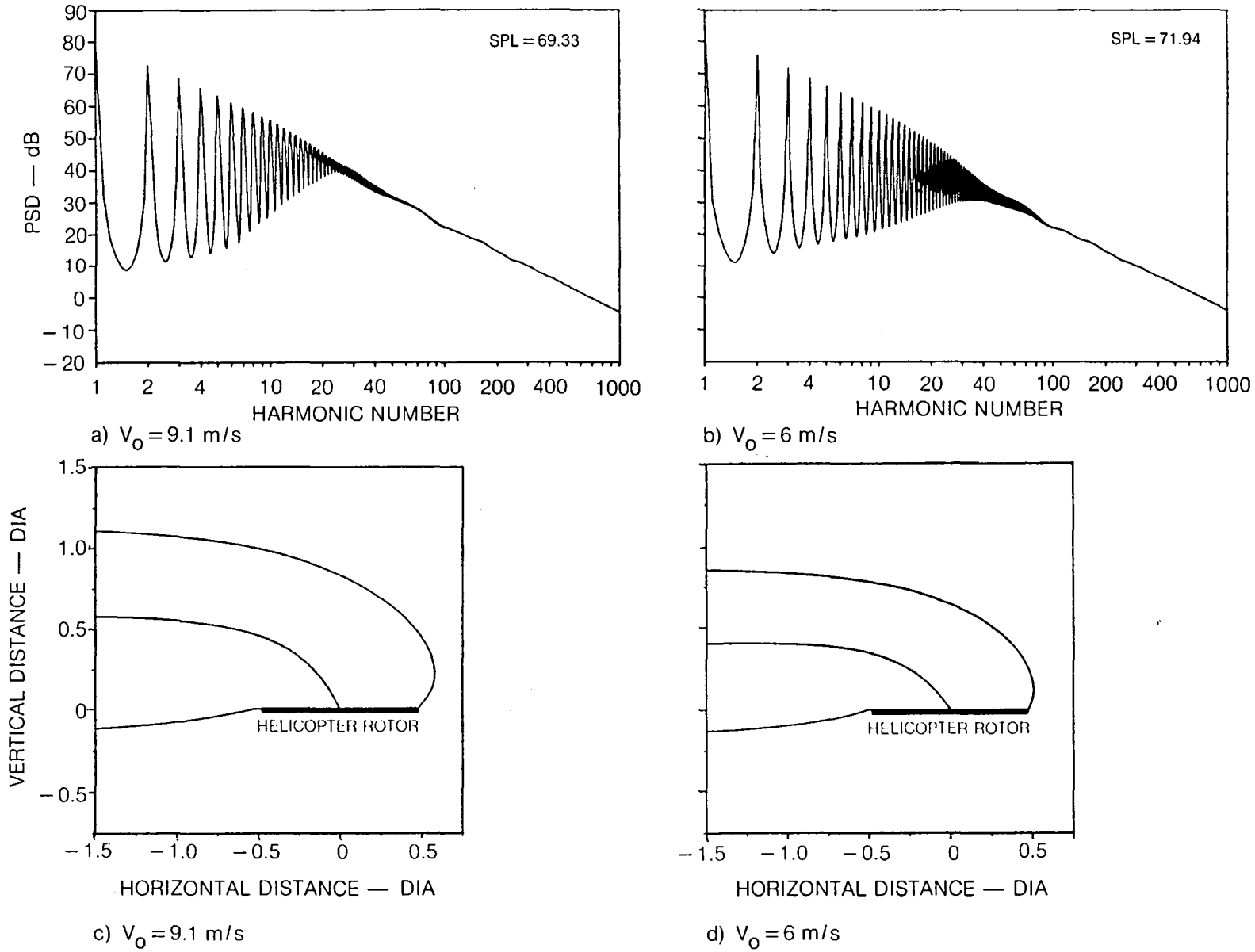

Figure 40 — Spectra and Streamlines for Full Scale Hughes 500 E, G = 2.6 m/s, L = ∞, Z = 8.5 m

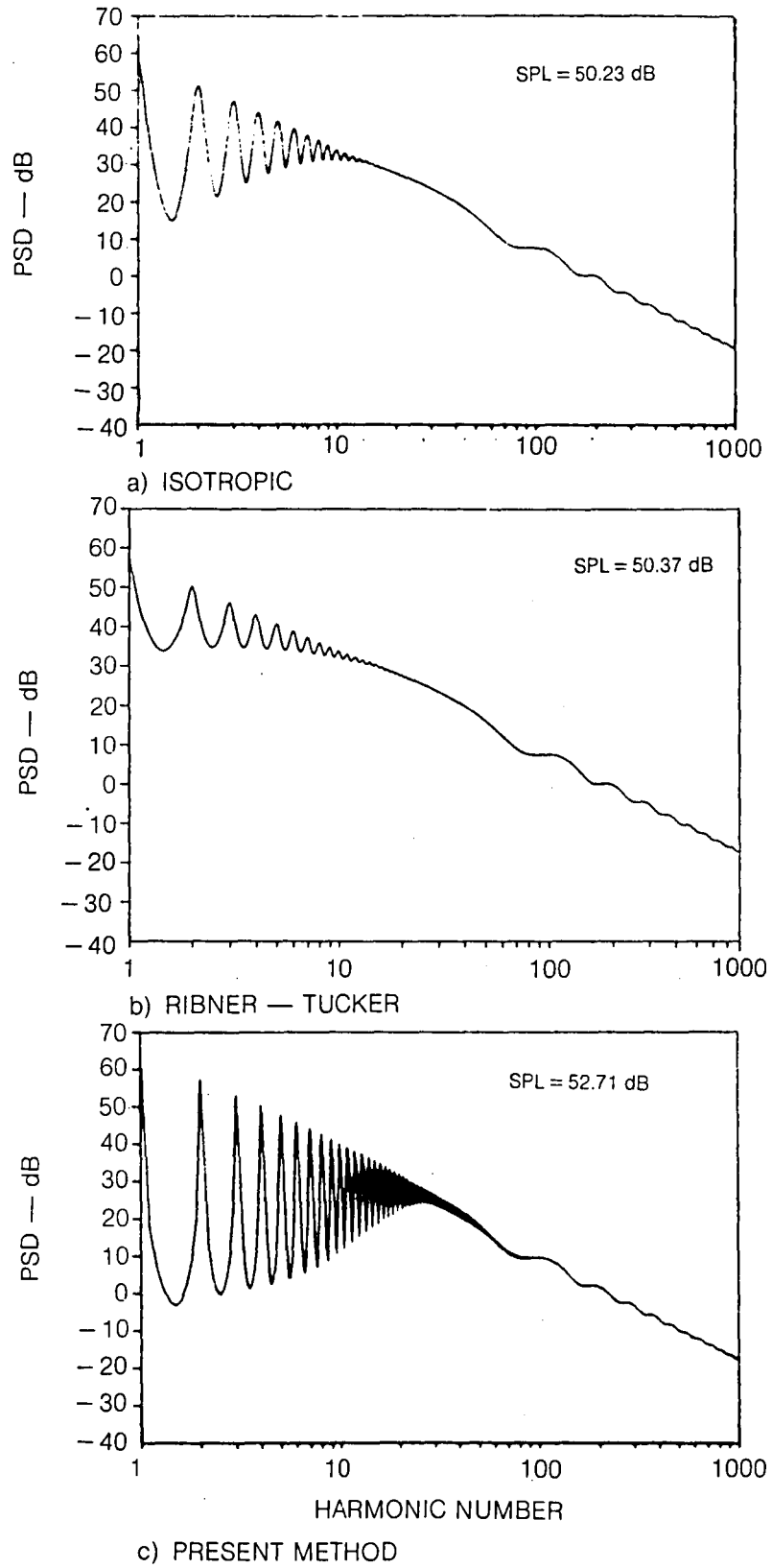

Figure 41 — Spectral Dependence of Turbulence Assumption, Pseudo Hover Operating Condition, L = ∞, G = 5.1 m/s, Z = 122 m

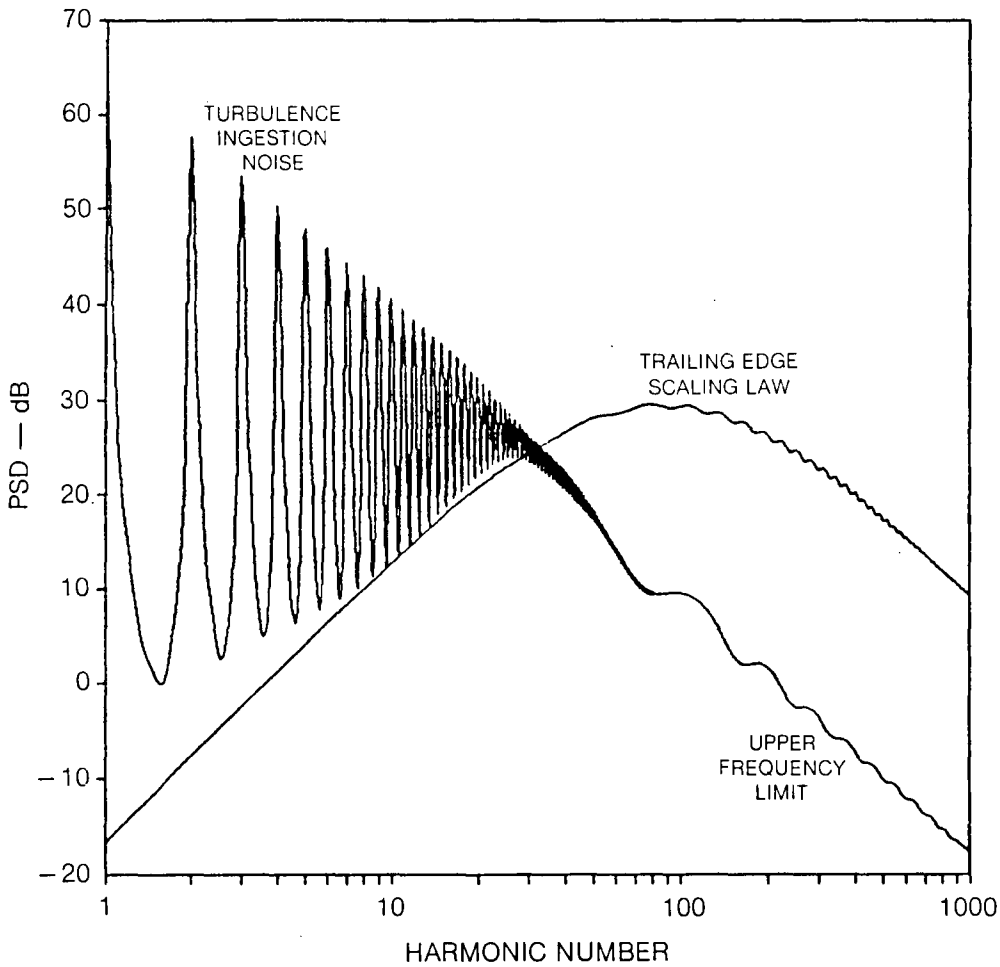

Figure 42 — Turbulence Ingestion Noise and Trailing Edge Noise Comparison, Hover Operating Condition, L = ∞, G = 5.1 m/s, Z = 122 m

1. Report No. NASA CR-3973	2. Government Accession No.	3. Recipient's Catalog No.
4. Title and Subtitle Helicopter Rotor Noise Due to Ingestion of Atmospheric Turbulence		5. Report Date May 1986 6. Performing Organization Code
7. Author(s) John C. Simonich, Roy K. Amiet, Robert H. Schlinker, and Edward M. Greitzer		8. Performing Organization Report No. 10. Work Unit No.
9. Performing Organization Name and Address United Technologies Research Center East Hartford, CT 06108		11. Contract or Grant No. NAS1-17096 13. Type of Report and Period Covered Contractor Report
12. Sponsoring Agency Name and Address National Aeronautics and Space Administration Washington, DC 20546		14. Sponsoring Agency Code

15. Supplementary Notes

John C. Simonich, Roy K. Amiet, and Robert H. Schlinker: United Technologies Research Center, East Hartford, Connecticut.
Edward M. Greitzer: Massachusetts Institute of Technology, Cambridge, Massachusetts.

Langley Technical Monitor: Thomas F. Brooks
Final Report

16. Abstract

A theoretical study was conducted to develop an analytical prediction method for helicopter main rotor noise due to the ingestion of atmospheric turbulence. This study incorporates an atmospheric turbulence model, a rotor mean flow contraction model and a rapid distortion turbulence model which together determine the statistics of the non-isotropic turbulence at the rotor plane. Inputs to the combined mean inflow and turbulence models are controlled by atmospheric wind characteristics and helicpoter operating conditions.

A generalized acoustic source model was used to predict the far field noise generated by the non-isotropic flow incident on the rotor. Absolute levels for acoustic spectra and directivity patterns were calculated for full scale helicopters, without the use of empirical or adjustable constants.

Comparisons between isotropic and non-isotropic turbulence at the rotor face demonstrated pronounced differences in acoustic spectra. Turning and contraction of the flow for hover and low speed vertical ascent cases result in a 3 dB increase in the acoustic spectrum energy and a 10 dB increase in tone levels. Compared to trailing edge noise, turbulence ingestion noise is the dominant noise mechanism below approximately 30 rotor harmonics, while above 100 harmonics, trailing edge noise levels exceed turbulence ingestion noise by 25 dB.

17. Key Words (Suggested by Author(s))	18. Distribution Statement		
Helicopter Noise Rotor Noise Turbulence Ingestion Noise	Unclassified - Unlimited Subject Category 71		
19. Security Classif. (of this report) Unclassified	20. Security Classif. (of this page) Unclassified	21. No. of Pages 150	22. Price A07

NASA-Langley, 1986

End of Document